Master's thesis

NTNU
Norwegian University of Science and Technology
Faculty of Information Technology and Electrical Engineering
Department of Mathematical Sciences

Alastair Patrick Thomas

Spatial Inference of Coseismic Slip on the Cascadia Subduction Zone

Master's thesis in Mathematics
Supervisor: John Paige
June 2024

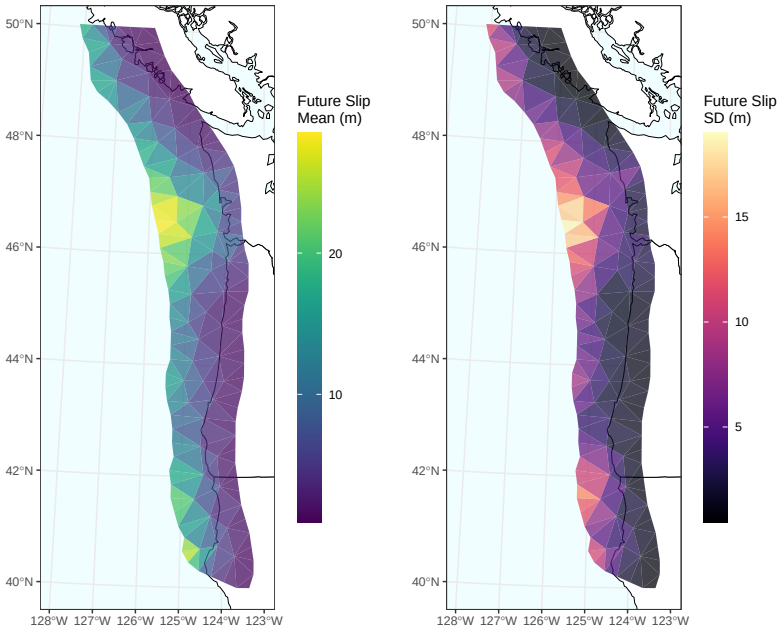

NTNU
Norwegian University of Science and Technology

Alastair Patrick Thomas

Spatial Inference of Coseismic Slip on the Cascadia Subduction Zone

Master's thesis in Mathematics
Supervisor: John Paige
June 2024

Norwegian University of Science and Technology
Faculty of Information Technology and Electrical Engineering
Department of Mathematical Sciences

NTNU
Norwegian University of
Science and Technology

ABSTRACT

Inference about historical great earthquakes is a key step in understanding the risk involved from a potential future event. In the Cascadia region, located on the Pacific Coast of the North American continent, the most recent full margin rupture was in 1700AD. As such the spatial distribution of the movement in the underlying rock structure of the Cascadia Subduction Zone (CSZ) needs to be inferred from geological estimates of surface movements taken throughout this region. This spatial distribution is the CSZ coseismic slip distribution, and the geological estimates used will be a coseismic subsidence data set.

Here we model the underlying coseismic slip distribution as a transformed Gaussian Random Field (GRF), using the Stochastic Partial Differential Equations (SPDE) approach. The main contribution of this work is in developing a Bayesian framework which links the coseismic slip distribution to the geological subsidence estimates via the Okada dislocation model. Existing scientific information is also incorporated into the framework via a taper function and an anisotropic coseismic slip distribution to align with the current literature.

The method is validated by predicting unseen subsidence estimates which demonstrates that the best model presented can capture the geological history of the CSZ well. The data suggests a high degree of similarity between the studied historic great earthquakes, and predicts a potential future magnitude $M_w 9.0$ event which has a high coseismic slip concentrated in the shallower depths of the CSZ. We conclude by reflecting on improvements to be made to the new methodology presented here. The main focus being on incorporating higher quality data sources, as well as increasing the resolution of artificial modelling structures to better capture the continuous nature of the coseismic slip distribution.

SAMMENDRAG

Statistisk inferens rundt store historiske jordskjelv er et viktig steg for å forstå risikoen ved fremtidige potensielle jordskjelv. I Cascadiaregionen, ved Stillehavskysten av Nord-Amerika, ble den siste fullstendige forkastningen dannet år 1700. For å lage en statistisk fordeling av forflytningen av det underliggende berget ved subduksjonssonen i Cascadiaregionen må en bruke geologiske estimater av overflatebevegelsen langs Stillehavskysten ved USA og Kanada i denne regionen. Fordelingen som brukes er en Cascadia subduksjonssone (CSZ) seismisk glidefordeling (coseismic slip distribution) og de geologiske estimatene som brukes vil være datasett med seismiske senkningsinformasjon.

I denne oppgaven modelleres den underliggende seismiske glidefordelingen (coseismic slip distribution) som et transformert tilfeldig Gaussian felt (GRF), ved å bruke en tilnærming med stokastiske partielle differensiallikninger (SPDE). Hovedbidraget fra dette arbeidet er ved å utvikle et Bayesiansk rammeverk som kobler sammen den seismiske glidefordelingen med det geologiske senkningsestimatet via dislokasjonsmodellen Okada.

Metoden er kontrollert ved å beregne senkning i forhold til kjente senkningsestimater. Dette viser at den beste modellen som er presentert kan fange opp den geologiske historien av subduksjonssonen (CSZ) bra. Dataene antyder en stor likhetsgrad mellom de ulike undersøkte historiske jordskjelvene og forutser et potensielt fremtidig jordskjelv til å ha en stor seismisk glidning konsentrert i grunnere deler av dagens subduksjonssone (CSZ). Vi konkluderer med å reflektere over forbedringer som kan gjøres ved den nye metoden som er presentert her. Hovedfokuset vil være på å inkorporere datakilder med høyere kvalitet, samtidig som en øker oppløsningen til de kunstige modellstrukturene for å bedre kunne fange opp den kontinuerlige oppførselen i den seismiske glidefordelingen.

PREFACE

This thesis has been undertaken as the final part of my Master's Degree in Statistics at NTNU. I have a Bachelor's degree in Mathematics from the University of Edinburgh where I wrote a Bachelor thesis titled the "Mathematics of Climate" jointly with two other students. As such it felt only natural that I should research a geoscience based problem for my Master's thesis.

Alastair Patrick Thomas.
03.06.2024

ACKNOWLEDGEMENTS

I would firstly like to thank my supervisor John Paige, for giving me the opportunity to write about such an interesting topic, and providing me with endless support throughout this process. I would also like to thank my fellow students, with a special mention going to the university's orienteering club which has provided me with a fantastic social environment, as well as endless support during my two years of study in Trondheim. And finally my family, who despite being in another country have managed to remain engaged and supportive during this time.

CONTENTS

LIST OF FIGURES

LIST OF TABLES

ABBREVIATIONS

The following is an alphabetical list of abbreviations used throughout this thesis:

- **AE** Absolute Error
- **CRPS** Continuous Rank Probability Score
- **CSZ** Cascadia Subduction Zone
- **GADM** Global Administrative Areas
- **GMRF** Gaussian Markov Random Field
- **GRF** Gaussian Random Field
- **IS** Interval Score
- **MAE** Mean Absolute Error
- **MSE** Mean Squared Error
- **PC** Penalised Complexity
- **PI** Prediction Interval
- **PTHA** Probabilistic Tsunami Hazard Analysis
- **RF** Random Field
- **SD** Standard Deviation
- **SE** Squared Error
- **TMB** Template Model Builder

CHAPTER

ONE

INTRODUCTION

Great earthquakes have the capacity to affect vast areas of the earth. From changing the geological makeup of whole regions through ground failure and surface displacements, to the immediate damage to infrastructure and loss of life caused by violent earth movements, surface faulting and deadly tsunamis [1] and finally the long term socioeconomic impacts of enduring such an event [2, 3, 4, 5, 6]. These great earthquakes, also known as megathrust events, occur in the worlds subduction zones whereby one tectonic plate is being forced under another. A recent example of such an event in which a tsunami was also triggered is the magnitude M_w9.0 Japan 2011 event which is estimated to have damaged $685,000$ residential buildings, caused US$211 billion [7] in total damage and most notably triggered the meltdown of a nuclear reactor [8]. Additionally the M_w9.3 2004 South East Asia event, which also triggered a tsunami, transcended national boundaries causing $226,408$ deaths across the whole of the region [9].

Unlike these examples the focus region of this thesis, the Cascadia Subduction Zone (CSZ) located on the West Coast of North America, has not experienced a megathrust event within living memory. However, there is a plethora of geological evidence to suggest that this subduction zone has a long history of megathrust events [10, 11, 12, 13, 14, 15, 16]. In the last $10,000$ years there have been an estimated 19 megathrust events with the last event hitting the CSZ in the year 1700AD. This was before official written records were kept in the Cascadia region and as such researchers have had to turn to tsunami records in Japan, a stunning 7000 kilometers from the CSZ, and geological records in the Cascadia region to accurately date this event [17]. Of the available geological markers, buried soils at coastal locations along the CSZ will be of highest interest in this thesis. They allow for both the estimation of vertical ground displacement caused by the movement of the underlying tectonic plate during a coseismic event, and the dating of the events through the organic composition of the soils [18, 19, 20]. The term coseismic here is used to describe any geological event that is related to an earthquake. Vertical displacement in the downwards direction is called subsidence, a term used throughout this thesis, and in the upwards direction it is called uplift.

It is no wonder then, that with "the most spatially and temporally complete geological records of past megathrust events" [21] that there has been extensive

modelling efforts with regards to the coseismic activity of the CSZ. The modelling that is particularly of interest here is that which aims to describe the coseismic slip distribution across the CSZ. Coseismic slip is the displacement of the underlying rock, which will henceforth be referred to as the fault, during a coseismic event. The extent of the CSZ fault can be seen in Figure 1.0.1 which shows that it runs over 1100 km from the northern edge on Vancouver Island to the southern point in Northern California. The coseismic slip distribution is not homogeneous across the fault, instead it is more accurately represented as a varying continuous distribution across the entire fault. Inference about this distribution is critical as it directly affects the risk associated with locations throughout the fault region. Higher slip will result in more aggressive ground shaking and trigger more powerful tsunamis which could have dramatic implications for any populated areas in the vicinity of an area with a high slip concentration. Moreover the coseismic slip distribution can be used as the input to tsunami models [22, 23, 24]. Thus increasing understanding about the coseismic slip distribution will enable a better understanding of the risk to the fault region.

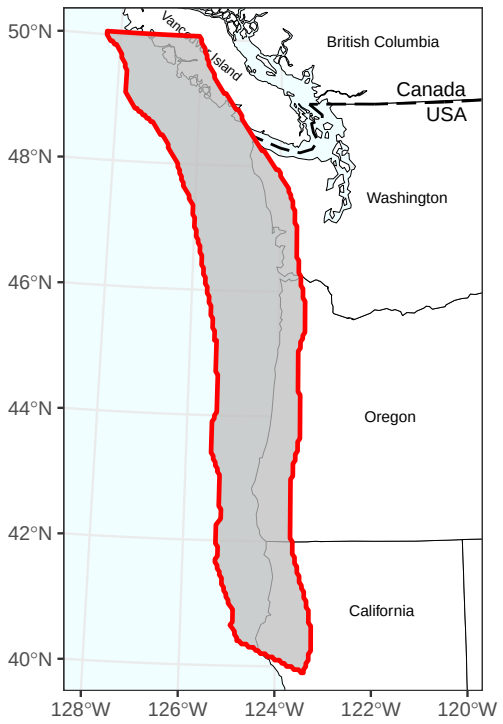

Figure 1.0.1: The area in grey, bounded by red, is the CSZ fault region which will be considered throughout this study. It was created by bounding the point depths of the Slab2 data set [25] which are less than 30 km deep.

Many stochastic point source models have been developed to describe the underlying coseismic slip distribution [26, 27, 28, 29, 23]. In the most recent study here Goda [23], generates 5000 coseismic slip distributions for earthquakes with $M_w \in \{8.1, 8.2, 8.3, ..., 9.1\}$ over the CSZ. These draws are used further, alongside

the fault geometry and a kinematic rupture[1], in a tsunami simulation model. To generate their slip distributions they first simulate from an anisotropic 2D von Kármán[2] wavenumber spectrum which has been calibrated with, amongst other parameters, along-strike correlation and along-dip correlation numbers. Anisotropy means that the spatial correlation between points in the coseismic slip distribution will not be the same in all directions. This is widely agreed upon as being the case for coseismic slip, since observations show that the correlation lengths in the strike direction and the dip direction are different [30]. The strike direction is defined as the angle between the fault boundary and the north line. The dip direction is defined as the angle at which the fault dips down into the earth, measured perpendicular to the strike direction from the horizontal plane. A Box-Cox power transformation[3] is then applied to achieve a desirable right-skewed feature. Then two step taper functions are applied with respect to both depth and on the northern and southern boundaries of the fault. Finally, a constraint is added that requires a suitable slip concentration in the shallower depths of the CSZ. This final constraint was informed by the geological data available and any draw that does not meet the constraint is disregarded. The anisotropy used in this modelling is useful as it reflects the geological reality of a megathrust event. Additionally, use of a taper function here reflects the reality of slips tapering to zero on the down-dip limit of the fault and is widely used in coseismic slip studies [22, 31, 32]. However, their application of a step function here results in an almost discontinuous mean slip distribution which is perhaps not the most accurate reflection of reality.

Melgar et al. [33] have also developed a stochastic point source modelling approach to simulating the slip distribution in CSZ megathrust events, however this time using a K-L expansion[4]. They first assume an earthquake magnitude, with 100 simulations of each $M_w \in \{8.0, 8.1, 8.2, ..., 9.2\}$ used. The fault region is divided into small triangular subfaults. Then a subfault is selected at random and a rectangular area with length and width is taken around the selected subfault whereby said length and width are drawn from a log-normal distribution scaled for the particular magnitude required. The slip distribution on all the subfaults in the rectangular region (which can now be thought of as a vector of known length) is assumed to be multivariate log-normally distributed with a mean vector and covariance matrix. The "log" part here is to ensure that the slips remains positive. The covariance matrix is again based on the von Kármán correlation function. Finally the slip vector has been decomposed using the K-L expansion (see equation (8) from the original paper for the full equation) which allows for a numerically efficient simulation of slip vectors. However, the application of a KL expansion to the slip vector seems complicated and unnecessary, especially since

[1]The kinematic rupture of an earthquake encapsulates the details about how an earthquake propagates throughout time.

[2]The von Kármán function is a mathematical model that can be used to describe the spatial variability and roughness across a field.

[3]The Box-Cox power transformation is used to stabilise the variance of a distribution to more closely approximate a normal.

[4]The Karhunen-Loève expansion is an eigendecomposition for random processes, often used as a low rank representation allowing for each simulations. It states that a random vector can be decomposed into the sum of its mean and the product of eigenvalues, eigenvectors and a standard normal variable.

the expansion is not being truncated which would be the main justification for using such a method. Instead one could just work directly with the multivariate Gaussian distribution through its mean and covariance structure.

Dislocation models have also been applied to help describe the coseismic movements of the CSZ. The 2013 paper of Wang et al. investigates heterogeneous slip distributions that vary in the strike and dip direction [34, 35]. In this paper the Okada model [36] was used to relate the coseismic slip distributions to the subsidence estimates. To create their slip distributions they use a trial and error method, aiming to distribute slip across the region in such a way that produces subsidence predictions which align with the subsidence data. The use of the Okada model here to verify that coseismic slip distributions give predictions of subsidence that match the known geological estimates provides a very interesting link between the underlying distribution and the data. This would lend itself to a Bayesian analysis, as all the components to update prior beliefs about the slip distribution with the observed data are now given. Additionally anisotropy has once again been added into the modelling to distinguish between strike and dip directions.

Logic tree methods of defining the slip distribution have also been used as a component in Probabilistic Tsunami Hazard Analysis (PTHA) [37, 38]. Park, Cox, and Barbosa [38], modelled 72 different combinations of earthquake parameters which came in the hierarchical decision tree of: magnitude $\rightarrow$ slip shape $\rightarrow$ peak slip location for full fault ruptures. The resulting slip distribution was assumed to be Gaussian with parameters based on the combination of these three earthquake parameters and conditional probability weights for each branch informed by the geological data. The way in which the slip distribution has been modelled here is coarse and the resulting slip distributions are just scalar multiples of one another for each magnitude. In order to account for the full distribution of possible outcomes, one would need to incorporate a fully probabilistic spatial process into the underlying slip distribution.

The goal of this work here is thus to do inference about the CSZ coseismic slip distributions for past megathrust events and to then predict the CSZ coseismic slip distribution of a potential future full fault rupture. This should be done in a statistically rigorous way, by using the available data whilst also incorporating valuable scientific knowledge to assist in modelling when the data is not informative enough. It has been shown that modelling the underlying spatial effects which lead to the CSZ coseismic slip distribution is oftentimes done in a Gaussian way, which will be followed here in this work. There are two components which are consistent throughout previous studies and aim to incorporate scientific knowledge about the CSZ coseismic slip distribution. That is the addition of a taper function, and anisotropy in the strike and dip directions. It therefore seems very reasonable to include these in the work here as well. In order to model the CSZ coseismic slip distribution in a statistically rigorous way, the Okada model shall be used as a way in which to inform the slip distributions through the geological estimates along the CSZ coastline. In order to incorporate prior scientific knowledge, which will be very important in properly capturing the

CSZ coseismic slip distribution, Bayesian hierarchical models will be investigated as this gives a framework in which the addition of the prior scientific knowledge into the models can be achieved. To the best of the author's knowledge this is the first time a spatial Bayesian model has been fitted to the geological data in the Cascadia region and is the key contribution of this work. These modelling choices only seem natural since, as demonstrated, there exists data which can be incorporated with pre-existing scientific knowledge about the CSZ which could result in a more detailed and accurate understanding of the CSZ coseismic slip distribution.

This contribution can lead to the better understanding of how a future full margin rupture will affect communities in the Cascadia region, through further risk modelling. These effects can range from the immediate well being of residents of the Cascadia region, to the damage caused to infrastructure to how the region as a whole would be effected from a long term economic standpoint. A perquisite for understanding these effects, which align with the UN's goals for sustainable development [39], is informed knowledge of the CSZ coseismic slip distribution.

1.1 A Note on Readability

A high proportion of the figures used in this thesis will be spatial plots with some value of interest overlayed on top. Therefore a colour scheme will need to be chosen to represent the specific values and scaled such that it is consistent across comparable plots. Importantly here is that any colour scheme used is accessible to as many people as possible, which means taking into account common colourblindness in the general population. This is a well researched topic and many appropriate colour schemes have been made available for general use which are perfectly perceptually-uniform. Here the *Viridis* package [40], the *Scico* [41] and the *CartoColor* [42] package are used. In Figure 1.1.1 one can see all the palettes used in this thesis and what each palette is used for. Most importantly is the the Viridis colour palette which will be used to show central predictions for the CSZ coseismic slip distribution.

1.2 A Note on the Implementation of Analysis

The vast majority of analysis done throughout this thesis has been completed using the R programming language [43], using the R-Studio interface [44]. A link to the code used for analysis is found in Appendix A. When a function from an external library is used for a specific purpose which is highly relevant to the thesis a citation is provided for said external library.

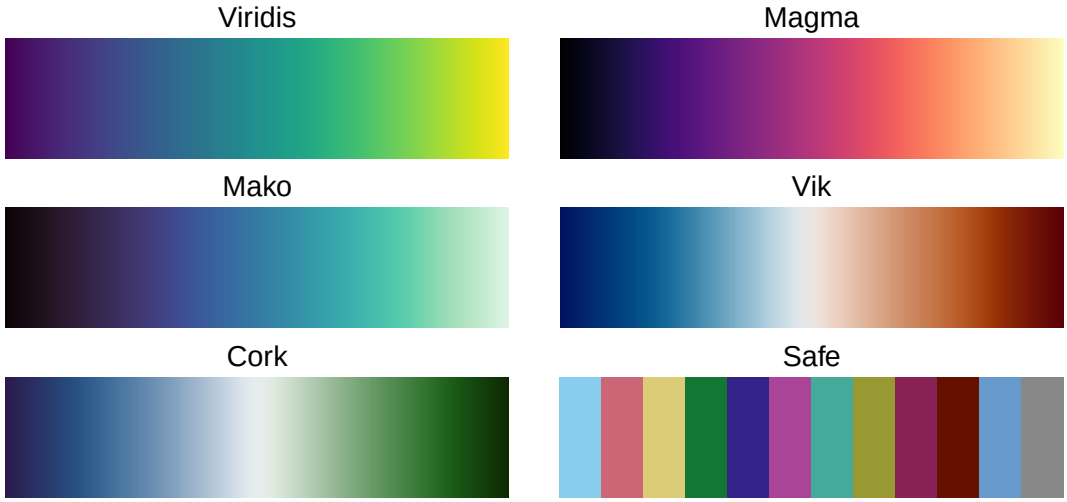

Figure 1.1.1: All the colour palettes used throughout this thesis. The Viridis palette is used to show the central predictions of the CSZ coseismic slip distribution. The Magma palette is used to show any data regarding uncertainty, standard deviations for example. The Mako palette is used to show geometry across space, the depth of the CSZ fault for example. The Vik palette is diverging from 0 and as such is used to show the central prediction for subsidence distributions. The Cork palette is also diverging and is used to show the central predictions for the underlying Gaussian Random Fields. Finally the Safe palette is used for any discrete plots. Viridis, Magma and Mako come from the *Viridis* [40] package. Vik and Cork come from the *Scico* [41] package. The Safe palette comes from the *CartoColor* [42] package.

CHAPTER

TWO

DATA

In this chapter the data sources which are used in the forthcoming modelling of the CSZ are presented, explained and then processed. There are two key data sets that are used. The first is a compilation of surface displacement estimates caused by historical seismic activity, where the estimates are based on comparisons between coastal marsh displacements and a data set of displacement predictions from a dislocation model [18]. The second data set gives the geometry of the CSZ and is the Cascadia subset of Slab2 [25]. Other data sets related to the geological activity of the CSZ do exist, for example turbidite[1] records [15, 16], however for now the work will focus on the aforementioned data sets.

2.1 Country and State Boundaries

As this thesis is concerned with the spatial analysis of the CSZ, it is natural that the majority of the data, methodology and results are best presented in terms of their spatial position, overlaid on top of a base map of the CSZ. To create such a base map, the state and province boundaries of America and Canada were acquired from the Global Administrative Areas (GADM) database [45]. This was then combined with US-Canada border data [46] and all the boundaries were then simplified using a function from the *rmapshaper* R package [47] so that they appear cleaner visually. Finally they were plotted using the *ggplot2* package [48]. This results in a base map which can be seen in the background of Figure 2.2.1 for example. It is worth noting that the place labels and US - Canada border are often dropped from the base map in later plots in order to increase clarity.

2.2 Coseismic Subsidence Estimates

It is well documented that there have been many megathrust events on the CSZ throughout history, [10, 12, 13, 14, 49]. Of these the events, the ones from the past $\sim$ 6500yrs have left visible, and more importantly measurable geological markers along the North American coast which can used to estimate subsidence and its corresponding uncertainty. In this section a data set of such subsidence estimates

[1] Turbidites are the rapid flow of sediments/ rocks down the seafloor, which can be triggered by and therefore indicative of seismic events.

is introduced.

The vast majority of the data set used is taken from the work of Leonard et al. [18] and therefore their notation has been adopted. The features of interest for each data point are the spatial position, given in longitude and latitude coordinates, the amount of subsidence, given in meters, the uncertainty in the subsidence measurement, also given in meters and which megathrust event the estimate belongs to. Each subsidence estimate from this data set has been assigned a megathrust event, labelled as $T1, T2, ..., T12$, which represent the full margin ruptures[2], going chronologically back in time with $T1$ being the 1700AD megathrust event. This data set also includes partial margin ruptures, labelled with an a or b appended to the end. These data points are disregarded as this work focuses only on full margin ruptures. To label each subsidence record with a specific coseismic event, they used published radiocarbon dates of soils to calculate an age distribution using OxCal [50] as well as correlating the subsidence data with turbidite records[15, 16]. For more details on the dating of estimates please see Figure 4 from Leonard et al. [18].

The subsidence estimates are made by looking at the differences in elevation between buried soil layers at collection sites. During a megathrust event marsh land will sink due to coseismic subsidence and will therefore be exposed to more tidal activity. Sediment from the increased tidal activity will then cover the sunken land, creating a buried soil. It is assumed that this process happens fairly quickly, i.e. on the time scale of weeks and thus the effects of gradual uplift are negligible. Then during the time period between megathrust events, gradual uplift brings the buried soils back up to a higher tidal zone where the development of organic-rich soil is facilitated. The different tidal zones, classified by elevation, have a unique collection of organic material. Finally the coseismic subsidence is estimated by the elevation difference between each buried soil layer and the sediment layer directly over it. The error in the measurements comes from the estimation of the paleoelevation[3], which is done by evaluating the organic content as well as macrofossil[4] and microfossil[5] content in each layer. Most of the data comes from measurements based on organic material and macro fossil analysis which usually results in an error of $\pm 0.5 - 0.8$m. However some sites have microfossil samples available which combined with transfer function analysis [51] can reduce the error to $\pm 0.2 - 0.3$m. Leonard et al. [18] therefore categorised the subsidence estimates into three categories:

1. High quality - Estimates based on microfossil analysis;

2. Medium quality - Estimates based on organic content with macrofossil content on both side of the contact;

[2]A full margin rupture is a seismic event which effects the entirety of the tectonic plate boundary.

[3]Paleoelevation is the historical elevation of land.

[4]A macrofossil is what most people would consider to be a normal fossil, visible to the naked eye and above 1 mm in size.

[5]A microfossil is one which needs to be studied with a microscope and is typically anything under 1 mm in size.

3. Low quality - Estimates based mainly on organic content, with macrofossil content on one or no sides of the contact.

The data set is then supplemented with three new, high quality, subsidence estimates from the 2021 study by Padgett et al. [20]. These estimates are located in the Humboldt Bay area of Northern California. In this study they analysed samples from the region and used a Bayesian transfer function methodology to date the soil samples with a lower uncertainty. Their subsidence estimates and uncertainties are taken from Table 4, and the locations are given from Figure 2 in the referenced paper. This Bayesian transfer function methodology has also been previously implemented across the whole CSZ by Kemp et al. [19] but the summary statistics of their results are not publicly available so their estimates have not been used in the analysis here.

The final data set compiled is compromised of 429 subsidence estimates spread over 23 collection sites. Following the classification of Leonard et al. this final data set consists of 13.75% high quality estimates, 8.86% medium quality estimates and 77.39% low quality estimates. Figure 2.2.1 shows that these sites run the length of the Cascadia coastline, starting on Vancouver Island in the north at Port Alberni, running all the way down to Northern California in the south at Eel River. It is also evident from Figure 2.2.1 that the spatial location of the sites vary mainly with latitude and not so much with longitude. This can provide a modelling challenge as the area of interest does in fact extend with longitude. Furthermore the northern and southern extremes of the CSZ could be under-represented in the data set as there are only 2 sites on Vancouver Island and similarly there are only 2 sites in Northern California, which again needs to be considered when modelling with this data set. It is also shown that the number of subsidence estimates made per site varies throughout the data set from only 1 estimate at both Quinault River and Nehalem River up to 79 estimates at Coos Bay, which again adds some spatial skew into the underlying data.

The value of all the subsidence estimates and corresponding uncertainties can be seen from Figure 2.2.2. This shows that the estimates range from approximately $0 - 2.25\,\text{m}$ with the uncertainty ranging from roughly $0.25 - 1.25\,\text{m}$. The highest estimates of subsidence is in the Washington region at Willapa Bay and Columbia River. However these estimates also have some of the largest uncertainty values. In the northern and southern extremes of the CSZ the estimated subsidence's look quite conservative at approximately $0.5 - 1.0\,\text{m}$ with an uncertainty on the lower end of the scale.

Since this work is mainly focused on describing the geological movement of megathrust events it is important to be aware of how the subsidence estimates are distributed amongst the 12 megathrust events. In Figure 2.2.3 the sites which have subsidence estimates recorded for each megathrust can be seen. The title of each sub plot also gives the total number of subsidence estimates that have been collected for each megathrust event. It is clear that the 1700AD megathrust event is the dominant event in this data set, with 45.92% of the data points relating to this event. The 1700AD earthquake also has a good spatial spread of data points, which is not the case for all the events. For example the $T11$ event only has 3 subsidence estimates spread over 3 collection sites. When modelling megathrust event it will be important to evaluate how these varying distributions of subsidence

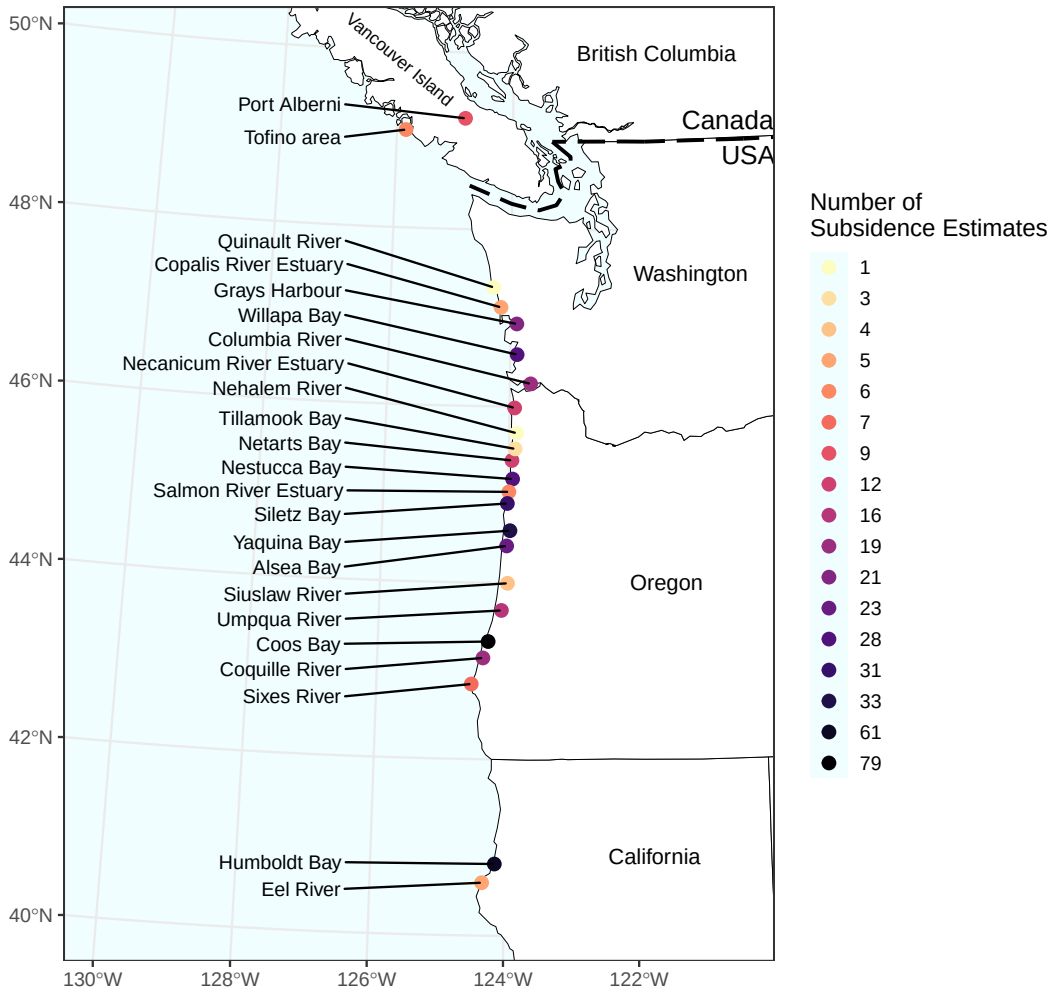

Figure 2.2.1: The locations of the sites where subsidence estimates have been made along the CSZ. Each point is coloured by the number of estimates in the data set made at that site. The labels are placed using *ggrepel* [52].

estimates effect the results.

2.3 Cascadia Subduction Zone Geometry

In order to model the coseismic slip distribution of the CSZ during a megathrust event, it is essential to obtain an accurate geometry of the CSZ. Most important to the modelling presented in this thesis is to obtain the depths across the entirety of the subducting plate. This is because the Okada model [36], relies on a 3D representation of the fault geometry, will be used to predict subsidence values at the surface, thus allowing for inference about the slip distribution from the subsidence data set presented in Section 2.2. An accurate geometry at as high a resolution as possible is therefore critical.

In 2018, Hayes et al. [25] published an updated geometrical model of all the

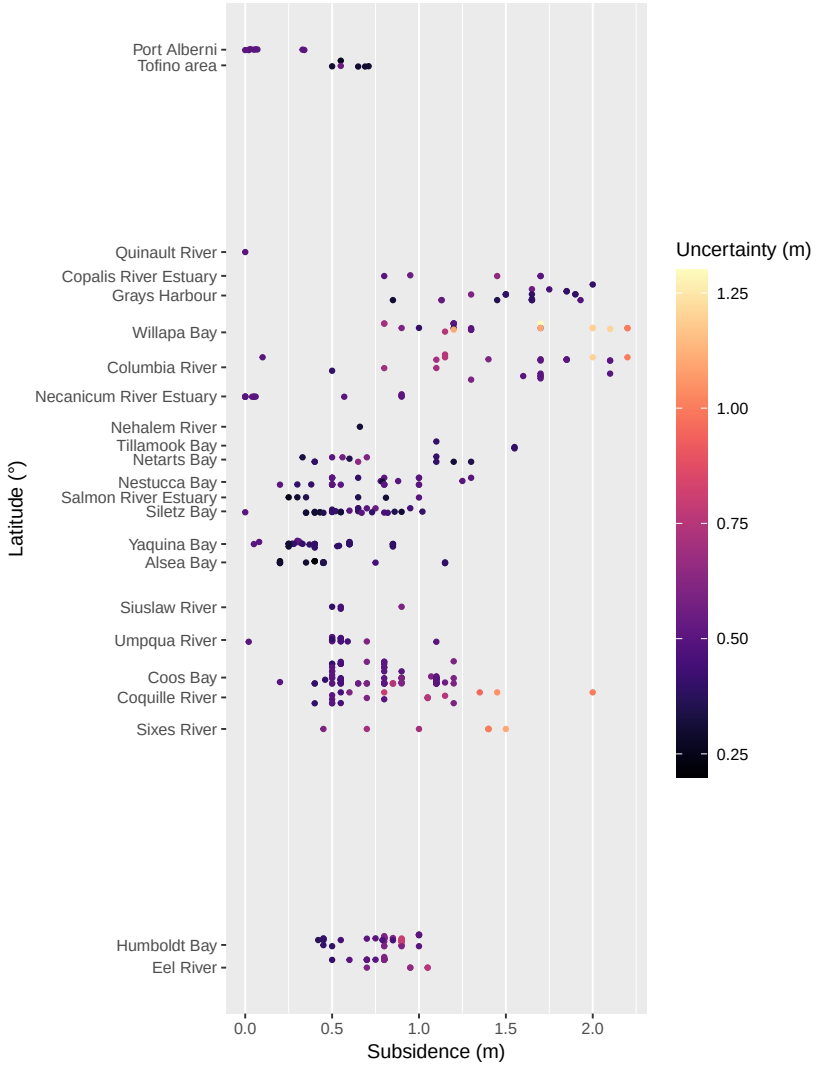

Figure 2.2.2: All the subsidence estimates plotted against the latitude at which they were observed. The names of the site locations are also plotted with latitude and the estimates are coloured by their uncertainty.

subduction zones in the world which has been named "Slab2". This presents the detailed geometry of more than 24 million km^2 of subductive zones, of which the CSZ is included. They have included data from active-source seismic data interpretations, receiver functions, local and regional seismicity catalogues (from both regional networks and relocation studies), and seismic tomography models and as such claim that the Slab2 model gives a better geometry than other available subduction zone geometries, especially at shallower depths. This is particularly important to the modelling done here, as the inference will be on a fault geometry that is limited to the shallower depths of the CSZ.

The specific Slab2 data set used here can be found online [53]. This data set contains different geometries with those of interest being the depth, dip and strike files. The depth given by the Slab2 data for the CSZ can be seen in Figure 2.3.1. This shows that the CSZ is shallowest on the western side and increases in depth as one travels eastwards over the CSZ.

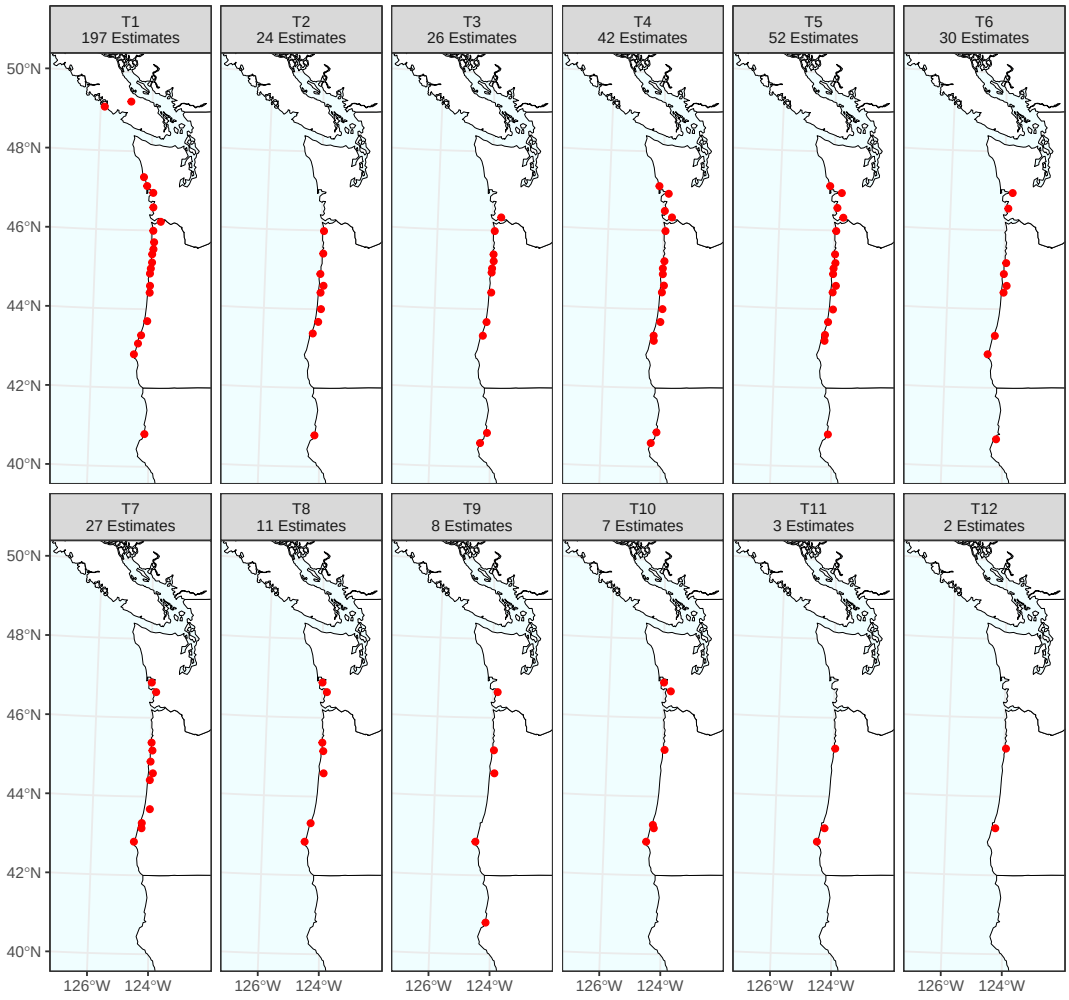

Figure 2.2.3: The locations of the sites for which each megathrust event has subsidence estimates recorded are displayed in red. The total number of subsidence estimates for each megathrust event is given in each facet heading.

This depth data set is then used to create the subfault triangulation seen in Figure 2.3.2. Firstly the Slab2 data is limited to depths of 30 km which is in line with thermal studies of the CSZ [54, 34]. There has also been research into the potential of a deeper coseismic slip distribution, down to depths of 50 km [55], but this is left as a possible extension to the modelling. With the point depth data limited to depths of 30 km a concave hull is created using the *concaveman* package [56]. This hull is then slightly shrunk by 0.1 km using the *buffer* function of the *terra* package [57]. This ensures that all the depths of the triangulation created are non NA. Next the INLA package [58, 59] is used to create a triangulation over the region whereby the function *inla.mesh.2d* is used with the interior boundary hull being the one just described and an exterior hull which is created arbitrarily bigger (in the end only the interior is of interest). There are two key parameters in this function which control the resolution of the subfault triangulation created: max.edge and cutoff. max.edge controls the maximum length of edges within the interior boundary and between the interior and exterior boundary. This parameter

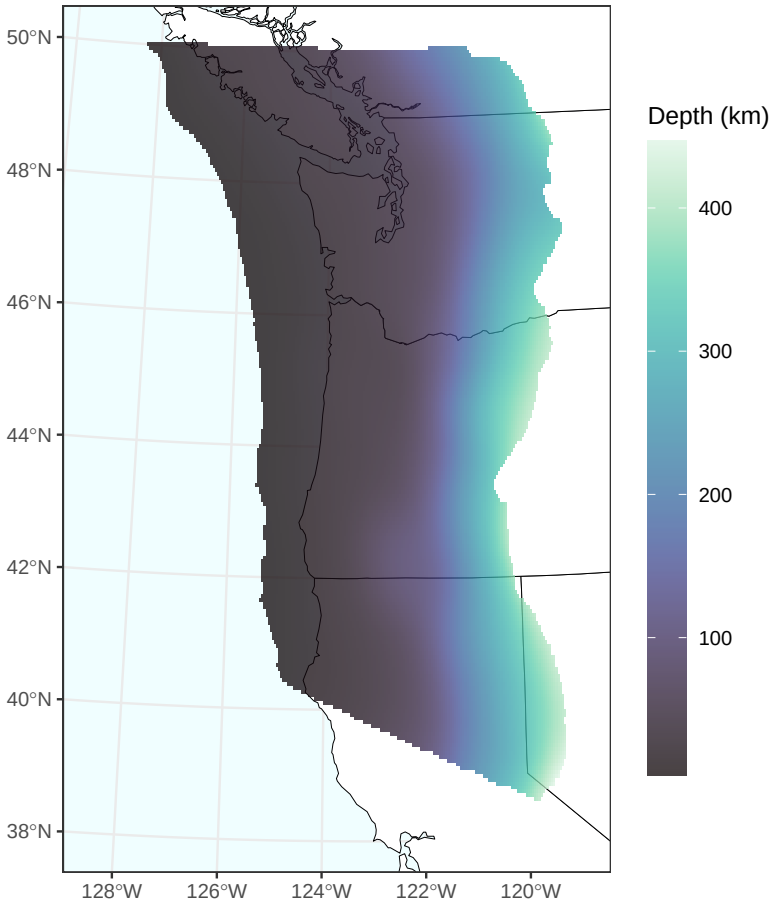

Figure 2.3.1: Illustration of the point depths for the CSZ as given by the Slab2 [25] data set.

is set to $[75\,\text{km}, 1000\,\text{km}]$ such that the largest triangular subfault created within the interior will have a side length of 75 km. Then the cutoff parameter is set to 25 km which means that the smallest possible triangle will have a side length of 25 km. Getting rid of anything outside the interior hull gives the triangulation also seen in Figure 2.3.2. Now the depths at the centroids of each triangular subfault are calculated. This is achieved by interpolating from the Slab2 data, via the *interp* function from the *akima* package [60] and results in the depths seen in Figure 2.3.2. It should be noted that during this whole process the data was transformed to Easting and Northing coordinates so that using distance parameters makes sense. This results in a triangulation of 188 subfaults. This is not as fine as would be optimal to represent the continuous nature of the CSZ coseismic slip distribution, however due to computational bottlenecks, this is as fine as was reasonably possible. It results in a subfault triangulation whereby the average distance between the subfault centroids is 25.6 km.

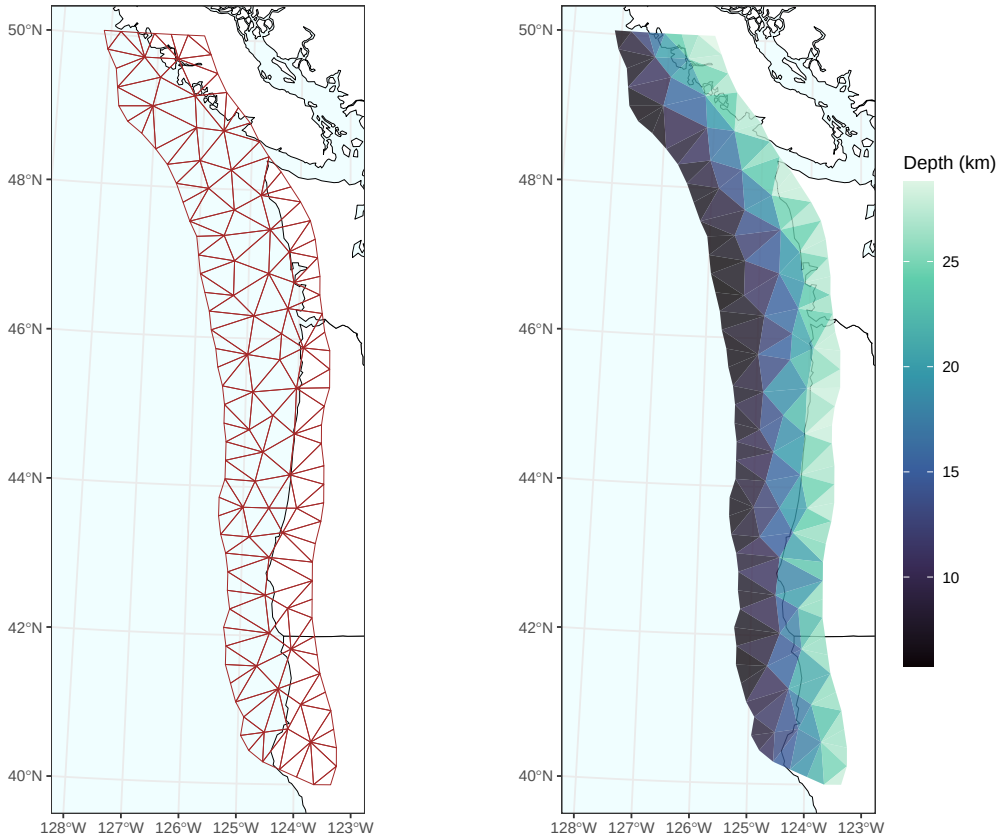

(a) (b)

Figure 2.3.2: In (a) the triangular subfault geometry created using INLA functions and the Slab2 data set is shown. In (b) the same geometry but with each subfault coloured by the depth at its center is shown. This depth was calculated by interpolating the Slab2 point depth dataset.

CHAPTER

THREE

MODELLING

In this chapter four new spatial models used to describe the coseismic behaviour of the CSZ are introduced. Before this however, two pre-existing methods need to be introduced which are then subsequently used as building blocks in the modelling of the CSZ. The first of these is a surface deformation model, the Okada model [36], which is used to map a slip distribution over a subfault geometry to surface displacements. The second of these is the SPDE method [61], which enables computationally efficient modelling of GRFs. Using these, the spatial models of the CSZ can be introduced. Finally, Template Model Builder (TMB) [62], a software package for R, implemented with C++, which allows for the fitting of statistical latent variable models with random effects to data, is introduced.

3.1 Okada Model

A key step in the modelling of the CSZ is to link the coseismic slip distribution to the coseismic subsidence. This step enables the spatial model of the underlying slip distribution to be fitted to the subsidence data set (Section 2.2) and is achieved through the application of the Okada model [36].

This model requires an underlying fault geometry, which is described here as a triangular mesh of subfaults, whereby each subfault is defined by its geometric parameters, most notable the locations of the corners of the subfaults and the depths of the centroids. It is assumed that the entire fault is embedded in an elastic[1], homogeneous[2] and isotropic[3] half-space[4].

A slip distribution is then assumed over the fault, with each individual subfault having a given value of slip representing the average slip over that subfault. The Okada model then uses Green's functions to describe the response of the half-space to the coseismic slip on each subfault. This will give the contribution of each individual subfault to the vertical and horizontal movement at a set of points

[1] An elastic space is one which returns to its original state once external forces are removed.

[2] In a homogeneous space, all the properties of the material are assumed to be uniform throughout.

[3] Isotropic means that the response to any external forces will be the same in any direction.

[4] A half-space is one in which only a certain section of the space is considered for analysis. For example $\mathbb{R}^3$ can be divided into two by the x-y plane. The half whereby z is positive is called a half space.

on the earths surface. Finally, the Okada model is linear, so the total movement at each point on the surface can be calculated by summing up the contributions of each subfault.

For this work the Okada model has been implemented in R by translating and modifying the Python code found in Clawpack [24]. Specifically, what is known as the "Okada matrix", G, is of interest here. This matrix can be thought of as the Okada mapping from the space of average slips on each of the S subfaults to the N surface deformations at the locations of the subsidence data. It is therefore of dimension $G \in \mathbb{R}^{N \times S}$, and is found by assuming a unit slip over the S subfaults. Thus, in general, taking the product of G and a vector of slips, $\boldsymbol{s} \in \mathbb{R}^S$, one can predict a vector of subsidences, $\hat{\boldsymbol{y}} \in \mathbb{R}^N$, which are the result of the given slips:

$$\hat{\boldsymbol{y}} = G\boldsymbol{s}. \tag{3.1}$$

3.2 SPDE Method

Throughout the following spatial modelling an underlying, continuously indexed, stationary, Random Field (RF), $\boldsymbol{X}(\boldsymbol{l})$, will be assumed. Here $\boldsymbol{l} \in \mathbb{R}^2$ is a location within the domain $\mathcal{D}$, whereby $\mathcal{D}$ is taken to be the domain of the subfault triangulation. Furthermore, the RF will be assumed to be a Gaussian Random Field which means that any finite collection of points taken from $\boldsymbol{X}$, say $\boldsymbol{x} \in \mathbb{R}^B$, are jointly Gaussian distributed. In other words $\boldsymbol{x}$ is multivariate normal, with mean $\boldsymbol{\mu}$ and covariance matrix Σ. In order to use the SPDE method and in keeping with standard spatial modelling practises, the covariance structure will be defined via the Matérn [63] covariance function. For a Euclidean distance of h between two points in $\mathcal{D}$, the covariance function is:

$$C_0(h|\sigma, \nu, \kappa) = \sigma^2 \frac{1}{2^{\nu-1}\Gamma(\nu)} (\kappa h)^\nu K_\nu(\kappa h), \tag{3.2}$$

where σ^2 is the marginal variance, ν relates to the smoothness of the field, and κ controls the range of the field. Throughout the following modelling $\nu = 1$ is chosen because the SPDE is solved for this value. In order to maximise the likelihood that the models created capture the movement of the plate tectonics, the fault geometry, created in Section 2.3, is made with as high a resolution as was computationally possible: $S = 188$ triangles, representing subfaults. This means that any direct modelling approach for X would involve a covariance matrix with dimensions of at least 188×188. And it would be dense. This would pose a significant problem when trying to fit the model as many, expensive matrix operations will be needed. This has been a universal problem in spatial statistics, however Lindgren, Rue, and Lindström [61] proposed a rather abstract, yet powerful and most importantly computationally efficient solution in their 2011 paper which will henceforth be referred to as the SPDE method.

Essentially their idea is to approximate the GRF with a Gaussian Markov Random Field (GMRF), which is defined via a sparse precision matrix, and to do the computations using the pre-existing efficient algorithms for sparse matrices. The approximation of X to a GMRF is derived by first recognising that a GRF with

Matérn covariance structure is the solution of the Stochastic Partial Differential Equation (SPDE) given by:

$$(\kappa^2 - \Delta)^{\frac{\alpha}{2}} X(\boldsymbol{s}) = \tau \mathcal{W}(\boldsymbol{s}), \tag{3.3}$$

where Δ is the Laplacian operator, and $\mathcal{W}$ is spatial Gaussian white nose with unit variance. They then show that a certain GMRF (seen in their Equation (6)) is also an approximate solution to (3.3), with different values of ν equating to convolutions of the coefficients in the GMRF precision matrix. Finally and perhaps most usefully, they then derive the precision matrix for the GMRF over an irregular triangulation of the domain $\mathcal{D}$, and explicitly give it in terms of the parameters of the original Matérn GRF. The full details of the derivation can be seen in the original paper [61].

The practical outcome of the SPDE method is that a triangulation of the domain of interest $\mathcal{D}$ is needed, whereby the corners of the triangles are points of interest in the GRF. In the case of modelling the CSZ these points of interest will be the centroids of the triangular subfaults defined as the average latitude and longitude of the corners of the subfaults. This triangulation will henceforth be referred to as the "SPDE mesh" and is calculated using *inla.mesh.2d* in a similar manner as the subfault triangulation. Since the SPDE method is an approximation a projection matrix from the SPDE mesh to the points of interest is required. This projection matrix is named $A \in \mathbb{R}^{S \times B}$ and takes the evaluation of the GMRF on the SPDE mesh to an evaluation of $\boldsymbol{X}$. Thus to create the SPDE mesh the initial locations are given as the centers of the subfaults, the inner and outer lengths are 75 km and 1000 km respectively and the cutoff is set to 15 km. Note 15 km is smaller than when creating the subfault triangulation which ensures that every subfault centroid will have a node in the SPDE mesh. This will improve the accuracy of the SPDE approximation to subfault slips. The resulting SPDE mesh is shown in Figure 3.2.1.

This mesh contains $B = 483$ vertices, which are also referred to as basis functions, 844 triangles and extends beyond the area of interest. This is the boundary zone and is added to mitigate the boundary effects in the area of interest, which is inside the purple boundary and where the triangulation is finest. Figure 3.2.1 also shows a zoomed in section of the domain $\mathcal{D}$ with both the SPDE mesh, the subfaults and the centroids of the subfaults being plotted. This demonstrates how the centers of the subfaults have been used as the vertices in the SPDE mesh.

3.3 Independent Megathrust Events

The first spatial model presented is the most simple, and aims to describe the coseismic history of the CSZ as was introduced in Section 2.2. This model will often be referred to as the "isotropic model without a shared spatial component", or for ease of readability "model 1". In the history of the CSZ section, it was shown that there is $M = 12$ megathrust events which data has been collected for. Let megathrust events be indexed $m \in (1, 2, ..., M)$. Each event has N_m data points describing it, and thus this gives $M = 12$ subsidence data vectors, $\boldsymbol{y}_m \in \mathbb{R}^{N_m}$ and $M = 12$ standard deviation vectors, $\boldsymbol{v}_m \in \mathbb{R}^{N_m}$. As described in Section 3.1,

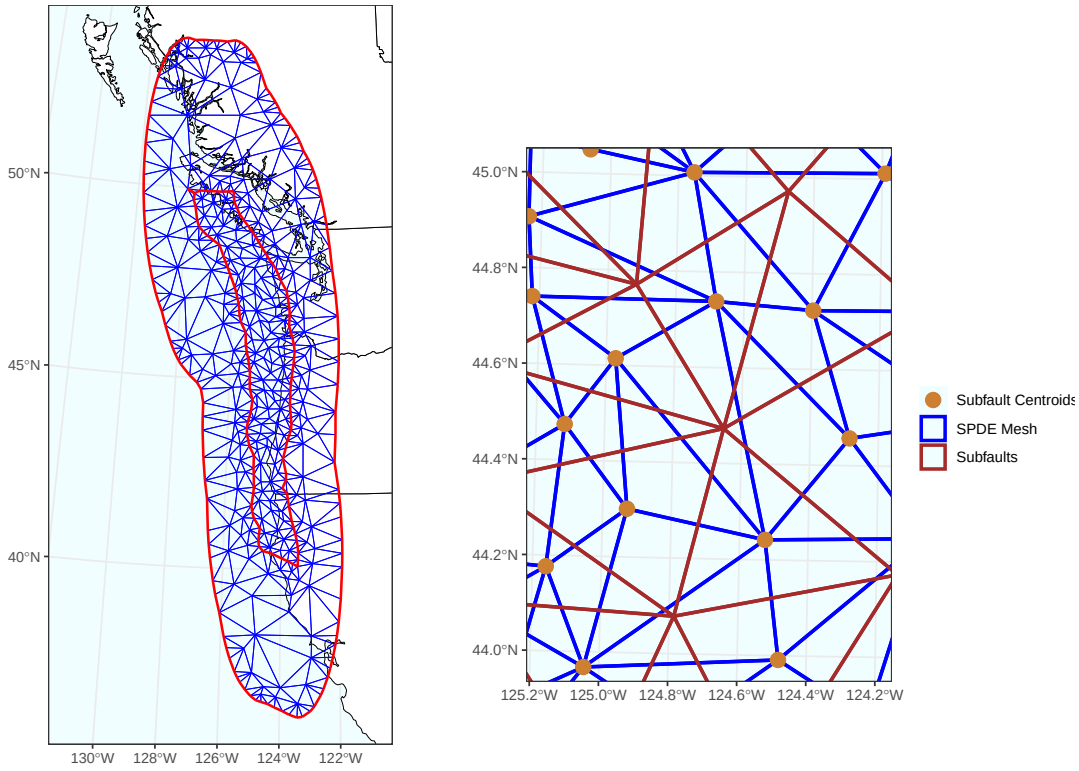

(a) (b)

Figure 3.2.1: In (a) the mesh used during the SPDE method is seen. The area inside the inner red boundary is the domain, $\mathcal{D}$, of interest. The SPDE mesh, the subfault geometry and the centroids of the subfaults are plotted together in (b).

subsidence can be predicted when the coseismic slip is known via the Okada model. In this setting coseismic slip is given for each of the $S = 188$ subfaults created in Section 2.3. Therefore let $\boldsymbol{s}_m \in \mathbb{R}^S$ be the $M = 12$ random slip vectors. To take the subsidence values calculated by the Okada model to the observed subsidence estimates, $\boldsymbol{y}_m$, an additive error, $\boldsymbol{\epsilon}_m \in \mathbb{R}^{N_m}$, based on the observed uncertainty data can be added. Thus it is possible to write the equation for the observed subsidence data as:

$$\boldsymbol{y}_m | \boldsymbol{s}_m, \boldsymbol{\epsilon}_m = G_m \boldsymbol{s}_m + \boldsymbol{\epsilon}_m \tag{3.4}$$

whereby terms of $\boldsymbol{\epsilon}_m$ are assumed to be independently normally distributed with a mean of 0 and variance given by the corresponding value in $\boldsymbol{v}_m$ squared. This means that $\boldsymbol{\epsilon}_m$ is multivariate normal with a zero mean vector, $\mathbf{0}_m \in \mathbb{R}^{N_m}$, and diagonal covariance matrix, Σ_m, with the diagonal given by the squared values of $\boldsymbol{v}_m$. That is:

$$\boldsymbol{\epsilon}_m | \boldsymbol{v}_m \sim \text{MVN}\left(\mathbf{0}_m, \Sigma_m\right). \tag{3.5}$$

The elements of the covariance matrix are explicitly given as:

$$\{\Sigma_m\}_{i,j} = \begin{cases} \{\boldsymbol{v}_m\}_i^2 & i = j \\ 0 & i \neq j. \end{cases} \tag{3.6}$$

where $\{\cdot\}_{i,j}$ is the element in row i and column j of a matrix. Similarly $\{\cdot\}_i$ is the element in row i of a column vector.

The Okada matrix $G_m \in \mathbb{R}^{N_m \times S}$ is the matrix calculated from the Okada model with a uniform slip over the entire fault, giving the surface deformation at the locations of the N_m data points for the m-th megathrust event.
The slip vector's are now appropriately modelled as the transformation of independent underlying GRFs, labelled X_m. Given that $X_m = \boldsymbol{x}_m$ the slips are given by:

$$\boldsymbol{s}_m|\lambda, \mu, \boldsymbol{x}_m = Te^{\mu\mathbf{1}+A\boldsymbol{x}_m}. \tag{3.7}$$

$T \in \mathbb{R}^{S\times S}$ is the taper matrix which is added to gradually decreases the spatial slip values near down-dip edge of the fault (the deeper, eastern edge) to provide a more realistic representation of how the the slip diminishes with depth as previously discussed. The matrix T is diagonal with elements explicitly given as:

$$\{T\}_{f,j} = \begin{cases} t(d_f|\lambda) & f = j \\ 0 & f \neq j \end{cases} \tag{3.8}$$

where d_f is the depth of the central point of the f-th sub fault and t is a taper function. The taper function used is

$$t(d|\lambda) = e^{-\lambda d} \tag{3.9}$$

where λ is a model parameter. Setting $\lambda = 0.123$ gives the taper shown in Figure 3.3.1. It is seen that this is 1 at the shallowest part of the CSZ and tapers to nearly 0 by 30 km.

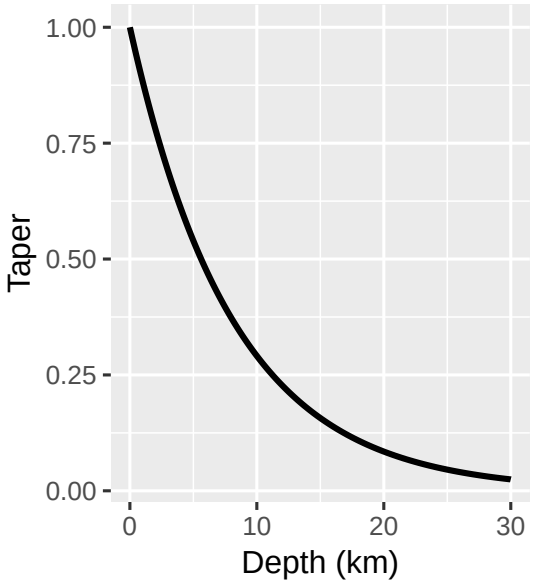

Figure 3.3.1: An example of the taper function with the free parameter fixed as $\lambda = 0.123$.

In (3.7) μ represents the mean untapered slip and $A \in \mathbb{R}^{S\times B}$ is the previously introduced projection matrix from the SPDE mesh to the GRF X_m.
As it has already been alluded to, the spatial fields, X_m, are assumed to be independently Gaussian with a Matérn covariance structure. Thus:

$$X_m = \boldsymbol{x}_m|\sigma^2, \kappa, \tau \sim \text{MVN}\left(\mathbf{0}, \sigma^2 Q^{-1}_{spde}(\kappa, \tau)\right). \tag{3.10}$$

where Q_{spde}^{-1} is the precision matrix of the GMRF representation of the underlying GRFs X_m, calculated via the SPDE method with κ and τ. When the matrix Q_{spde}^{-1} is actually calculated is accounts for the marginal variance, and thus σ^2 does not get fitted with the model. Instead Lindgren, Rue, and Lindström [61] showed that marginal variance can be calculated once the model has been fitted from τ and κ as:

$$\sigma^2 = \frac{1}{4\pi\kappa^2\tau^2}. \tag{3.11}$$

A final, empirically derived, parameter which is useful in understanding the range of the spatial field is the effective range ρ. This is also taken from Lindgren, Rue, and Lindström [61]. This is defined to be the distance at which the correlation has dropped to 0.1 and is calculated as:

$$\rho = \frac{\sqrt{8\nu}}{\kappa}. \tag{3.12}$$

3.4 A Shared Spatial Component Between Events

The first model could capture the behaviour of all the megathrust events independently, and has an implicit link between events via the shared spatial parameters κ and τ. However the random fields X_m are still independent of one another and can thus take completely different values. It has been recorded in events that the rupture patterns can be similar in subsequent events [64], thus indicating that the slip distribution could be similar throughout the history of CSZ megathrust events. To account for this a shared spatial component is added to the model. This model will thus be later refereed to as the "isotropic model with a shared spatial component", or just "model 2". This shared spatial random field will be denoted by W, and will be modelled with the SPDE method in the same way as the X fields. To account for W, some new notation is required. Specifically the parameters σ, κ and τ will now be related to either the X fields or the W field which will be denoted using subscript. That is σ_x, κ_x and τ_x are the parameters which control the X fields. Similarly σ_w, κ_w and τ_w will control the shared spatial field W.

Each slip vector will again be the transformation of its corresponding underlying spatial random field X_m which are all independent for each event. However now they will also be the transformation of the shared random field W. Given a realisation of the random fields, $X = \boldsymbol{x}_m$ and $W = \boldsymbol{w}$, the slip vector for each event can be written as:

$$\boldsymbol{s}_m|\lambda, \mu, \boldsymbol{x}, \boldsymbol{w} = Te^{\mu\mathbf{1}+A(\boldsymbol{w}+\boldsymbol{x}_m)} \tag{3.13}$$

where μ and T are the same mean untapered slip and the taper matrix as before. Similarly A is the same projection matrix previously described. It is worth noting that A is the same for both the shared spatial field and the independent fields, since W is modelled via the same SPDE mesh as X_m is. Once again it is assumed that all the underlying spatial random fields are Gaussian with $\mathbf{0}$ mean and a Matérn covariance structure, which allows the use of the SPDE method.

$$X_1, ..., X_M|\sigma_x^2, \kappa_x, \tau_x \sim \text{MVN}\left(\mathbf{0}, \sigma_x^2 Q_{spde}^{-1}(\kappa_x, \tau_x)\right); \tag{3.14}$$

$$W|\sigma_w^2, \kappa_w, \tau_w \sim \text{MVN}\left(\mathbf{0}, \sigma_w^2 Q_{spde}^{-1}(\kappa_w, \tau_w)\right). \tag{3.15}$$

The rest of the model is the same as before, that is (3.4) (3.5), (3.6), (3.7), (3.8) and (3.9) still hold. The marginal variances (σ_x^2 and σ_w^2) are calculated as expected once the model has been fitted, that is:

$$\sigma_x^2 = \frac{1}{4\pi\kappa_x^2\tau_x^2}, \qquad \sigma_w^2 = \frac{1}{4\pi\kappa_w^2\tau_w^2}. \tag{3.16}$$

Finally since there are two spatial fields, there will also be two effective spatial ranges, ρ_x and ρ_w. These are again the distance at which the correlation between points drops to 0.1 and are given by the empirically derived formulas in Lindgren, Rue, and Lindström [61]:

$$\rho_x = \frac{\sqrt{8\nu}}{\kappa_x}, \qquad \rho_w = \frac{\sqrt{8\nu}}{\kappa_w}. \tag{3.17}$$

3.5 Anisotropy of the Coseismic Slip Distribution

It has been shown that the correlation range of coseismic slip is different along the dip and strike directions [30] and as previously discussed it is common in CSZ coseismic slip modelling to account for their varying correlation ranges. This gives reason to add an anisotropic factor into the underlying spatial random fields. This model will as such be refereed to as the "anisotropic model with/without a shared spatial component" or for simplicity "model 3/4". Over the considered section of the CSZ (up to depths of 30 km) the strike angle varies from $-44.65°$ to $23.09°$, as seen in (a) of Figure 3.5.1.

The strike angle varies over the entire CSZ, which would imply that introducing non-stationary anisotropy[65] [66] into the spatial field would be the absolute best solution. However for simplicity the anisotropy is chosen to be geometric and stationary across the CSZ. This means that instead of assuming that the correlation function is the same in all directions as in the isotropic case, it is now allowed to vary with direction as well as distance. To achieve this a transformation matrix, H, is added into the underlying random field. This is implemented with the anisotropic version of the SPDE method[61], which is defined now via the SPDE:

$$(\kappa^2 - \nabla \cdot H\nabla)^{\frac{\alpha}{2}} Z(s) = \tau\mathcal{W}(s). \tag{3.18}$$

The transformation matrix, H, needs to be parameterised with at most two new parameters to account for the strike and the dip and to not over-parameterise the model. It also needs to "preserve volume" so that correlation isn't artificially added into the modelling.

The interpretation of H can be found through its eigenvalues and eigenvectors (see supplementary material from Thorson et al. [67]). The direction of anisotropy is given by the eigenvectors and the stretch of the spatial field in that direction is given by the corresponding eigenvalue. Therefore H is parameterised with its eigendecomposition:

$$H = [\boldsymbol{h}_1, \boldsymbol{h}_2]\Lambda[\boldsymbol{h}_1, \boldsymbol{h}_2]^T, \tag{3.19}$$

where $\boldsymbol{h}_1$, $\boldsymbol{h}_2$ are the two eigenvectors of H and Λ is the diagonal matrix with ϕ_1 and ϕ_2, the two eigenvalues on the diagonal. Since the strike angle is known across the CSZ, the direction of anisotropy is chosen to be fixed and in the direction of

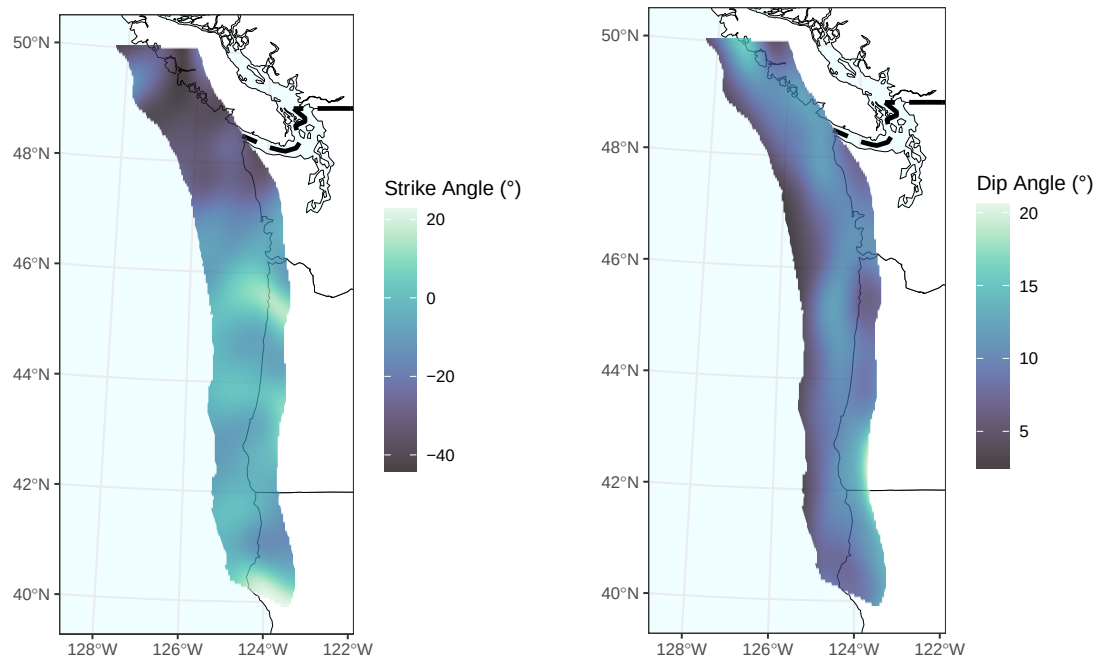

(a) (b)

Figure 3.5.1: In (a) the strike angle as given by the Slab2 data set is shown over the CSZ. In (b) the dip angle, again given by the Slab2 data set, is shown over the CSZ.

the average strike angle. This is $\theta_s = -12.14°$ and means that $\boldsymbol{h}_1$ should make an angle of θ_s, as measured clockwise from the lines of longitude (the vertical). $\boldsymbol{h}_1$ is also a normalized eigenvector and thus it can be explicitly written as:

$$\boldsymbol{h}_1 = \begin{bmatrix} -\sqrt{\frac{\tan(-\theta_s)^2}{\tan(-\theta_s)^2+1}} \\ \sqrt{\frac{1}{\tan(-\theta_s)^2+1}} \end{bmatrix} \approx \begin{bmatrix} -0.210 \\ 0.978 \end{bmatrix} \tag{3.20}$$

$\boldsymbol{h}_2$ is orthogonal to $\boldsymbol{h}_1$ and should also be normalised giving the explicit formula for $\boldsymbol{h}_2$ as:

$$\boldsymbol{h}_2 = \begin{bmatrix} \sqrt{\frac{\tan(90+\theta_s)^2}{\tan(90+\theta_s)^2+1}} \\ \sqrt{\frac{1}{\tan(90+\theta_s)^2+1}} \end{bmatrix} \approx \begin{bmatrix} 0.978 \\ 0.210 \end{bmatrix}. \tag{3.21}$$

Now the fact that the determinant of H needs to be 1 to preserve volume means that the product of the two eigenvalues also needs to be 1. This means that $\phi_1 = \frac{1}{\phi_2}$ and vice versa. Therefore the matrix Λ can be simplified to:

$$\begin{bmatrix} \phi & 0 \\ 0 & \frac{1}{\phi} \end{bmatrix} \tag{3.22}$$

where now the parameter $\phi > 0$ represents the stretch of the underlying spatial field in the direction of $\boldsymbol{h}_1$ and $\frac{1}{\phi}$ is the stretch in the direction of $\boldsymbol{h}_2$.

The independent megathrust model defined in Section 3.3, is exactly the same in the anisotropic setting except that the independent underlying X random fields now depend on ϕ as well. Explicitly that is:

$$X_1, ..., X_M | \sigma^2, \kappa, \tau, \phi \sim \text{MVN}\left(\mathbf{0}, \sigma^2 Q^{-1}_{spde}(\kappa, \tau, \phi)\right). \tag{3.23}$$

Evidently the effective range, ρ (3.12), of the spatial field will now be different in all directions. Therefore, as alluded to, the effective range in the direction of $\boldsymbol{h}_1$ (the strike direction) and its orthogonal (the dip direction) are given. These are calculated by multiplying ρ (3.12) by the previously introduced scaling parameter[5]:

$$\rho^{(strike)} = \phi \cdot \frac{\sqrt{8\nu}}{\kappa} \tag{3.24}$$

$$\rho^{(dip)} = \frac{1}{\phi} \cdot \frac{\sqrt{8\nu}}{\kappa}, \tag{3.25}$$

where $\nu = 1$ as before. Here the two values $\rho^{(strike)}$ and $\rho^{(dip)}$ will give the maximal and minimal effective ranges (with which one is which depending on the value of ϕ). In the shared component model, introduced in Section 3.4, the anisotropic parameters will be the same between the individual random fields, X_m and the shared random field W. The anisotropy is modelled in this way because it is assumed that the anisotropy is being introduced by the geometry of the CSZ (strike and dip angles), and not by specific earthquake rupture patterns. Thus having the same anisotropy over the individual X fields and the shared W field is required. Explicitly:

$$X_1, ..., X_M | \sigma_x^2, \kappa_x, \tau_x, \phi \sim \text{MVN}\left(\mathbf{0}, \sigma_x^2 Q^{-1}_{spde}(\kappa_x, \tau_x, \phi)\right) \tag{3.26}$$

$$W | \sigma_w^2, \kappa_w, \tau_w, \phi \sim \text{MVN}\left(\mathbf{0}, \sigma_w^2 Q^{-1}_{spde}(\kappa_w, \tau_w, \phi)\right). \tag{3.27}$$

The maximum and minimum effective ranges for the individual earthquakes and the shared random field are then given exactly as one would expect:

$$\rho_x^{(strike)} = \phi \cdot \frac{\sqrt{8\nu}}{\kappa_x}, \qquad \rho_x^{(dip)} = \frac{1}{\phi} \cdot \frac{\sqrt{8\nu}}{\kappa_x}, \tag{3.28}$$

$$\rho_w^{(strike)} = \phi \cdot \frac{\sqrt{8\nu}}{\kappa_w}, \qquad \rho_w^{(dip)} = \frac{1}{\phi} \cdot \frac{\sqrt{8\nu}}{\kappa_w}. \tag{3.29}$$

3.6 Priors

In this section the prior distributions which are placed on the model parameters are explained. The priors are consistent throughout all the models, which allows for the comparison of the affects of the specific model changes. Informative priors have been used where possible in order to guide the model towards the physical reality of the CSZ. This is important because the data set used is relatively small (429 data points), and so the prior distributions will have a noticeable impact on determining the posterior distribution. In cases where the use of an informative prior is not possible, priors which agree with previous studies and common practise are used.

[5]There was some lack of clarity over whether these the ranges should be multiplied by the eigenvalue or the square root of the eigenvalue. It was chosen to follow the work of [67] and just multiply by the eigenvalue.

3.6.1 SPDE Parameters

The parameters that control the basic use case of the SPDE method are κ and τ. Both the parameter sets which control the X spatial fields and the shared W field will have the same prior distribution. Thus $p(\kappa_x, \tau_x)$ and $p(\kappa_w, \tau_w)$ will here be referred to as $p(\kappa, \tau)$. Just remember that the priors will not be the same in reality as the parameters are different!

It is chosen to use the penalised complexity (PC) prior for κ and τ, which was introduced by Fuglstad et al. [68]. The idea of the penalised prior framework is to shrink the model to a base model to avoid overly complex models. In this case the range of the field ρ is "shrunk" towards infinity and the standard deviation σ is shrunk towards zero. This leads to four new hyper-parameters defined by:

$$\begin{aligned}\mathbb{P}(\rho < \rho_0) &= \alpha_1 \\ \mathbb{P}(\sigma > \sigma_0) &= \alpha_2.\end{aligned}$$

This says that the joint prior placed on τ and κ should be created such that the probability the range is less than ρ_0 is equal to α_1. Similarly the probability that the marginal standard deviation is greater than σ_0 should be equal to α_2. $\alpha_2 = 0.01$ is chosen. It is chosen to set $\sigma_0 = 1$ which means that the prior sets with probability 0.99 the marginal variance under 1. α_1 is chosen to be 0.5 and as such, ρ_0 is interpreted as the prior median effective range. The range hyper-parameter is chosen as $\rho_0 = 100$ which is in between the estimated correlations lengths in the strike and dip direction for a magnitude 9.0 event [30].

To implement the PC prior, Altay [69] was modified slightly and used.

3.6.2 Mean Untapered Slip Parameter

The parameter μ represents the mean untapered slip in the model, where e^{μ} is the value of the untapered slips when there is no contribution from the spatial fields. This is left as a flat prior as this is an intercept term which should be well-identifiable.

3.6.3 Taper Parameter

The taper parameter λ determines how aggressively the slips will be tapered towards zero on the down dip edge of the CSZ. Letting λ be gamma distributed with shape k and scale ζ, these hyper parameters can be chosen such that the probability the taper is 0.05 at depths greater than 20 km but less than 30 km is 0.95. This can be mathematically expressed as:

$$\begin{aligned}\mathbb{P}\left[t(d|\lambda, 20\,\text{km} \leq d \leq 30\,\text{km}) = 0.05\right] &= 0.95 \\ \mathbb{P}\left[t^{-1}(0.05|d = 30\,\text{km}) \leq \lambda \leq t^{-1}(0.05|d = 20\,\text{km})\right] &= 0.95.\end{aligned}$$

It is assumed that equally weighted tails are wanted, then this can be formulated as a system of two equations and two variables, from which the roots can be

found. The two equations are:

$$1 - \mathbb{P}\left[\lambda \leq -\frac{\log(0.05)}{30}\right] = 0.025$$
$$\mathbb{P}\left[\lambda \leq -\frac{\log(0.05)}{20}\right] = 0.975,$$

which can be expressed as the CDF of λ under the Gamma distribution assumption:

$$1 - F_\lambda\left(-\frac{\log(0.05)}{30}\right) = 0.025$$
$$F_\lambda\left(-\frac{\log(0.05)}{20}\right) = 0.975.$$

Solving this system of equations for the two hyper-parameters gives $k = 93.8$ and $\zeta = 0.00132$ such that lambda is distributed as:

$$\lambda \sim \Gamma(93.8, 0.00132), \tag{3.30}$$

and the taper function for when $\lambda = k \cdot \zeta = 0.123$ (the mean of this distribution) is shown in Figure 3.3.1.

3.6.4 Anisotropic Scaling Parameter

The parameter $\phi > 0$ gives the stretching of the underlying spatial fields, whereby $\phi = 1$ gives no anisotropic behaviour. It is also noted that ϕ is strictly positive. It is therefore chosen that the log of ϕ should be normally distributed (and thus ϕ is log-normally distributed) with a mean of 0 and a standard deviation chosen such that:

$$\mathbb{P}(0.5 < \phi < 2) = 0.95.$$

This is read as the probability that the stretch is between 0.5 and 2 is 0.95. The standard deviation which gives this condition is 0.38 and thus:

$$\log \phi \sim N(0, 0.38^2). \tag{3.31}$$

3.7 Posterior Density

Now that four models have been specified, the posterior density is required in each case to fit the parameters to the data. The observations $\boldsymbol{y}_m$ and $\boldsymbol{v}_m$ are given. The latent variable's $\boldsymbol{x}_m$ and $\boldsymbol{w}$ give the underlying spatial distributions. Finally the parameters, which will be some subset of $\boldsymbol{\theta} = \{\kappa_x, \tau_x, \kappa_w, \tau_w, \mu, \lambda, \phi\}$ define the model. The negative log likelihood is given as $-\ell = -log(\boldsymbol{L})$, where $\boldsymbol{L}$ is the likelihood. In every case the likelihood required is simply the posterior distribution.

3.7.1 Isotropic Independent Events Model

Starting with the simplest model that was defined in Section 3.3, the likelihood required will be given by the posterior $p(\boldsymbol{x}_1, ..., \boldsymbol{x}_M, \boldsymbol{\theta}|\boldsymbol{y}_1, ..., \boldsymbol{y}_M)$. In this case the parameter vector is,

$$\boldsymbol{\theta} = \{\kappa_x, \tau_x, \mu, \lambda\}. \tag{3.32}$$

Using the standard Bayesian approach, it is possible to write the posterior density as:

$$p(\boldsymbol{x}_1, ..., \boldsymbol{x}_M, \boldsymbol{\theta}|\boldsymbol{y}_1, ..., \boldsymbol{y}_M) \propto p(\boldsymbol{y}_1, ..., \boldsymbol{y}_M|\boldsymbol{x}_1, ..., \boldsymbol{x}_M, \boldsymbol{\theta})p(\boldsymbol{x}_1, ..., \boldsymbol{x}_M|\boldsymbol{\theta})p(\boldsymbol{\theta}) \tag{3.33}$$

where $p(\boldsymbol{y}_1, ..., \boldsymbol{y}_M|\boldsymbol{x}_1, ..., \boldsymbol{x}_M, \boldsymbol{\theta})$ is the observational density, $p(\boldsymbol{x}_1, ..., \boldsymbol{x}_M|\boldsymbol{\theta})$ is the density given to the latent variables, and $p(\boldsymbol{\theta})$ is the joint prior density of the parameters. To begin to find $p(\boldsymbol{y}_1, ..., \boldsymbol{y}_M|\boldsymbol{x}_1, ..., \boldsymbol{x}_M, \boldsymbol{\theta})$, one must look towards (3.4). It is seen that each element of $\boldsymbol{y}_m$ is a linear combination of a constant and a normally distributed variable with mean 0 and variance given by the corresponding values in $\boldsymbol{v}_m$ squared. Each element of $\boldsymbol{y}_m$ is therefore conditionally independent on the corresponding $\boldsymbol{x}_m$ and $\boldsymbol{\theta}$, with mean vector of $\boldsymbol{y}_m$ given by:

$$\mathbb{E}\left[\boldsymbol{y}_m|\boldsymbol{x}_m, \boldsymbol{\theta}\right] = \boldsymbol{u}_m = G_m T e^{\mu \mathbf{1}_m + A\boldsymbol{x}_m}, \tag{3.34}$$

and the covariance matrix given by Σ_m as defined in (3.6). This gives the density $p(\boldsymbol{y}_m|\boldsymbol{x}_m, \boldsymbol{\theta})$ as that of a multivariate normal variable with mean $\boldsymbol{u}_m$ and covariance matrix Σ_m:

$$p(\boldsymbol{y}_m|\boldsymbol{x}_m, \boldsymbol{\theta}) = (2\pi)^{-\frac{N_m}{2}}|\Sigma_m|^{-\frac{1}{2}} \exp\left(-\frac{1}{2}(\boldsymbol{y}_m - \boldsymbol{u}_m)^T\Sigma_m^{-1}(\boldsymbol{y}_m - \boldsymbol{u}_m)\right). \tag{3.35}$$

It is noted that in practise this density will be calculated as the product of N_m normal densities, whereby the mean and standard deviations are given by the elements of $\boldsymbol{u}_m$ and the diagonal elements of Σ_m. This arises from the fact that each element of $\boldsymbol{y}_m$ is assumed to be independent and thus Σ_m is a diagonal matrix. To find the joint density $p(\boldsymbol{y}_1, ..., \boldsymbol{y}_M|\boldsymbol{x}_1, ..., \boldsymbol{x}_M, \boldsymbol{\theta})$ it is noted that $\boldsymbol{y}_1, ..., \boldsymbol{y}_M$ are conditionally independent of each other, depending on the corresponding $\boldsymbol{x}_m$ and $\boldsymbol{\theta}$. Thus:

$$p(\boldsymbol{y}_1, ..., \boldsymbol{y}_M|\boldsymbol{x}_1, ..., \boldsymbol{x}_M, \boldsymbol{\theta}) = \prod_{m=1}^{M} p(\boldsymbol{y}_m|\boldsymbol{x}_m, \boldsymbol{\theta}). \tag{3.36}$$

The second part of (3.33), $p(\boldsymbol{x}_1, ..., \boldsymbol{x}_M|\boldsymbol{\theta})$, is the joint density function of the spatial fields X_m. Again these were assumed to be independent so the joint density can be split into the product of the individual field densities as:

$$p(\boldsymbol{x}_1, ..., \boldsymbol{x}_M|\boldsymbol{\theta}) = \prod_{m=1}^{M} p(\boldsymbol{x}_m|\boldsymbol{\theta}). \tag{3.37}$$

The individual random field densities, $p(\boldsymbol{x}_m|\boldsymbol{\theta})$, were assumed to be multivariate normally distributed, calculated via the SPDE approximation via a GMRF.

The prior density for the parameters $p(\boldsymbol{\theta})$ is decomposed into the product of the densities for each parameter:

$$p(\boldsymbol{\theta}) = p(\kappa_x, \tau_x) \cdot p(\mu) \cdot p(\lambda) \tag{3.38}$$

where the priors placed on each individual parameter were discussed in Section 3.6. Note this assumes that the parameters are independent of one another.

3.7.2 Isotropic Shared Spatial Component Model

In this model, defined in Section 3.4, the latent variable $\boldsymbol{w}$ is included. This introduced two new parameters, κ_w and τ_w, and such the new parameter vector of interest is:

$$\boldsymbol{\theta} = \{\kappa_x, \tau_x, \kappa_w, \tau_w, \mu, \lambda\}. \tag{3.39}$$

Accounting for the new latent variable the posterior required is now of the form:

$$p(\boldsymbol{x}_1, ..., \boldsymbol{x}_M, \boldsymbol{w}, \boldsymbol{\theta} | \boldsymbol{y}_1, ..., \boldsymbol{y}_M) \propto p(\boldsymbol{y}_1, ..., \boldsymbol{y}_M | \boldsymbol{x}_1, ..., \boldsymbol{x}_M, \boldsymbol{w}, \boldsymbol{\theta}) p(\boldsymbol{x}_1, ..., \boldsymbol{x}_M, \boldsymbol{w} | \boldsymbol{\theta}) p(\boldsymbol{\theta}). \tag{3.40}$$

The observation density, $p(\boldsymbol{y}_1, ..., \boldsymbol{y}_M | \boldsymbol{x}_1, ..., \boldsymbol{x}_M, \boldsymbol{w}, \boldsymbol{\theta})$ can again be written as the product of individual megathrust event densities, whereby each observed subsidence vector is conditionally independent $\boldsymbol{y}_m$, depending on $\boldsymbol{x}_m$, $\boldsymbol{w}$ and $\boldsymbol{\theta}$:

$$p(\boldsymbol{y}_1, ..., \boldsymbol{y}_M | \boldsymbol{x}_1, ..., \boldsymbol{x}_M, \boldsymbol{w}, \boldsymbol{\theta}) = \prod_{m=1}^{M} p(\boldsymbol{y}_m | \boldsymbol{x}_m, \boldsymbol{w}, \boldsymbol{\theta}). \tag{3.41}$$

Following the same logic as in the previous section, conditional on $\boldsymbol{x}_m, \boldsymbol{w}, \boldsymbol{\theta}$ the random vector $\boldsymbol{y}_m$ is the linear combination of a constant and a multivariate normal random vector with mean vector $\mathbf{0}$ and covariance matrix Σ_m and is therefore itself multivariate normal. The conditional mean vector of $\boldsymbol{y}_m$ is thus just the value of the constant:

$$\mathbb{E}[\boldsymbol{y}_m | \boldsymbol{x}_m, \boldsymbol{w}, \boldsymbol{\theta}] = \boldsymbol{u}_m = G_m T e^{\mu \mathbf{1}_m + A(\boldsymbol{x}_m + \boldsymbol{w})}, \tag{3.42}$$

and has the covariance matrix Σ_m as before. The density, $p(\boldsymbol{y}_m | \boldsymbol{x}_m, \boldsymbol{w}, \boldsymbol{\theta})$, will take exactly the same form as (3.35), except that now $\boldsymbol{u}_m$ is defined differently to incorporate $\boldsymbol{w}$. The latent density, $p(\boldsymbol{x}_1, ..., \boldsymbol{x}_M, \boldsymbol{w} | \boldsymbol{\theta})$ will be decomposed into a product of the densities of each individual random field, owing to the fact that they are all conditionally independent on $\boldsymbol{\theta}$. That is:

$$p(\boldsymbol{x}_1, ..., \boldsymbol{x}_M, \boldsymbol{w} | \boldsymbol{\theta}) = p(\boldsymbol{w} | \boldsymbol{\theta}) \cdot \prod_{m=1}^{M} p(\boldsymbol{x}_m | \boldsymbol{\theta}). \tag{3.43}$$

These individual densities are again calculated via the SPDE method. It is important to note that the precision matrix calculated will be the same for all the X fields, but will be different for the shared field W as it has different defining parameters: κ_w and τ_w. Once again the prior density $p(\boldsymbol{\theta})$ will be the product of the densities of the parameters:

$$p(\boldsymbol{\theta}) = p(\kappa_x, \tau_x) \cdot p(\kappa_w, \tau_x) \cdot p(\mu) \cdot p(\lambda), \tag{3.44}$$

where the individual parameter priors are defined in Section 3.6.

3.7.3 Anisotropic Models

The two anisotropic models (with and without a shared spatial component) will have a very similar posterior density as their isotropic counterparts. In the model without a shared component the parameter set is:

$$\boldsymbol{\theta} = \{\kappa_x, \tau_x, \mu, \lambda, \phi\}. \tag{3.45}$$

The decomposition of the posterior (3.33) still holds, and the observational equation (3.36) also holds. Furthermore the form of the latent variable equation (3.37) holds, but now the density of each individual spatial field $p(\boldsymbol{x}_m|\boldsymbol{\theta})$ is now calculated via the anisotropic version of the SPDE method[61]. The joint prior density is again the product of the individual parameter densities and takes the form:

$$p(\boldsymbol{\theta}) = p(\kappa_x, \tau_x) \cdot p(\mu) \cdot p(\lambda) \cdot p(\phi), \tag{3.46}$$

where these individual densities are defined in Section 3.6. The final model which incorporates anisotropy and a shared spatial component, uses the full parameter set:

$$\boldsymbol{\theta} = \{\kappa_x, \tau_x, \kappa_w, \tau_w, \mu, \lambda, \phi\}. \tag{3.47}$$

The posterior has exactly the same expression as its isotropic counterpart, that is it is defined via (3.40), (3.41), (3.43). The difference being that $p(\boldsymbol{x}_m|\boldsymbol{\theta})$ and $p(\boldsymbol{w}|\boldsymbol{\theta})$ are now calculated via the anisotropic version of the SPDE method[61] using the parameter ϕ. Finally the joint prior density is, as expected, the product of the independent parameter densities:

$$p(\boldsymbol{\theta}) = p(\kappa_x, \tau_x) \cdot p(\kappa_w, \tau_w) \cdot p(\mu) \cdot p(\lambda) \cdot p(\phi). \tag{3.48}$$

3.8 Template Model Builder

In order to fit the model, i.e. find the parameters which maximise the joint likelihood, the R package *TMB* [62] is used. This package allows for the fitting of models such as the ones described here by letting the user specify the joint likelihood of the data and the random effects as a C++ file. When evaluating the joint likelihood for maximisation the random effects are automatically integrated out and the Laplace approximation is used to calculate the remaining marginal likelihood. The use of C++ allows for the fast computation of derivatives which will significantly speed up the model fitting procedure, important when working with a model that includes many random effects such as the ones just described. In addition to the model fitting *TMB* is used to calculate an estimate of the joint precision matrix of all the model parameters which is then used to simulate the parameters and random effects of the fitted models.

CHAPTER

FOUR

INFERENCE ABOUT HISTORICAL FULL FAULT RUPTURES

In this chapter the results of model fitting are presented and discussed. As mentioned previously, TMB is used to create the objective function for the posterior distribution and then a standard R optimiser is used to fit the model. Most usefully, TMB can be used to find an estimate of the joint precision matrix for all the model parameters and latent random effects. This joint precision matrix, Q_θ, can then be used to simulate from the GMRF which describes the latent random effects, conditional on the fixed model parameters. Thus n_{sims} simulations for each of the fixed parameters and each of the random effects can be drawn and used to calculate statistics for these variables of interest. This is mainly the coseismic slip distribution of each earthquake and model and the subsidence estimate which follows naturally from the slips distribution.

4.1 Inference about Model Parameters

The fixed parameters of each model are discussed in turn here. The mean, median, standard deviation, lower 2.5% quantile and upper 97.5% quantile of the each parameter calculated from the $n_{sims} = 1000$ simulations of the posterior is given in tabular format. A histogram of the more interpretable parameters for each model is also given, with vertical lines showing the 95% empirical confidence interval and the mean of the distribution. For ease of reading the mean and median are given again in each histogram. Furthermore, parameters of interest are investigated further and presented in a relevant way, for example the tapers which the draws of λ give will be shown.

The fixed parameter vector for model 1 is $\boldsymbol{\theta}_1 = \{\lambda, \mu, \tau, \kappa\}$ where τ and κ, which are SPDE parameters, are used to calculate the understandable parameters of ρ, the spatial range, and σ^2, the spatial marginal variance. The statistics from the posterior for the first model can be seen in Table 4.1.1. When looking at the second model, the fixed parameter vector now includes two lots of SPDE parameters to account for the new shared spatial field, whereby X is the independent field for each megathrust event and W is the field shared across all megathrust events. The parameter vector is thus $\boldsymbol{\theta}_2 = \{\lambda, \mu, \tau_X, \kappa_X, \tau_W, \kappa_W\}$. Estimates from the

Parameter	Mean	Median	SD	Lower 2.5%	Upper 97.5%
λ	0.116	0.115	0.00872	0.0999	0.135
μ	3.63	3.62	0.148	3.33	3.92
κ	0.0119	0.0115	0.00292	0.00732	0.0185
τ	48.1	47.0	11.3	30.4	72.9
ρ	252	246	62.5	153	386
σ^2	0.282	0.271	0.0815	0.158	0.462

Table 4.1.1: Distributional results for the parameters of the isotropic model without a shared spatial component. Values are calculated from 1000 simulations of the posterior.

Parameter	Mean	Median	SD	Lower 2.5%	Upper 97.5%
λ	0.122	0.121	0.0118	0.103	0.142
μ	3.58	3.59	0.313	3.08	4.09
κ_X	0.0845	0.0367	0.171	0.00386	0.310
τ_X	462	187	1090	20.9	1830
κ_W	0.0176	0.0158	0.00873	0.00729	0.0349
τ_W	35.7	32.2	17.4	14.6	68.6
ρ_X	201	77.2	382	9.14	734
σ_X^2	0.00522	0.00193	0.0110	0.000173	0.0208
ρ_W	201	180	101	81.0	388
σ_W^2	0.348	0.316	0.169	0.148	0.646

Table 4.1.2: The distributional results of 1000 draws from the posterior distribution of the isotropic model with a shared spatial component.

posterior distribution for these parameters for the second model are seen in Table 4.1.2.

With the addition of geometric anisotropy into the modelling, came the addition of two new parameters: θ_s and ϕ. The angle of rotation, θ_s, was fixed to $-12.14°$, and therefore is naturally not included in these results. Instead only ϕ is reported, alongside the other defining variables and their useful re-parameterisations. The defining parameter vector for the third model is thus $\boldsymbol{\theta}_3 = \{\lambda, \mu, \tau, \kappa, \phi\}$. Useful re-parameterisations are the marginal variance, σ^2 (3.11), as before, but now the effective range, ρ, needs to be calculated in the two anisotropic directions. These have been called the "strike" and "dip" directions as they aim to capture these geological geometries. The calculation is given in (3.25). The posterior estimates for these parameters relating to the third model can be seen in Table 4.1.3.

The final model and the one with the most parameters is the anisotropic model with a shared spatial component. The defining parameters for this model are $\boldsymbol{\theta}_4 = \{\lambda, \mu, \tau_X, \kappa_X, \tau_W, \kappa_W, \psi\}$ and as previously the marginal variance can be calculated for each of the spatial fields. Moreover the spatial range, ρ, will be calculated four times, twice for each spatial field to account for the strike and dip directions of anisotropy in each one. The estimates from the posterior distribution for this model are seen in Table 4.1.4.

Parameter	**Mean**	**Median**	**SD**	**Lower 2.5%**	**Upper 97.5%**
λ	0.115	0.115	0.00811	0.102	0.128
μ	3.61	3.61	0.145	3.37	3.85
κ	0.0130	0.0126	0.00346	0.00797	0.0196
τ	44.0	41.8	11.9	27.1	66.3
ϕ	0.844	0.773	0.326	0.437	1.45
$\rho^{(strike)}$	206	174	125	76.2	437
$\rho^{(dip)}$	304	288	108	159	503
σ^2	0.293	0.286	0.0824	0.177	0.447

Table 4.1.3: The distributional results for the parameters and their understandable re-parameterisations for the anisotropic model without a shared spatial component. Calculated from 1000 draws of the posterior distribution.

Parameter	**Mean**	**Median**	**SD**	**Lower 2.5%**	**Upper 97.5%**
λ	0.121	0.121	0.0116	0.0999	0.144
μ	3.58	3.58	0.290	3.04	4.14
κ_X	0.0768	0.0358	0.122	0.00302	0.437
τ_X	383	160	714	11.5	2040
κ_W	0.0187	0.0169	0.00902	0.00662	0.0423
τ_W	33.0	28.9	16.8	11.9	76.8
ϕ	0.803	0.761	0.305	0.342	1.50
$\rho_X^{(strike)}$	145	60.5	338	4.80	724
$\rho_X^{(dip)}$	259	101	485	7.56	1720
$\rho_W^{(strike)}$	157	125	119	33.9	450
$\rho_W^{(dip)}$	256	221	140	80.9	619
σ_X^2	0.00721	0.00254	0.0144	0.000122	0.0469
σ_W^2	0.365	0.324	0.185	0.134	0.800

Table 4.1.4: Distributional results for the parameters and their useful re-parameterisations for the anisotropic model with a shared spatial component. Values are calculated from 1000 draws from the posterior.

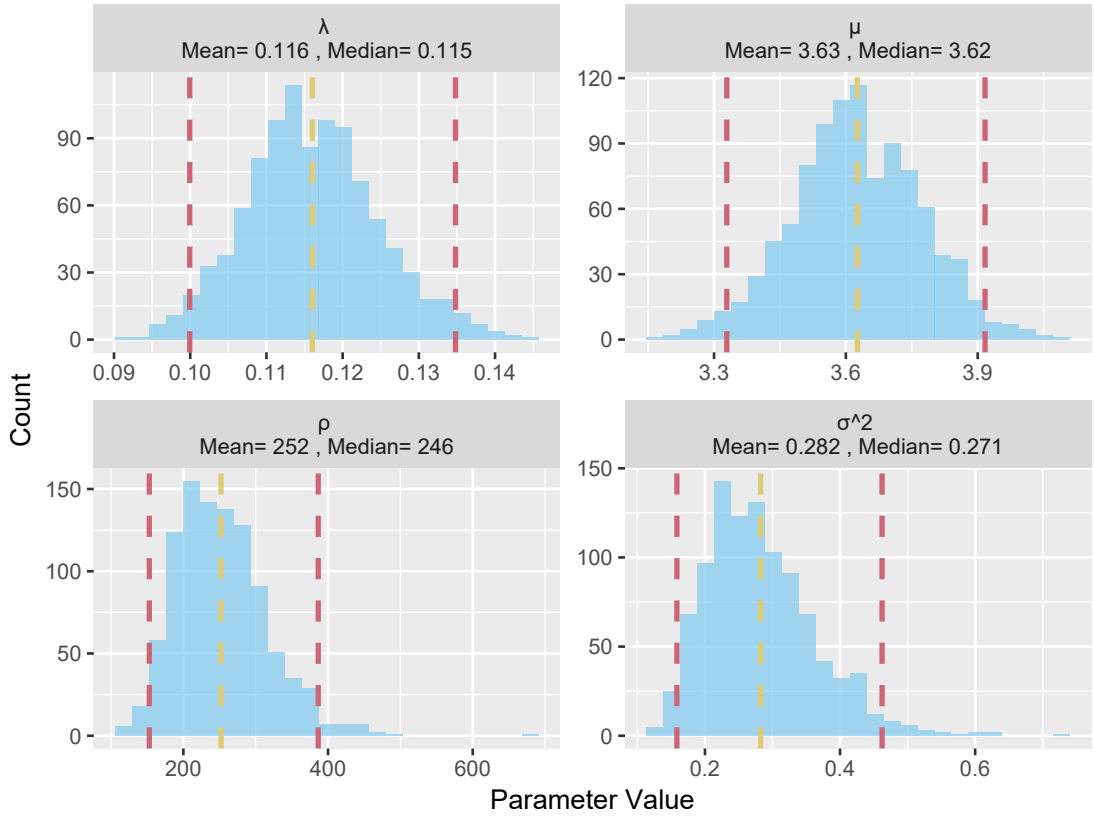

Figure 4.1.1: Histograms for the parameters in isotropic model without a random shared spatial component. The vertical red dashed lines are the lower 2.5% and upper 97.5% quantiles respectively. The vertical yellow dashed line is the mean of the empirical distribution.

The histograms for more interpretable parameters in all the models are now shown. In the first model λ, μ, ρ and σ^2 are the parameters shown, and can be seen in Figure 4.1.1. In the second model the parameters that give most interpretability, namely the taper parameter λ, the mean untapered slip, μ, the range parameters for both fields ρ_X, ρ_W and the marginal variances for both spatial fields, σ^2_X, σ^2_W, are shown in Figure 4.1.2. Next the empirical distribution for the useful parameters for the third model are shown in Figure 4.1.3. These parameters are the taper parameter λ, the mean untapered slip μ, the effective range ρ in both the strike and dip directions, the marginal variance, σ^2 and finally the anisotropic stretch factor. Finally the empirical distribution of the interpretable parameters for the fourth model are given in Figure 4.1.4. This is includes 9 parameters. The usual parameters, λ for the taper and μ for the mean untapered slip and then all the required permutations of the effective range, ρ, and marginal variance, σ^2 to account for two spatial field and two main directions of anisotropy.

In the isotropic model without a shared component there does not seem to be much skew in any of the parameters and that the optimisation process has found a stable maximum. This is similar for all the parameters of the anisotropic model without a shared component, except that the anisotropic stretch factor and the effective range in the strike direction seem to have a slight right skew. On the other hand the two models with a shared component display very heavy tails for some of

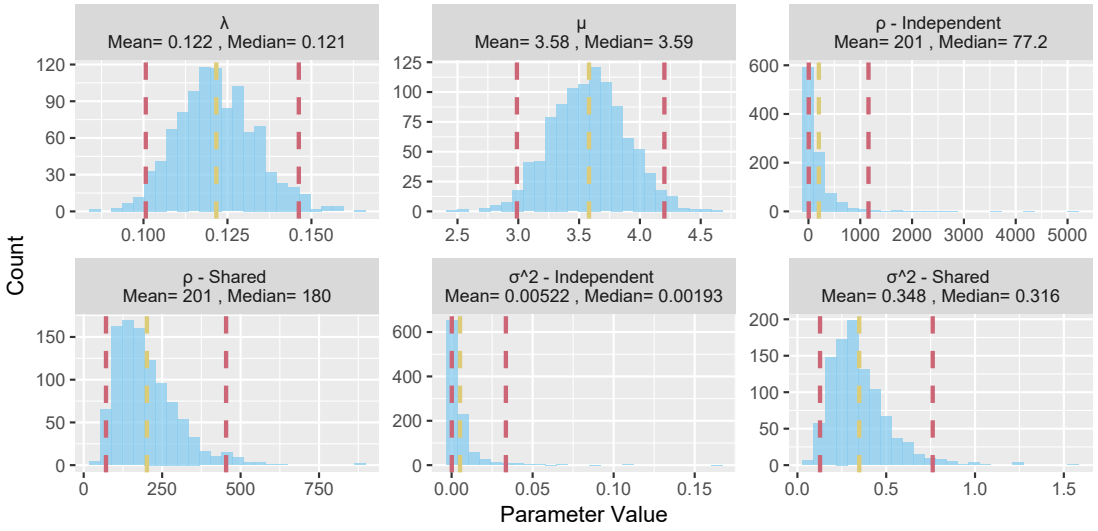

Figure 4.1.2: Histograms for the parameters in the isotropic model with a shared spatial component. The vertical red dashed lines are the lower 2.5% and upper 97.5% quantiles respectively. The vertical yellow dashed line is the mean of the empirical distribution.

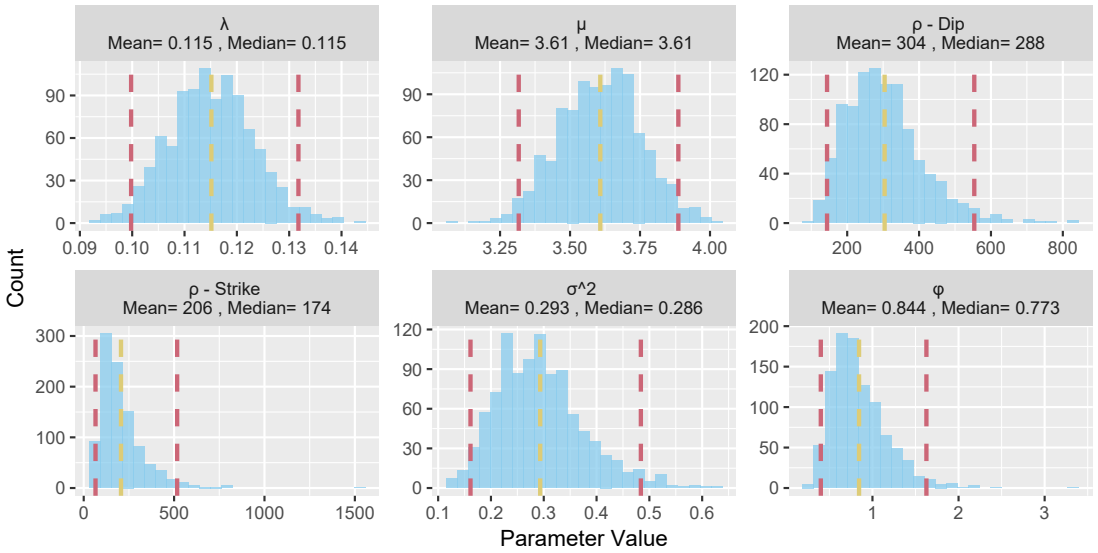

Figure 4.1.3: Histograms for the parameters in the anisotropic model without a shared spatial component. The vertical red dashed lines are the lower 2.5% and upper 97.5% quantiles respectively. The vertical yellow dashed line is the mean of the empirical distribution.

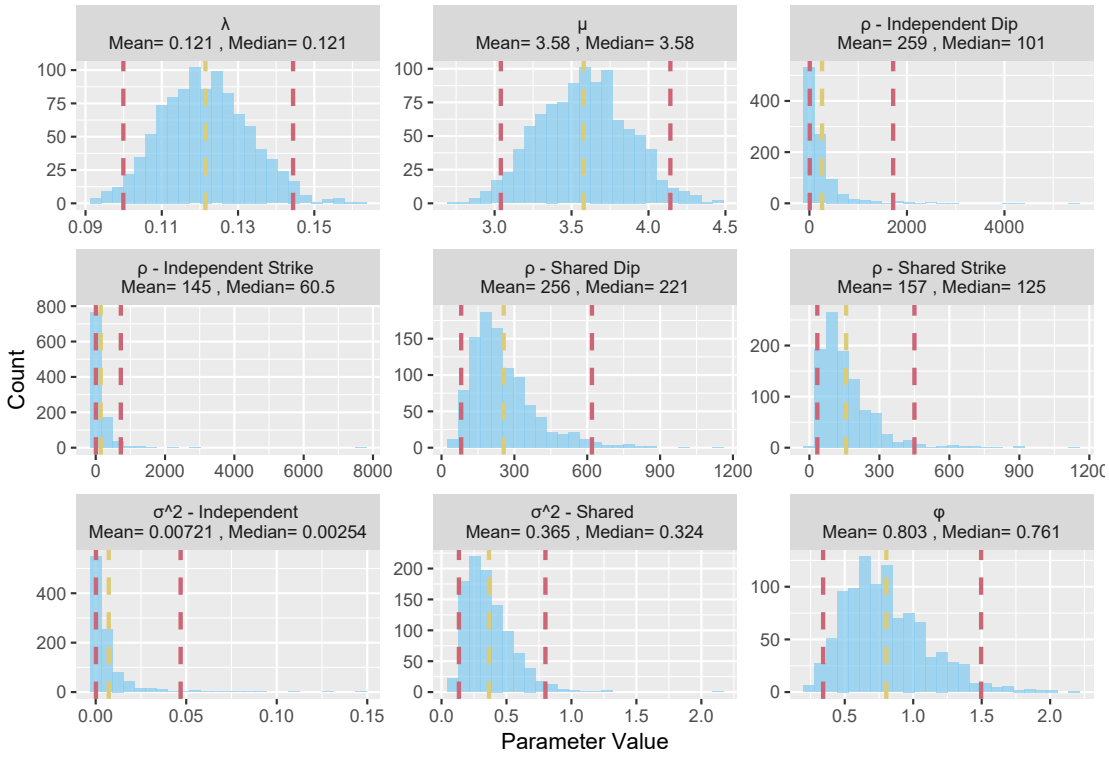

Figure 4.1.4: Histograms for the parameters in the anisotropic model with a shared spatial component. The vertical red dashed lines are the lower 2.5% and upper 97.5% quantiles respectively. The vertical yellow dashed line is the mean of the empirical distribution.

the parameters, most notably in the parameters related to the independent spatial fields, X. This could perhaps be a result of using a prior on the SPDE parameters which has heavy tails. Another very interesting observation about the models with a shared component is that the shared marginal variance is approximately 100 times bigger than that of the independent components. This suggests that these models have converged upon a coseismic slip distribution which is essentially the same for all the megathrust events. This is interesting as it suggests that full fault ruptures have been very similar for the all historic events, and that one coseismic slip distribution can fit the subsidence estimates well. The mean untapered slip has been estimated as roughly 3.6 m for all the models, and is the parameter which changes the least between models. The median effective range for the first model is 246 km, 180 km for the shared component of the second model, 174 km in the strike direction for the third model (this is the smaller of the two effective ranges) and 125 km in the strike direction of the shared component in the fourth model. This also means that the subfault geometery, whereby the average distance between between adjacent subfaults is 25.6 km, is just over 1/6-th the size of the smaller effective range in the modelling. This average distance between subfault centroids represents the average side length in the SPDE mesh. In her masters thesis, Røste [70] concluded that a maximum side length of 1/12-th the spatial range is sufficient for the Gaussian usage of the SPDE approach. The subfault geometry that has been created is therefore twice as coarse as it should optimally be but is the finest possible with the computational restraints.

4.1.1 Prior vs Posterior Taper Function

The taper function over the CSZ depths for each model is shown in Figure 4.1.5. The median taper and equi-tailed 95% empirical confidence interval are shown as well as the prior which was placed on the λ parameter. This shows that the taper parameter is well defined in the optimisation process of all the models as the confidence interval for each one lines up with the prior placed on lambda. This also suggests that the prior was very important here, and that the data has not affected the fitting of the taper much (if at all). This gives more evidence that the taper encodes important scientific information which cannot be seen through the data set alone. The only difference between the models is that the shared component models give a slightly wider confidence interval which aligns more with the prior than in the non-shared component models.

4.1.2 Prior vs Posterior Anisotropic Stretch

It is interesting and relevant to investigate the stretch parameter in the two anisotropic models a bit further. Specifically what does the median and 95% empirical confidence interval look like. To do this the correlation ellipse's are plotted for the median value of ϕ, the lower 2.5% quantile and the upper 97.5% quantile. Additionally the prior is illustrated by two dashed orange ellipses. Remember that the prior was set such that the stretch factor is between 0.5 and 2 with 95% probability which is not a very constrictive prior at all. The plots for both anisotropic models can be seen in Figure 4.1.6. It is seen that the median stretch in both models makes the dip directions have a longer effective range. This

is odd as the literature quite clearly suggests that the correlation along the strike direction is greater than in the dip direction [30]. It is probably the result of combining the geometric anisotropy with the taper function which already affects the coseismic slip distribution mainly in the dip direction. It is also seen that in both models the inferred confidence interval gives more stretch in the dip direction than the prior gives, but less in the strike direction.

4.2 CSZ Coseismic Slip Distributions

In this section the inferred coseismic slip distributions for each of the megathrust events and models are displayed. The slip distribution is given over the fault geometry which was introduced in Section 2.3. This means that in the illustrations the slip distribution is given as the mean across each triangular subfault. The slips were created from the $n_{sims} = 1000$ draws from the model posterior distributions using the appropriate formulas as given in Section 3. The draws of the fixed parameters were just given in Section 4.1, and a summary of the draws for the spatial random effects can be seen in Appendix B.1. Then the mean and standard deviation for each triangular sub fault are calculated. Firstly the mean slip distribution for all the models is given. The mean slip for the isotropic models can be seen in Figure 4.2.1 and for the anisotropic models in Figure 4.2.2.

It is seen that the coseismic slip distributions for the models without a shared spatial component vary with each megathrust event quite a lot. The distributions seem to depend on how much subsidence was estimates for each event in the central latitudinal region. These models have inferred the highest amounts of slip, with the anisotropic model giving over 30 m of mean slip for event $T10$. As expected the models with a shared spatial component do not show must variation in coseismic slip distribution between the megathrust events. They are also more conservative with their maximal mean slip values: 20 m of slip was inferred in the central latitudinal regions. This region seems to accumulate the highest concentration of slip, which occurs potentially from the high subsidence estimates from this region (Figure 2.2.2). It is worth mentioning that to account for the most southern subsidence estimates, all the models shown here have placed slip values of roughly 10 m on the south western tip of the CSZ fault. However the southern end of the CSZ fault is actually made up of several faults and is hard to analyse in a way which agree with the geology of the region [71], and as such no hard conclusions should be drawn here. Next the standard deviation is given for the slip distributions. The SD for the isotropic models can be seen in Figure 4.2.3. Then the SD of the slip distribution for the anisotropic models can be seen in Figure 4.2.4.

Here the expected pattern occurs, the SD tracks with the mean slip. The maximal SD is approximately 17 m, which means that the distribution of cosesimic slip can vary quite a lot between realisation for all these models.

4.3 Subsidence Prediction

With the slip distribution calculated for each model it is now possible to predict surface subsidences for all the models through the use of the Okada model, as introduced in Section 3.1. This is firstly done for the locations of collected subsidence

estimates, which will give an indication of how well the model captures reality. The subsidence prediction at each location can be calculated for the $n_{sims} = 1000$ draws from the posterior slip distribution and then a mean subsidence prediction found. These are plotted against latitude, with the real subsidence estimates also shown. These plots for the isotropic models can be seen in Figure 4.3.1 and in Figure 4.3.2 for the anisotropic models.

It is seen that all the models predict the subsidence at collection locations quite well. there is no real stand out bad models or megathrust events, which suggests that this type of modelling can explain the geological evidence well. The slip distribution can also be used to predict the subsidence over the entire CSZ region. To calculate subsidence across the entire fault, a new okada matrix is required. This is calculated such that it gives the surface deformation at a grid of points on the surface. This grid has 25 equally spaced locations in the longitude direction from $-128°$ to $-123°$ and then 50 equally spaced locations in the latitudinal direction ranging from $40°$ to $50°$. Computing the Okada matrix was a compuational bottleneck here and is the limiting factor in choosing the resolution of this grid. Ideally this would be as fine as possible. An illustration of this grid can be seen in Figure 4.3.3. Then 1000 subsidence estimates can be created for each point, and as such the mean and standard deviation in subsidence predictions can be calculated. Firstly the mean subsidence for the isotropic models can be seen in Figure 4.3.4 and in Figure 4.3.5 for the anisotropic models. Note that in all of these full fault subsidence prediction plots the colour scales have been fixed for all the models to allow for easier comparisons.

The relationships of subsidence predictions across the region between models is the same as it was for the coseismic slip distribution: the shared spatial component models are more conservative in their predictions. The really interesting thing here is the band of uplift predicted by all models on and slightly to the west of the shallower edge of the CSZ fault. This is the same across all the events, and would indicate the potential for a tsunami to have been triggered in all the events. In the most extreme case, an uplift of approximately 10 m would cause a highly powerful tsunami. Secondly the standard deviation of the subsidence predictions across the entire fault is calculated and shown in Figure B.2.1 in the Appendix for the isotropic models and in Figure B.2.2 of the Appendix for the anisotropic models.

4.4 Inference about Event Magnitude Distributions

Another interesting quantity to calculate from the slip distribution is the moment magnitude of the megathrust events that draws from the coseismic slip distributions would produce. This is done with the known equations [72]:

$$\begin{aligned} M_0 &= r \sum_{i=1}^{S} A_i s_i \\ M_w &= \frac{2}{3}(\log_{10}(M_0) - 9.1), \end{aligned} \tag{4.1}$$

where r is the rigidity of the rock and set to 3×10^{10} here. A_i is the area of each subfault and s_i is the mean slip across that subfault. M_w will be magnitude of the megathrust event as we are familiar with, and M_0 gives the earthquake

moment. Since 1000 realisations of the slip distribution have been calculated for each megathrust event, it is then possible to calculate 1000 magnitudes for each megathrust event. From this the empirical distribution can be found for each event and presented as a histogram. This illustration is seen in Figure 4.4.1 for the first model. For the second model these histograms are seen in Figure 4.4.2. For the anisotropic model without a shared spatial component the empirical distributions of megathrust magnitudes can be seen in Figure 4.4.3. Finally the empirical distribution of megathrust magnitudes for the anisotropic model with a shared spatial component is shown in Figure 4.4.4.

As expected the distributions in the shared component models are very similar, and give a mean and median magnitude of just of $M_w 9.0$ for all the events. There is a bit more variation in the other models, however they too also have central estimates of around 9.0 for all the events. In the models without the shared spatial components the 95% empirical confidence interval varies considerably across the events. In general it can be said that the events with more subsidence predictions, $T1$, $T4$ and $T5$ for example, have a much narrower confidence interval width than those events which have poor subsidence estimate coverage, $T12$, for example. The 1700AD event is predicted to have a magnitude of $M_w 9.0$ by all the models which agrees with the current literature [73, 35].

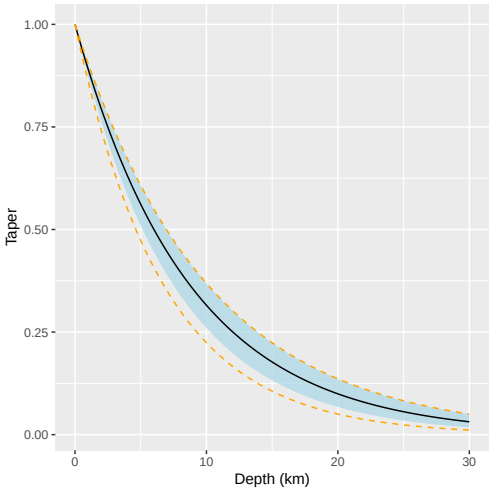

(a) Model 1

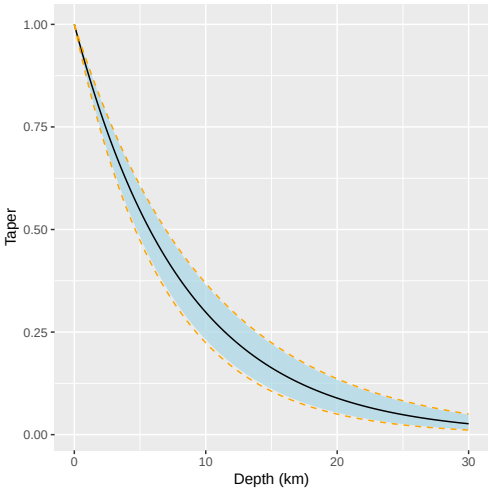

(b) Model 2

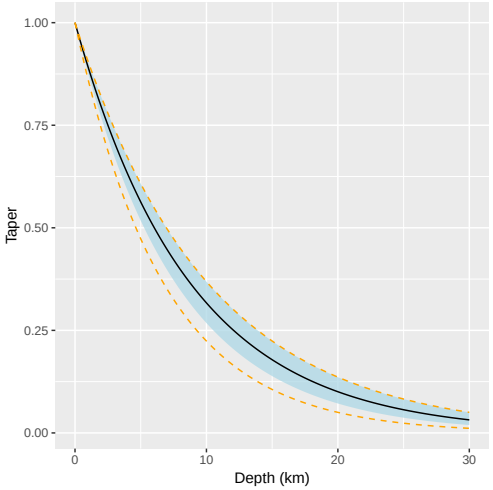

(c) Model 3

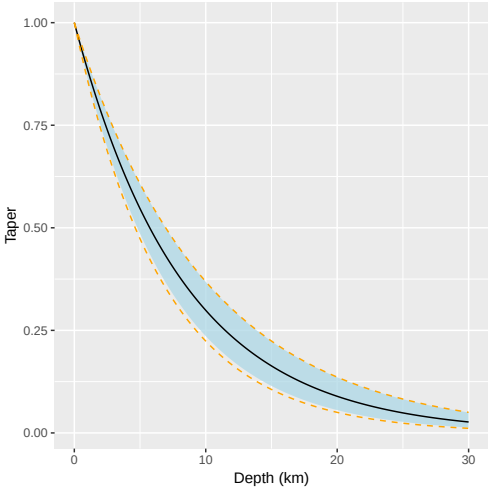

(d) Model 4

Figure 4.1.5: These plots show the statistics of the taper function calculated from draws from the λ function for each of the four models. The black line is the taper given by the median λ value. The blue band is created by filling in the region between the taper given by the lower 2.5% quantile of λ and the upper 97.5% quantile of λ, thus showing an equi-tailed, empirical 95% confidence interval. The orange dashed lines give the equi-tailed 95% confidence interval from the prior placed on λ.

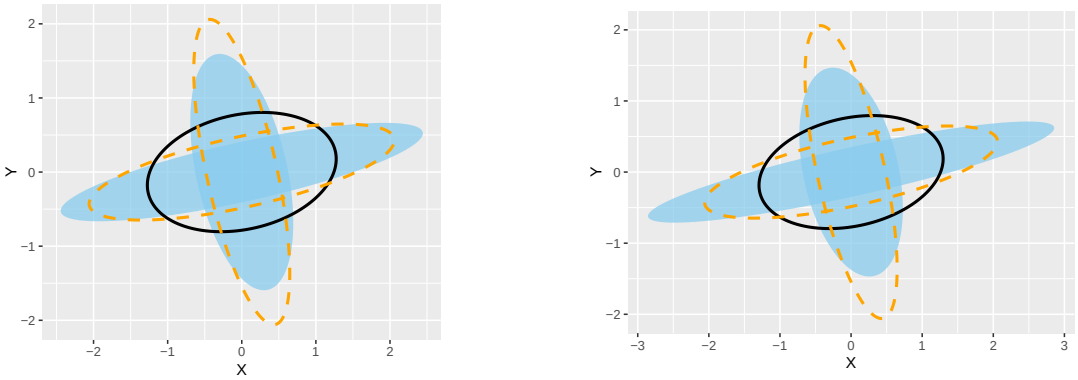

(a) Model 3

(b) Model 4

Figure 4.1.6: These plots illustrate the statistics on the anisotropic stretch factor. the black line gives the anisotropic ellipse for the median value of ϕ. The two blue ellipses represent the 2.5% and 97.5% quantiles for ϕ and thus any stretch in between these can be thought of as within the empirical 95% confidence interval. Further the orange dashed lines show the correlation ellipses for the prior placed on ϕ, which gives $\mathbb{P}(0.5 < \phi < 2) = 0.95$.

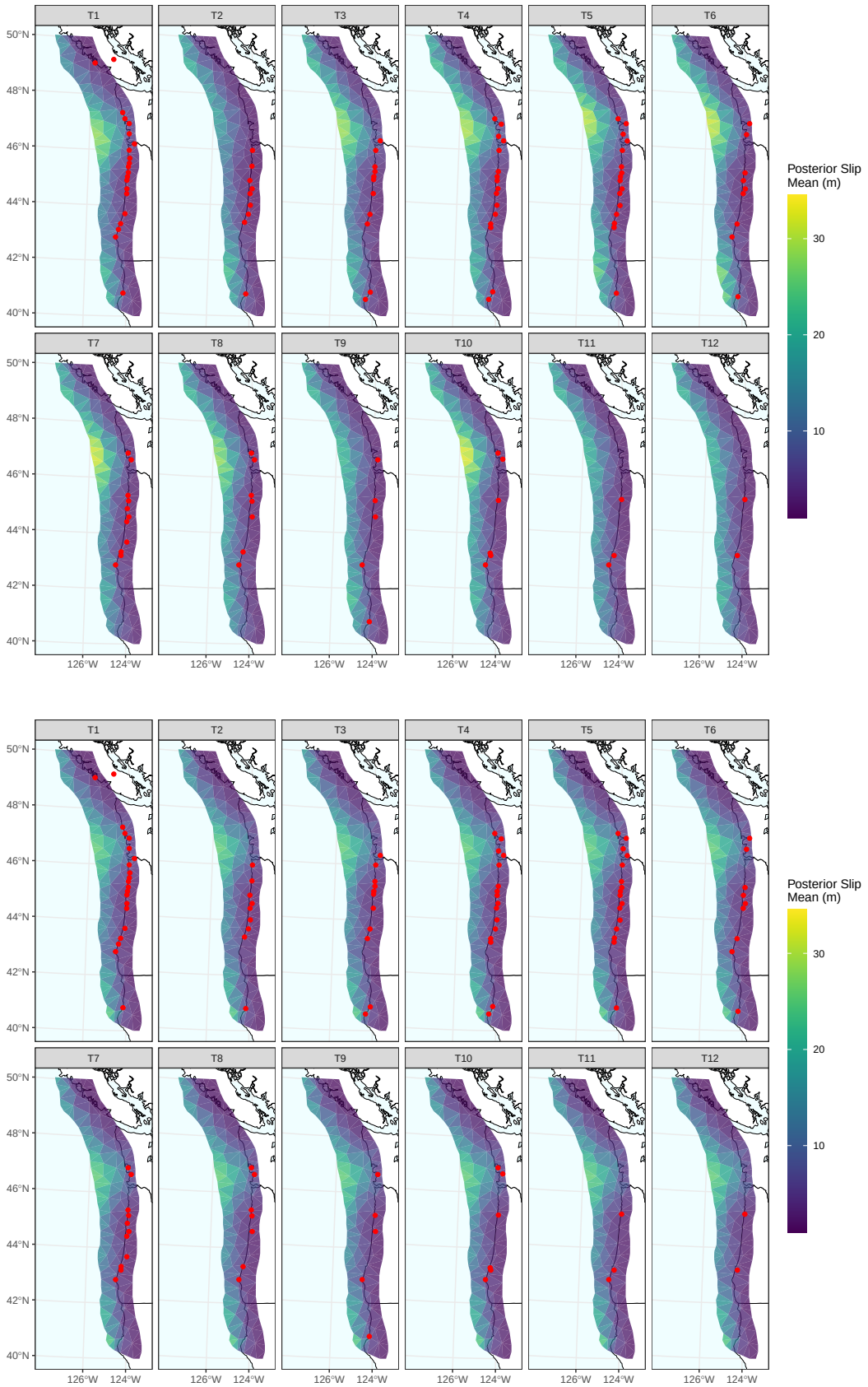

Figure 4.2.1: Above is the mean of the slip distribution for the first model and below is the mean of the slip distribution for the second model. The red points represent the locations of observed subsidence estimates.

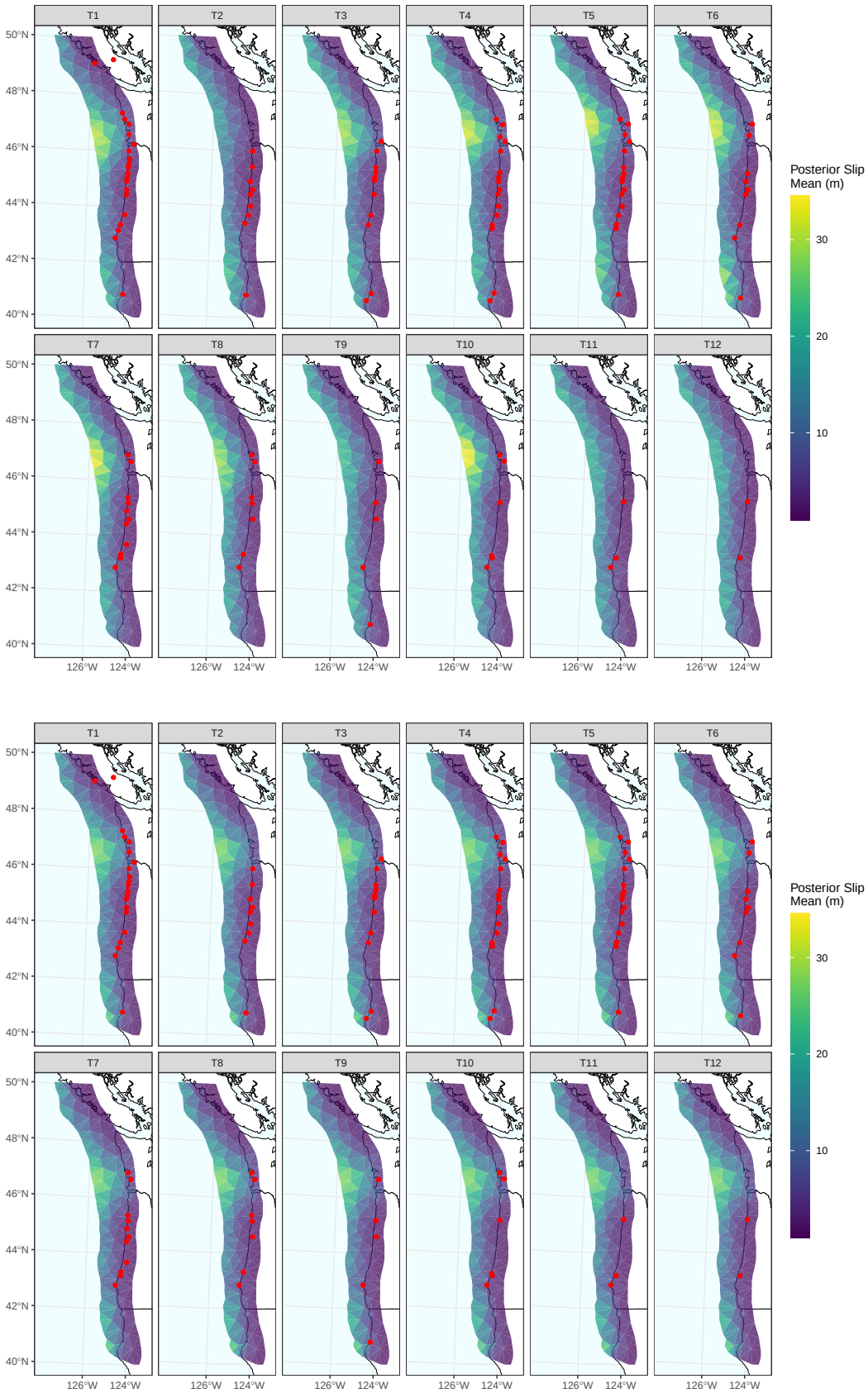

Figure 4.2.2: Above is the mean of the slip distribution for the third model and below is the mean of the slip distribution for the fourth model. The red points represent the locations of observed subsidence estimates.

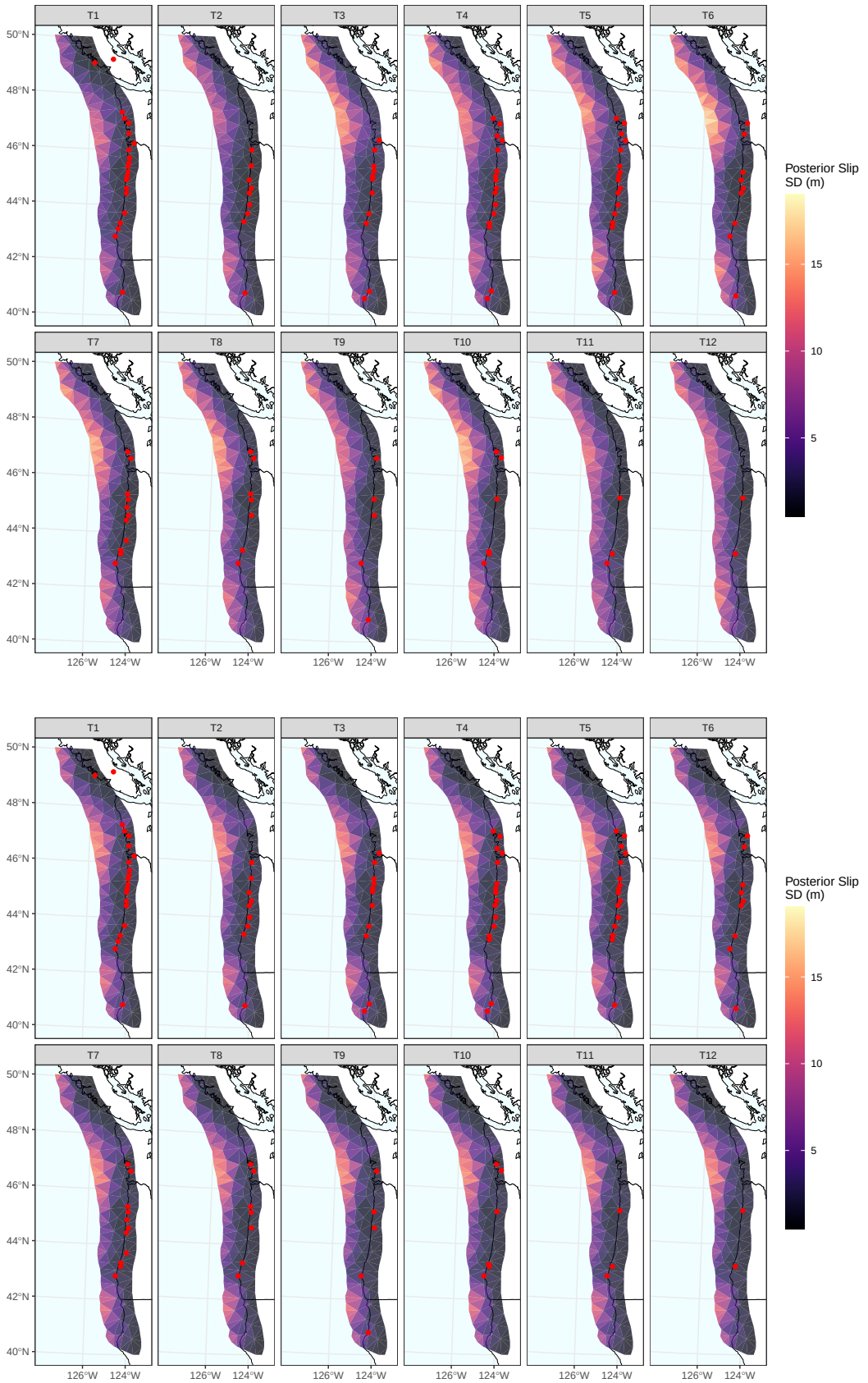

Figure 4.2.3: Above is the standard deviation of the slip distribution for the first model and below is the standard deviation of the slip distribution for the second model. The red points represent the locations of observed subsidence estimates.

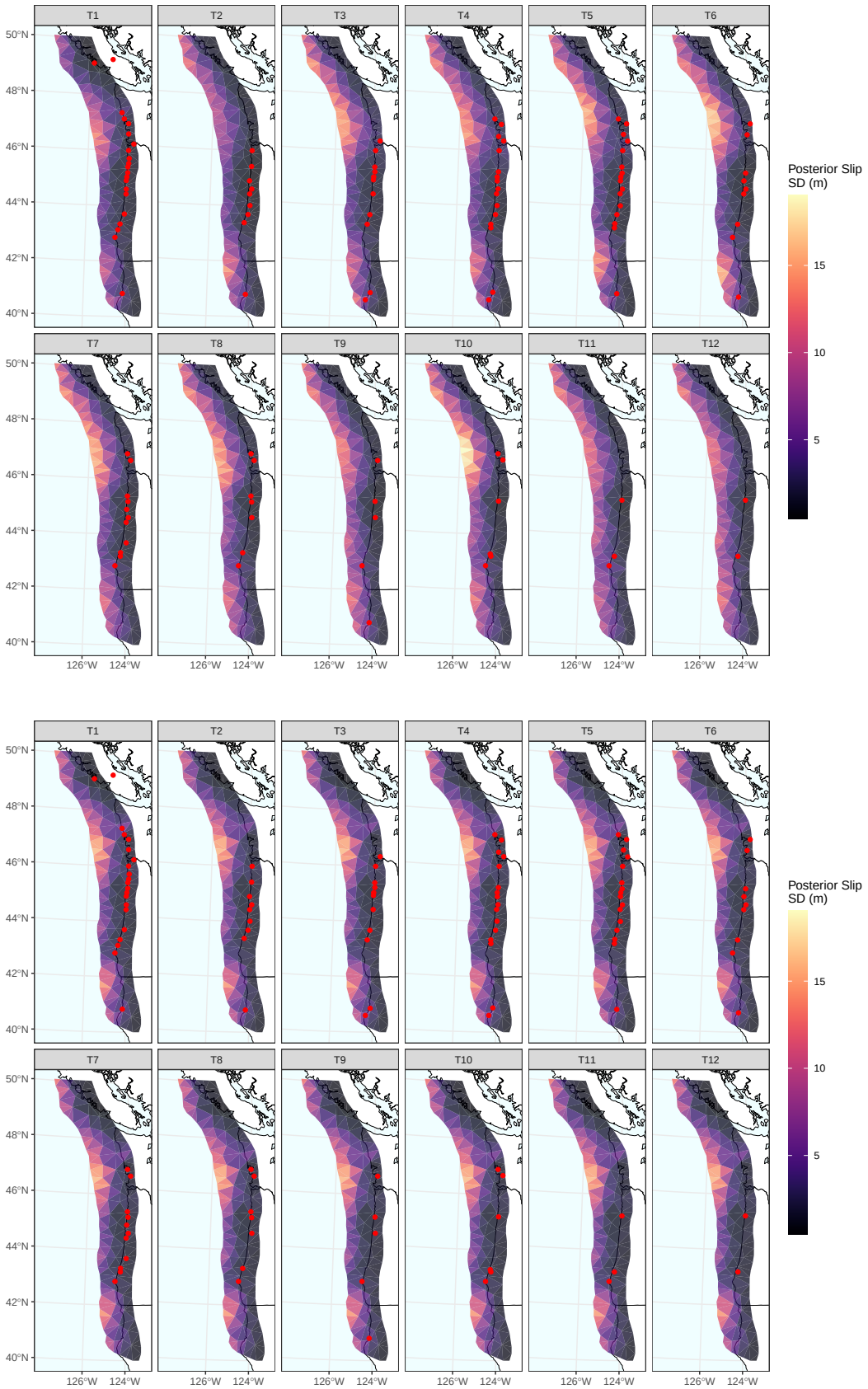

Figure 4.2.4: Above is the standard deviation of the slip distribution for the third model and below is the mean of the slip distribution for the fourth model. The red points represent the locations of observed subsidence estimates.

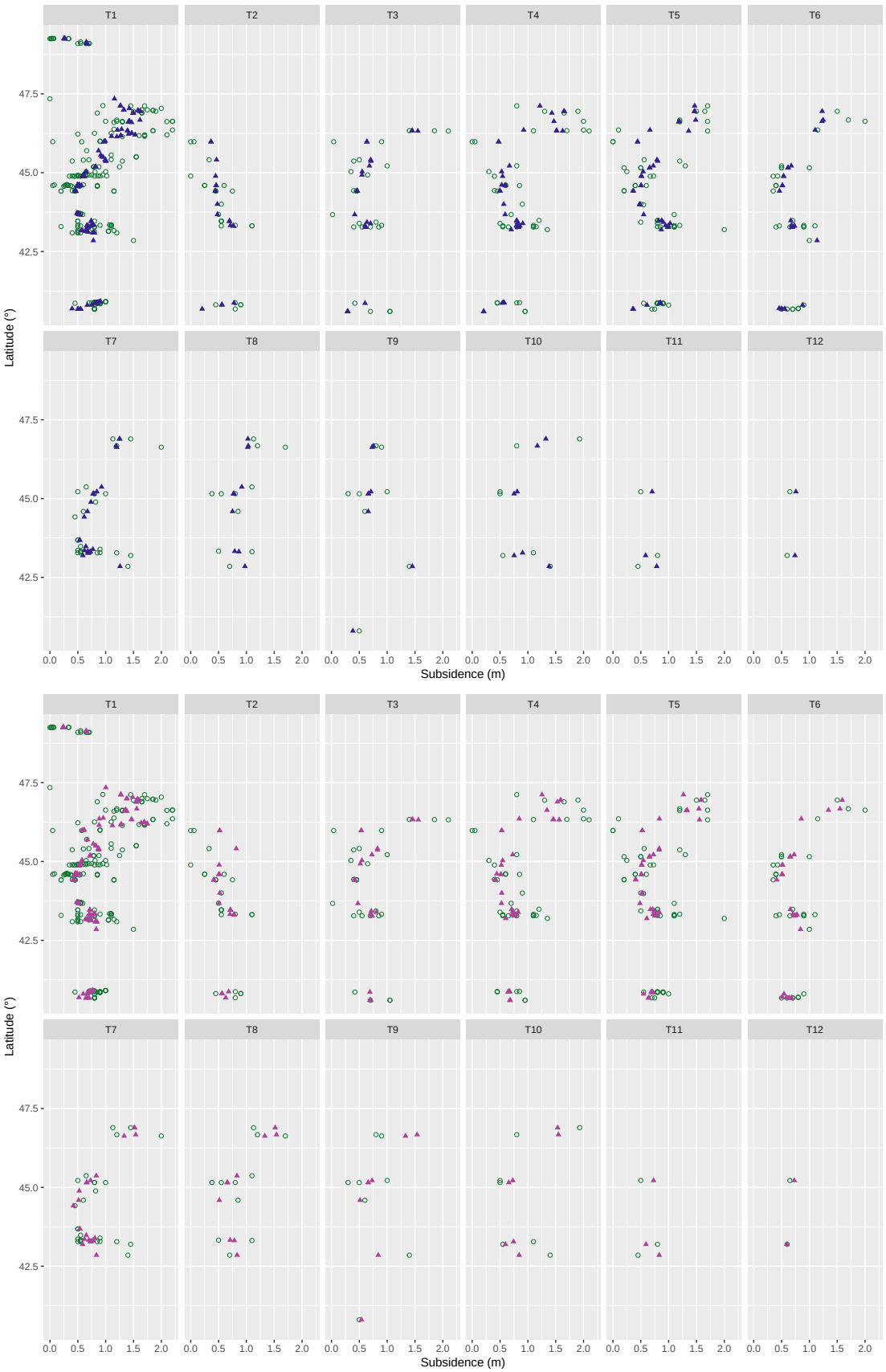

Figure 4.3.1: Above is the subsidence prediction at the locations of the data points for the first model and below is the same but for the second model. The triangles represent the model predictions and the hollow green circles are the original subsidence estimates.

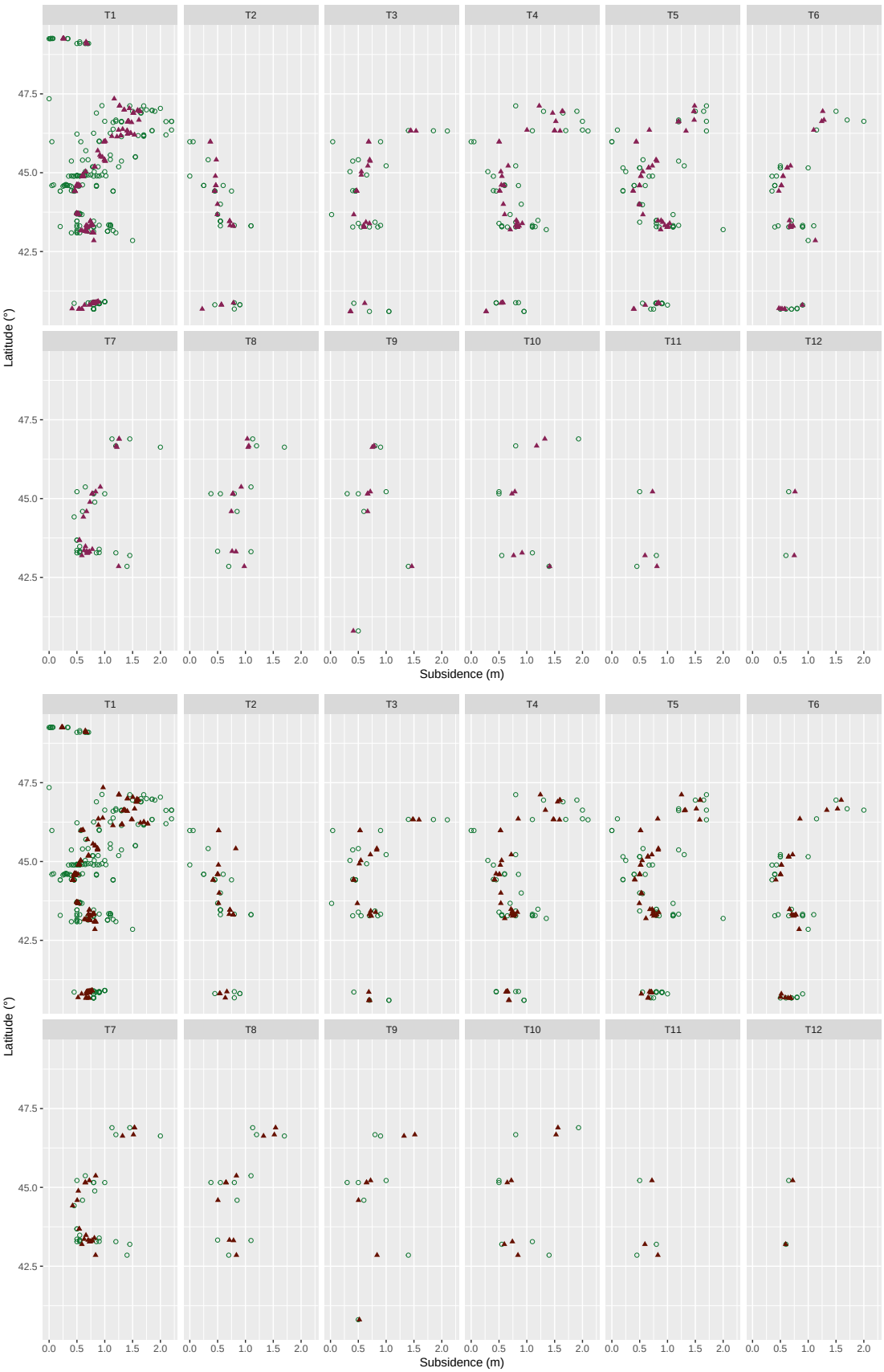

Figure 4.3.2: Above is the subsidence prediction at the locations of the data points for the third model and below is the same but for the fourth model. The triangles represent the model predictions and the hollow green circles are the original subsidence estimates.

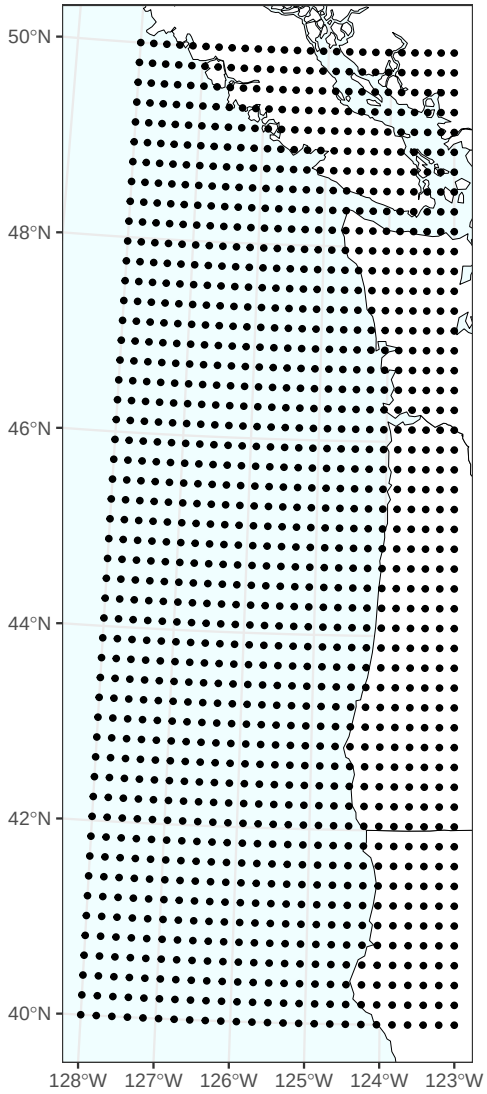

Figure 4.3.3: A grid of points at which subsidence will be evaluated for all the models.

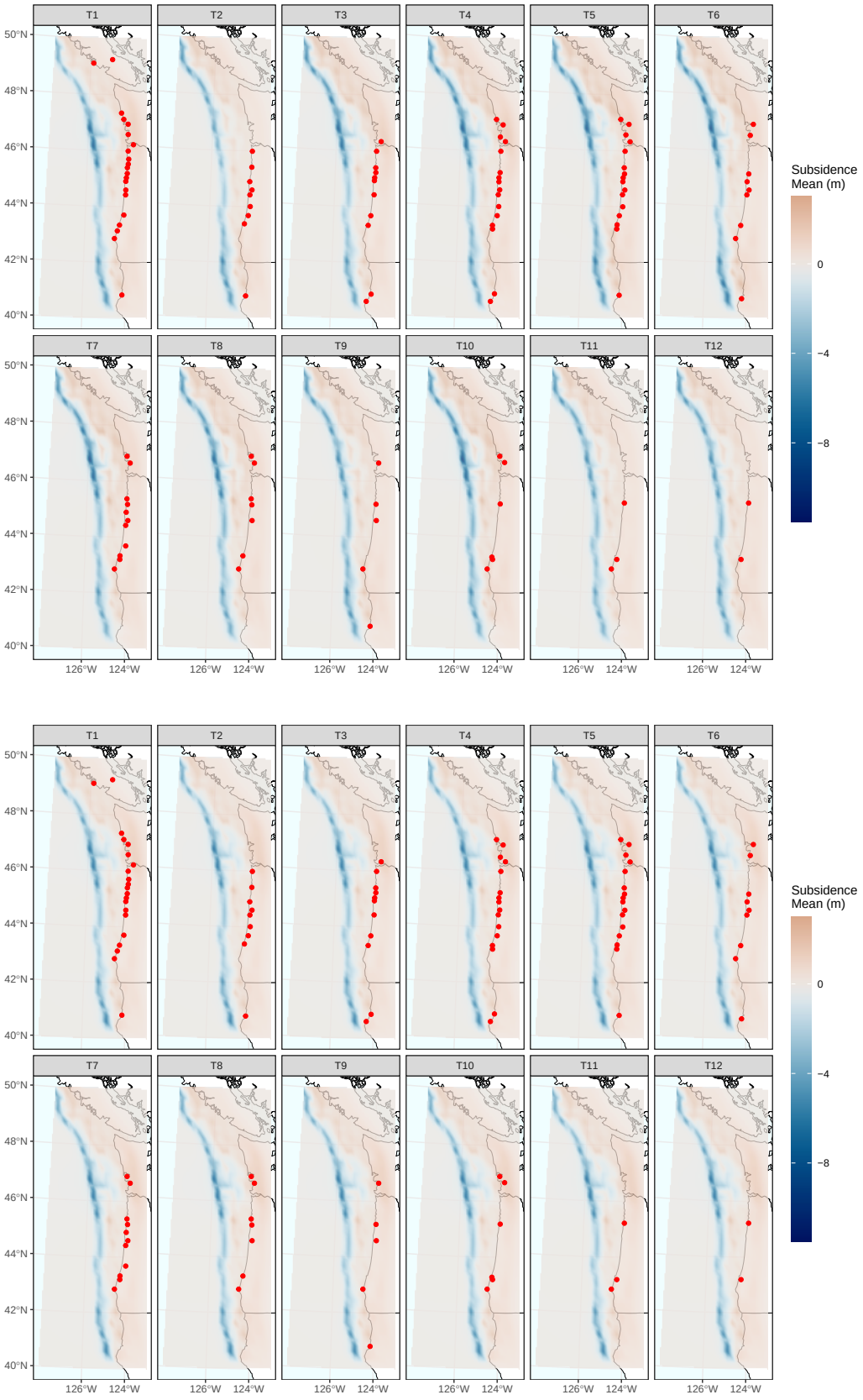

Figure 4.3.4: The mean subsidence across the whole fault calculated for the first model is shown above, and below is the same information but for the second model. The red points give the locations of subsidence estimates. The illustration was created by linearly interpreting the subsidence predictions made on the grid shown in Figure 4.3.3.

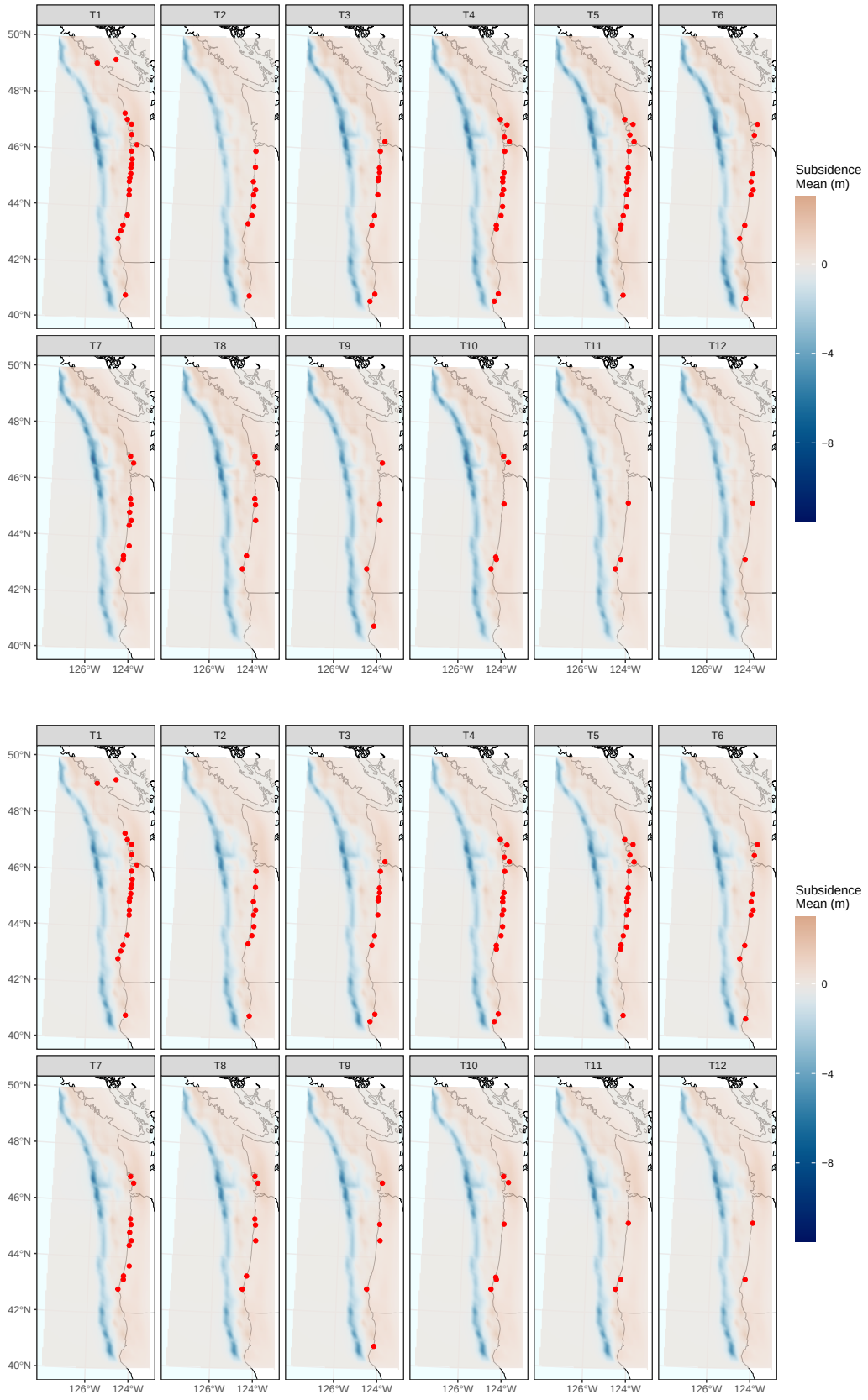

Figure 4.3.5: The mean subsidence across the whole fault calculated for the third model is shown above, and below is the same information but for the fourth model. The red points give the locations of subsidence estimates. The illustration was created by linearly interpreting the subsidence predictions made on the grid shown in Figure 4.3.3.

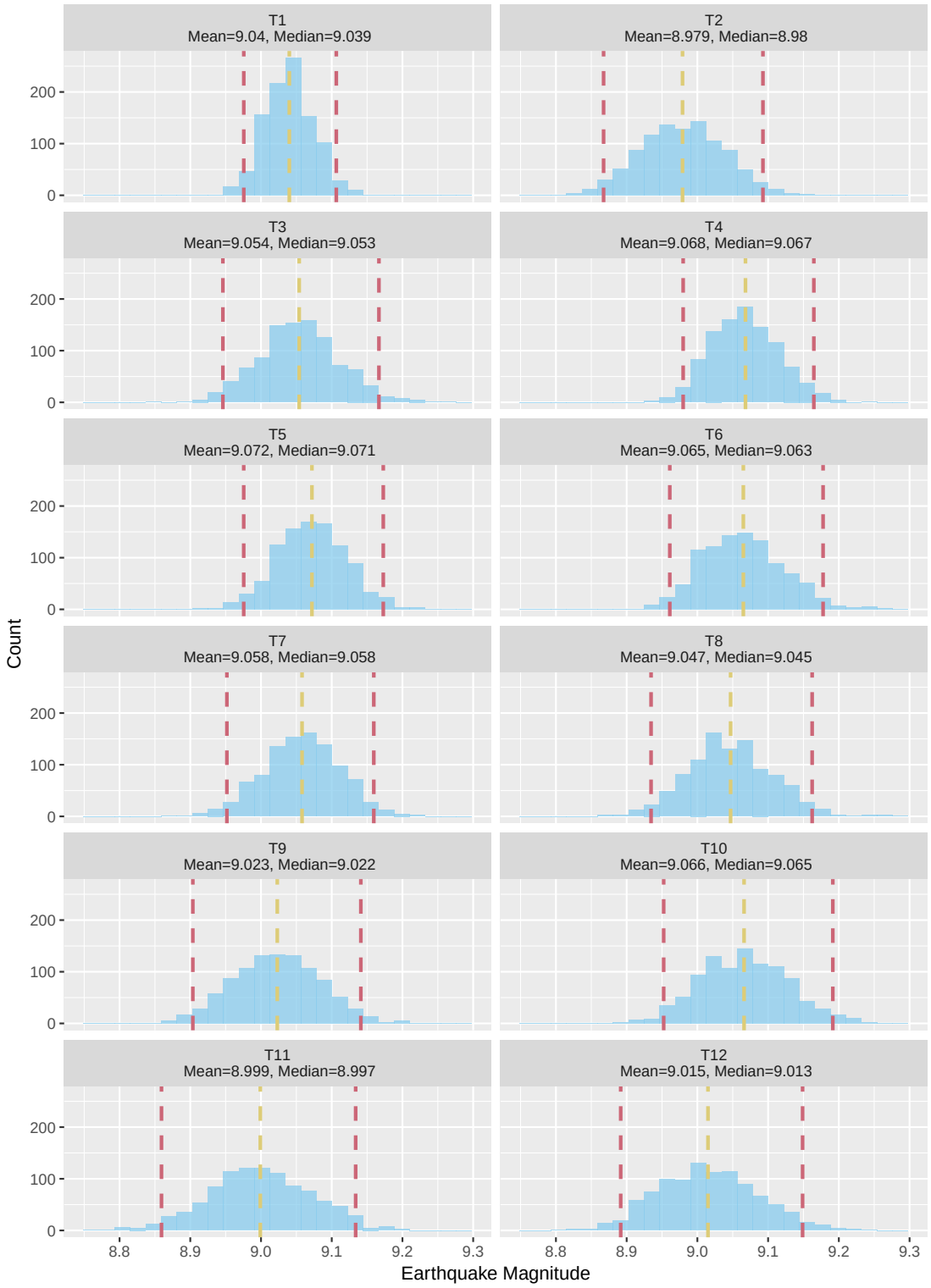

Figure 4.4.1: The empirical distributions of the magnitudes for all the megathrust events calculated from the slip realisations from the isotropic model without a shared spatial component. The red dashed lines give the lower 2.5% and upper 97.5% quantiles, and so the are in between these lines is the 95% empirical prediction interval for the event magnitude. The yellow dashed lines are the mean of the magnitudes for each event.

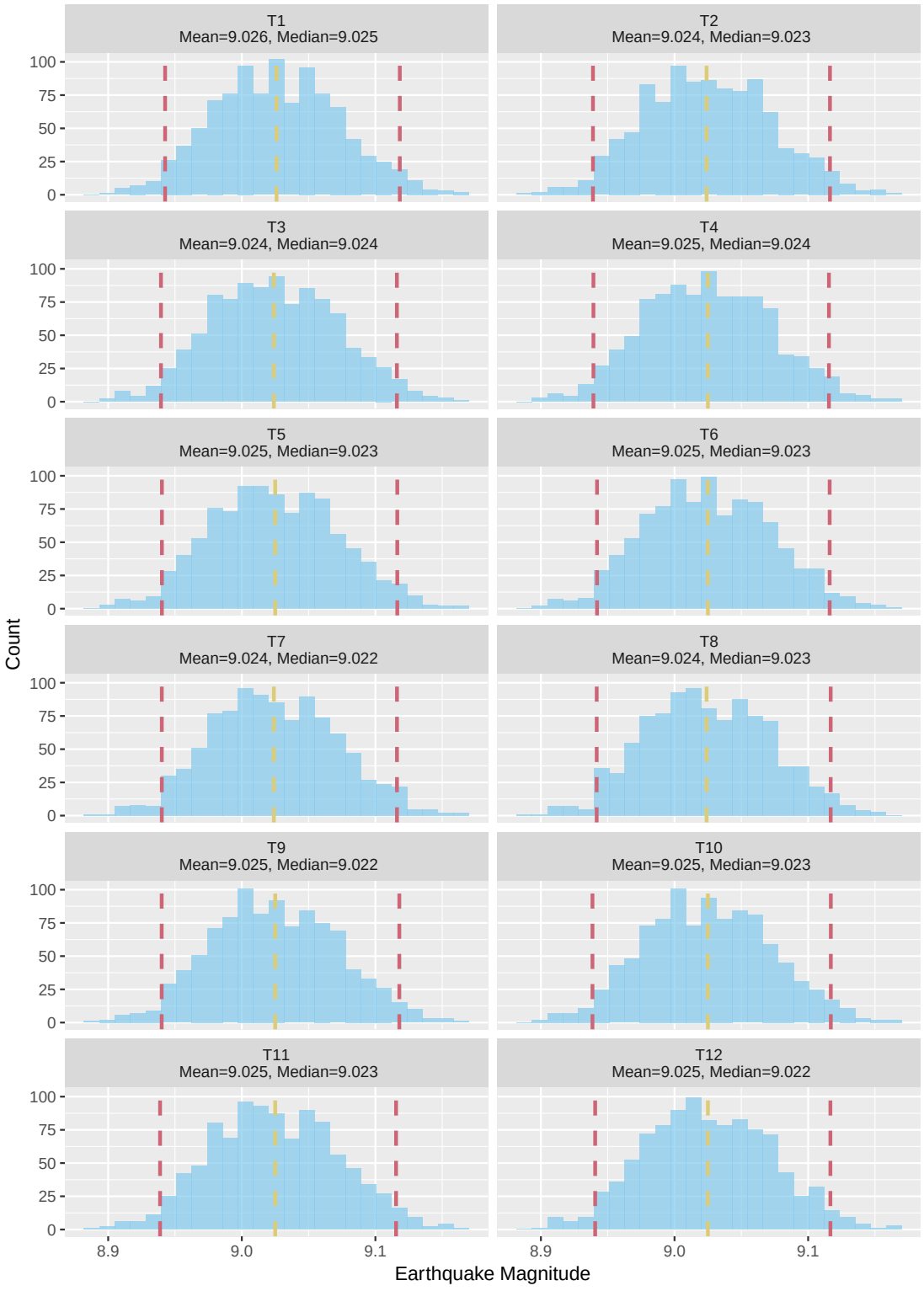

Figure 4.4.2: The empirical distributions of the magnitudes for all the megathrust events calculated from the slip realisations from the isotropic model with a shared spatial component. The red dashed lines give the lower 2.5% and upper 97.5% quantiles, and so the are in between these lines is the 95% empirical prediction interval for the event magnitude. The yellow dashed lines are the mean of the magnitudes for each event.

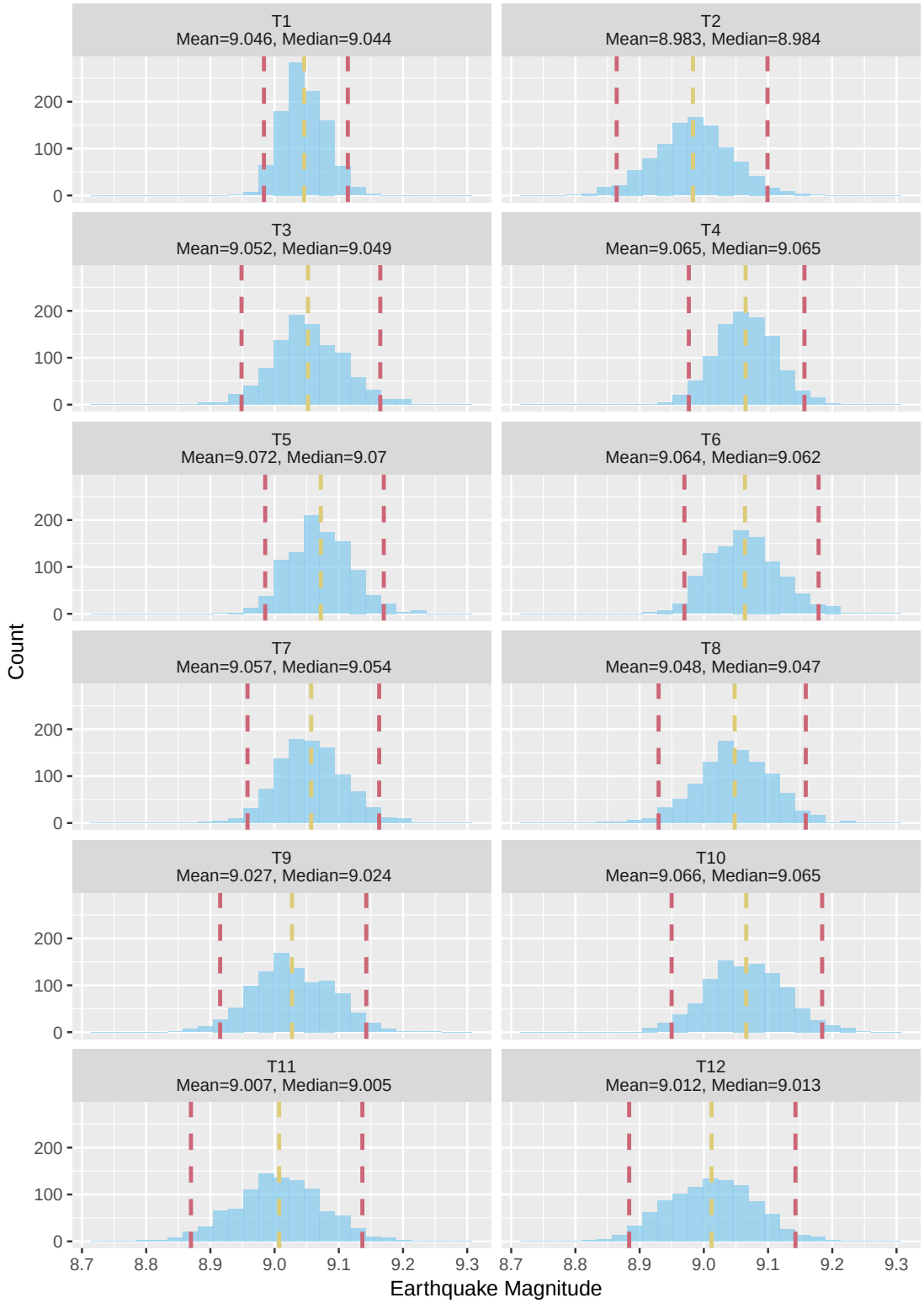

Figure 4.4.3: The empirical distributions of the magnitudes for all the megathrust events calculated from the slip realisations from the anisotropic model without a shared spatial component. The red dashed lines give the lower 2.5% and upper 97.5% quantiles, and so the are in between these lines is the 95% empirical prediction interval for the event magnitude. The yellow dashed lines are the mean of the magnitudes for each event.

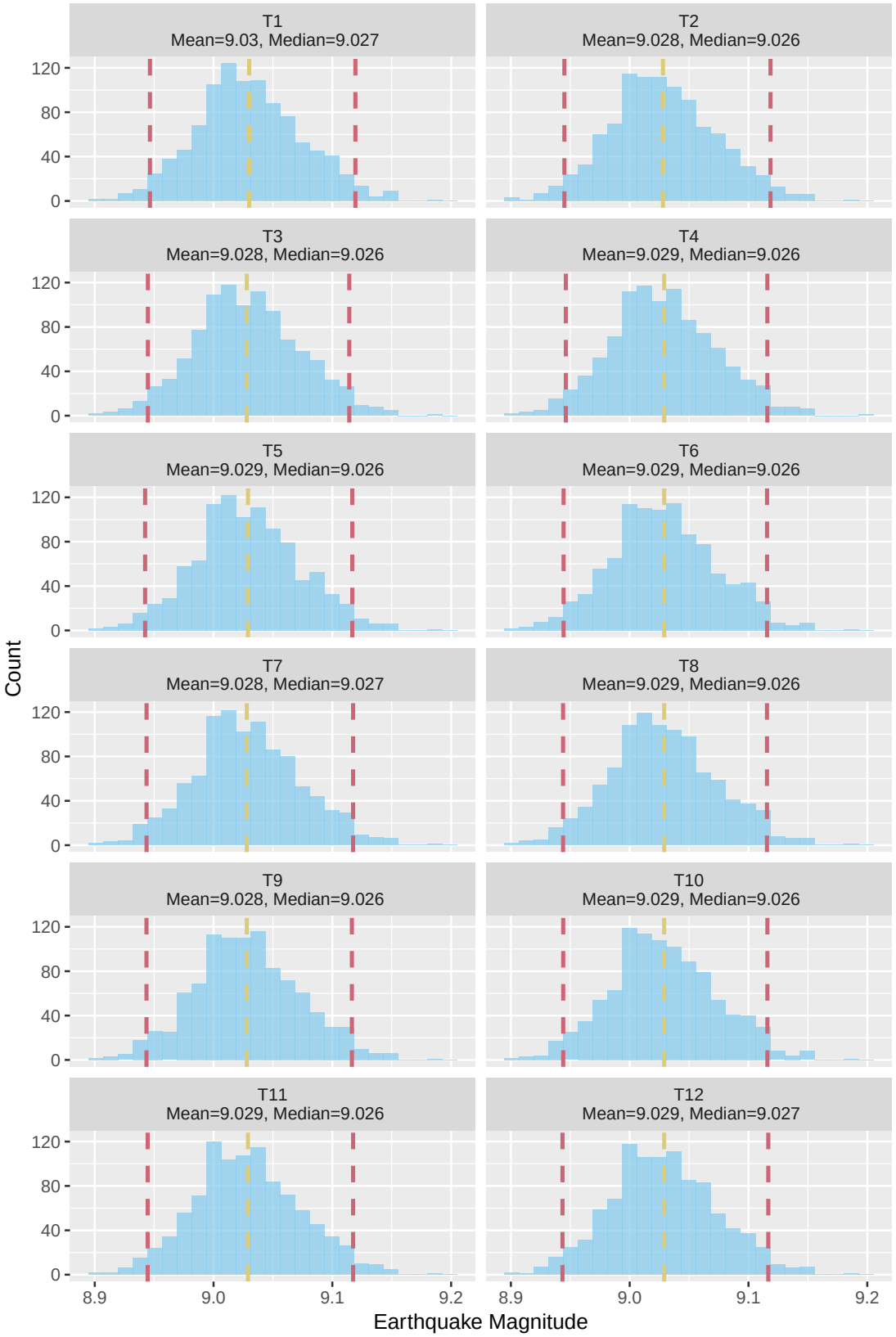

Figure 4.4.4: The empirical distributions of the magnitudes for all the megathrust events calculated from the slip realisations from the anisotropic model with a shared spatial component. The red dashed lines give the lower 2.5% and upper 97.5% quantiles, and so the are in between these lines is the 95% empirical prediction interval for the event magnitude. The yellow dashed lines are the mean of the magnitudes for each event.

CHAPTER

FIVE

PREDICTION OF A POTENTIAL FUTURE FULL FAULT RUPTURE

In this chapter the outcome of predicting a future megathrust event is explored for each model. Although a future full fault rupture may not occur, it is considered likely enough that predicting its properties is a worthwhile endeavour. Firstly the median parameters from the posterior distribution for each fully fitted model are used in predicting the resulting future coseismic slip distribution. Predictions are made many times for the coseismic slip distribution, and then these are used to predict the subsidence across the entire CSZ region. Finally the distribution of the magnitude resulting from the prediction of a future coseismic slip distribution is given for each model.

5.1 Potential Future Coseismic Slip Distribution for a Full Fault Rupture

To calculate a coseismic slip distribution one needs the parameters of the model and a draw from the underlying spatial fields. The chosen parameters are the median of the posterior distribution which are shown in the "Posterior Median" column of the tables in Section 4.1. The parameters which control the SPDE method are τ and κ and are used to calculate the precision matrices of the GMRF representations of the underlying spatial fields. These precision matrices are calculated via TMB in such a way as to be consistent with the optimisation process. Once a precision matrix has been calculated one can simulate from the underlying GMRF using the standard algorithm (that is Algorithm 2.3 from Rue and Held [74]). To make implementation easier, and likely much faster, these draws were taken by using INLA's [59] inbuilt *qsample* function. This draw from the underlying spatial distribution can then be combined with the selected parameters via the equations outlines in Section 3 to give a realisation from a future coseismic slip distribution. This is then repeated $n_{sims} = 1000$ times to give a good representation of the future coseismic slip distribution. As in the historical case, the mean and standard deviation is given for the coseismic slip distribution of each model. The mean can be seen in Figure 5.1.1 and the standard deviations in Figure 5.1.2. Both the models without a shared component display a uniform coseismic slip

distribution. They are essentially relying on the taper function to taper the slips on the down dip edge. This is expected since the random effects of these models when they predict a new megathurst event are not conditioned on any data, it is only the model parameters that have been informed by the data. On the other hand, the prediction of the future coseismic slip distribution for both the shared spatial component models used a shared random effect which is conditioned on the data. This results in a concentration of slip in the central latitudinal region. The largest concentration of slip is given by model 4. This occurs on the shallower, western edge of the fault region between $46°N$ and $47°N$. However this model also places slip values in the range of 10 m to 15 m near to coastal areas which is larger than previously given in work such as Goda [23] and Wang et al. [35]. In Goda [23], their simulation of a full fault rupture for a $M_w 9.0 - 9.1$ event indicates coseismic slip of up to 20 m, but with this concentration of slip all the way from $49°N$ to $44°N$. This is interesting, as our results indicate that the slip distribution is concentrated in smaller spatial region, but with higher values predicted. This probably comes from the fact that the largest subsidence estimates occur in the latitudinal region where these models gives the highest value of slip. The distribution of SD once again tracks the mean.

5.2 Predicting Future Subsidence Across the Whole Region

Now that 1000 realisations from the future slip distributions have been taken, they can be used to calculate 1000 subsidence realisation across the whole of the CSZ. The same Okada matrix is used here as was used in Section 4.3 and thus future subsidences will be predicted across the grid of points seen in Figure 4.3.3. From these, the mean and standard deviation of the subsidence predictions can be calculated. The mean that each model gives in illustrated in Figure 5.2.1 and the standard deviation of each model is shown in Figure B.2.3 in the Appendix.

As was inferred about the historical megathrust events, these potential future events have a band of uplift running alongside the western edge of the CSZ fault region. This demonstrates that in all modelling situations, it is highly likely that any future megathrust event would result in a tsunami. This agrees with research already done [75, 38].

5.3 Potential Future Megathrust Magnitude Distribution

The final quantity of interest that is presented for a future megathrust event is the distribution of the magnitude of the event predicted. The magnitude can be calculated for each of the slip realisations from the future slip distribution following (4.1) as before. The distribution of magnitudes is then presented in Figure 5.3.1 via a histogram for each model.

It is clear that all these models predict any future megathrust event to have a magnitude of $8.9 - 9.15$ which is a very large and potentially destructive event.

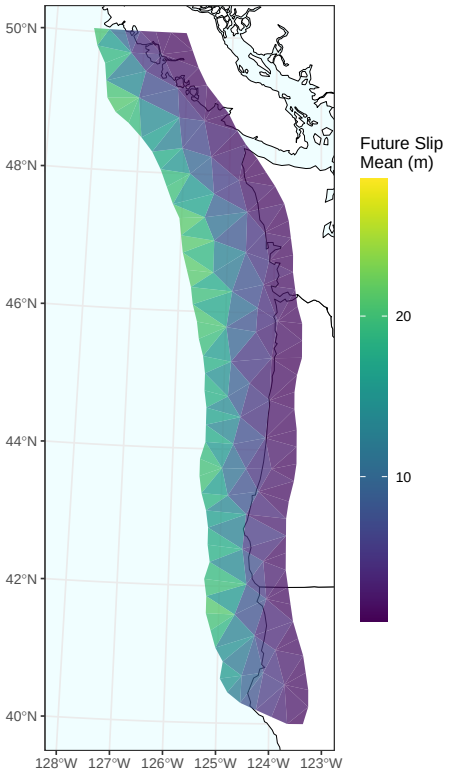

(a) Model 1

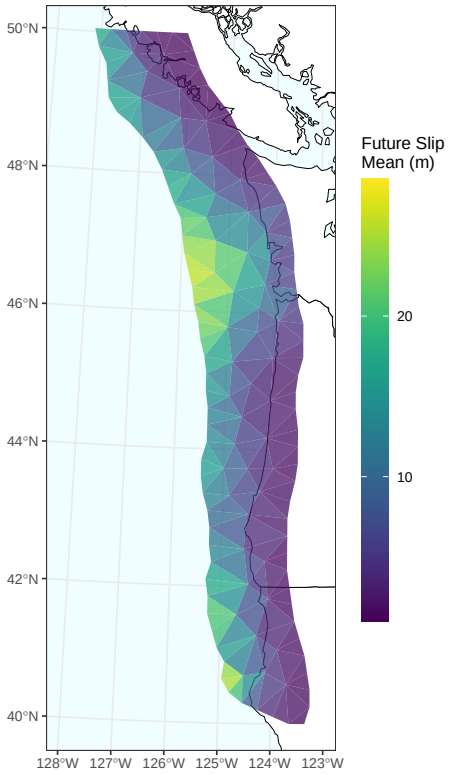

(b) Model 2

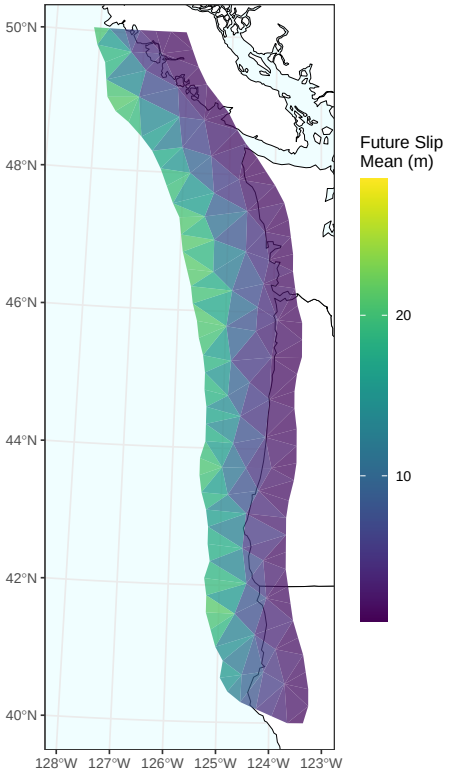

(c) Model 3

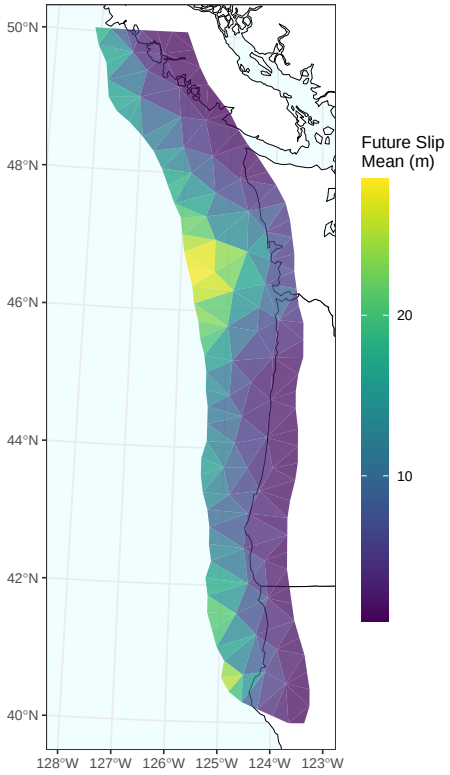

(d) Model 4

Figure 5.1.1: These plots show the mean of 1000 realisations of slip from the distribution given by the best fitted models.

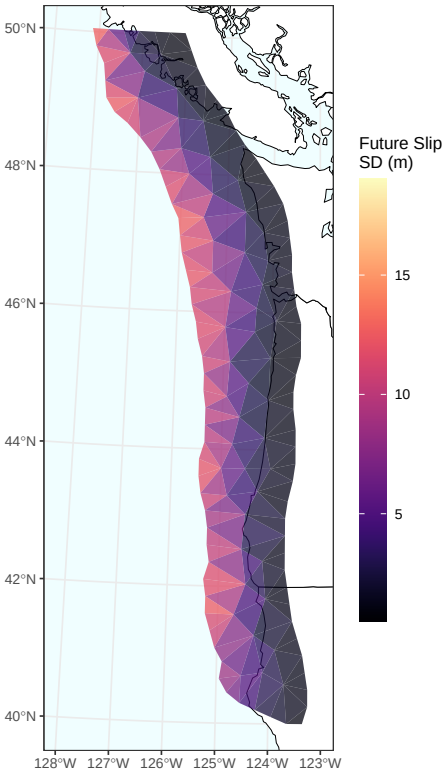

(a) Model 1

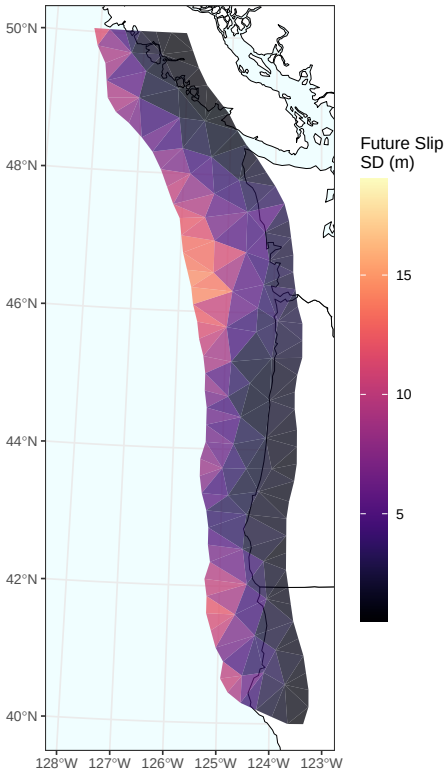

(b) Model 2

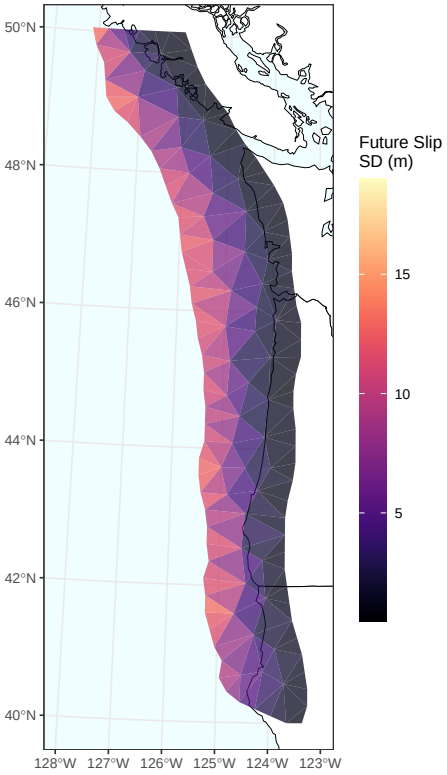

(c) Model 3

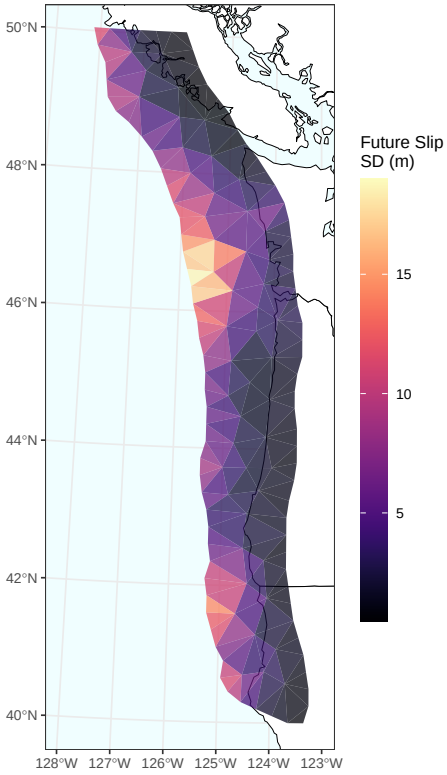

(d) Model 4

Figure 5.1.2: These plots show the standard deviation of 1000 realisations of slip from the distribution given by the best fitted models.

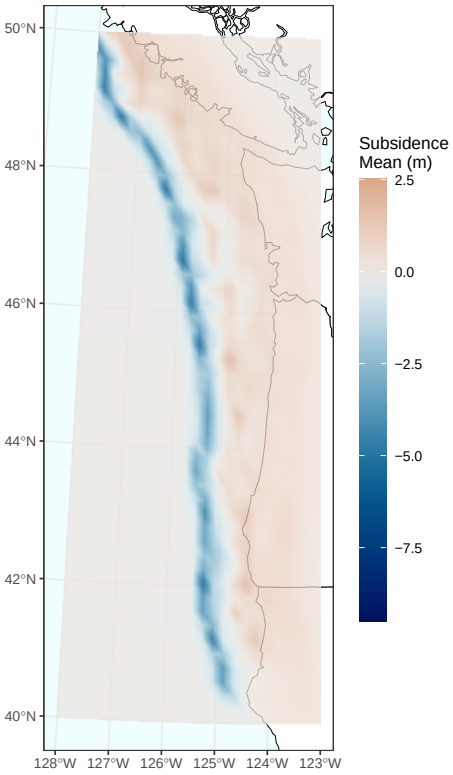

(a) Model 1

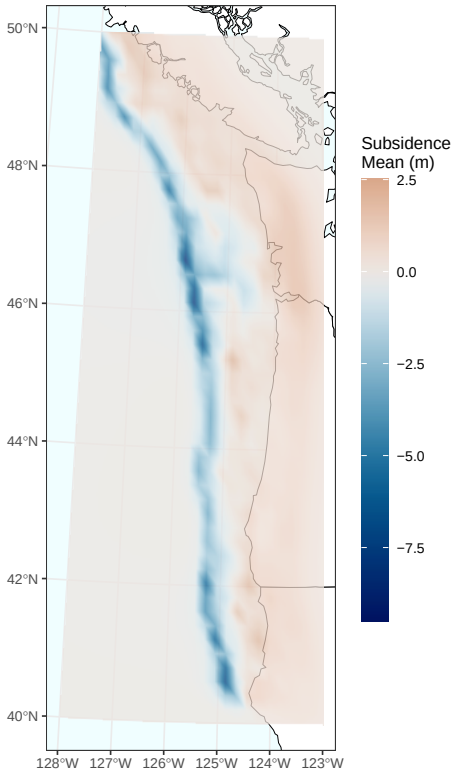

(b) Model 2

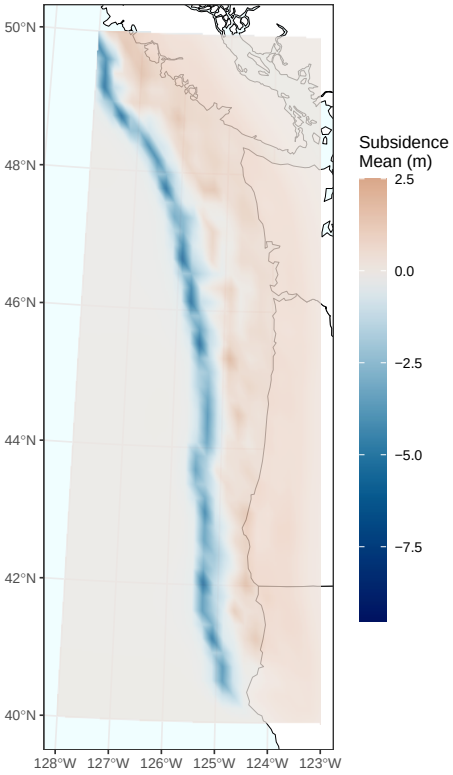

(c) Model 3

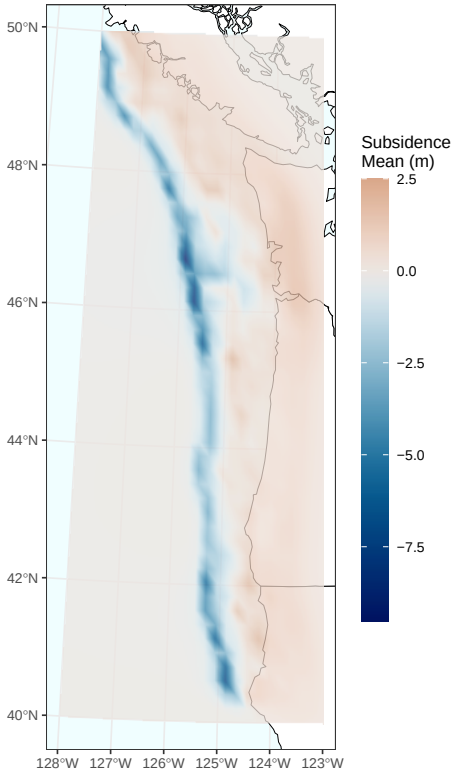

(d) Model 4

Figure 5.2.1: These plots show the mean of 1000 predictions of future subsidences across the entire CSZ for all the model.

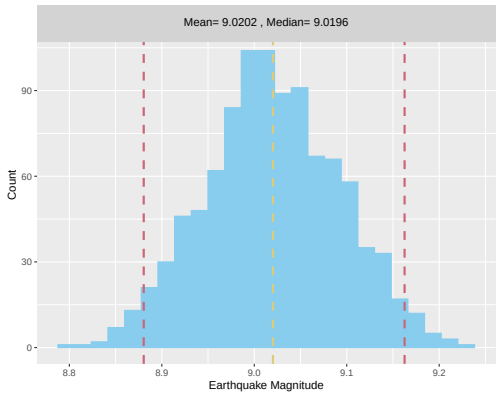

(a) Model 1

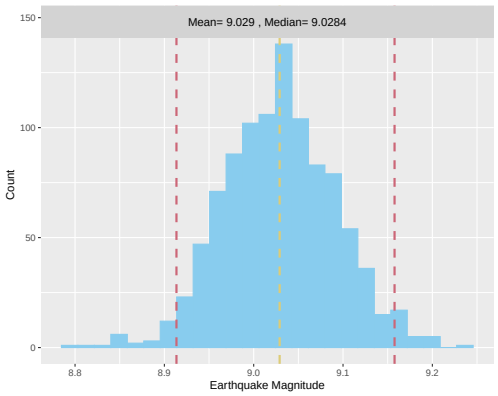

(b) Model 2

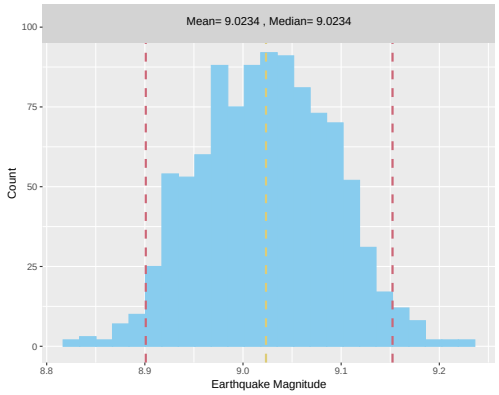

(c) Model 3

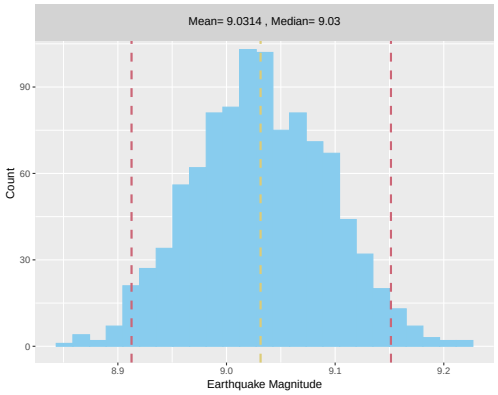

(d) Model 4

Figure 5.3.1: These figures show the distributions of magnitudes for predicted future megathrust event. The magnitudes were calculated from 1000 realisations of the slip distribution given by each model. The vertical red dashed lines give the lower 2.5% and upper 97.5% quantiles and thus the region in between them is the 95% confidence interval. The vertical yellow dashed line gives the mean of the distribution.

CHAPTER

SIX

MODEL VALIDATION

In this chapter the ability of the models to successfully determine the coseismic slip distribution of megathrust events is evaluated. The main modelling interest throughout this thesis is how well the information about future events can be captured and thus giving information about potential risk. Therefore a cross validation scheme, alongside appropriate scoring rules are used to explicitly reveal how well the different models can predict unseen megathrust events.

6.1 Details of the Validation Scheme

Here the validation scheme used is presented. This starts by assuming a score function s and as previously let the megathrust events be indexed $m \in (1, .., M)$. For each megathrust event there are N_m subsidence estimates which are given as $y_{i,m}$ for $i \in (1, ..., N_m)$. The exact numbers for N_m and the spatial distribution of estimates for each megathrust event was seen previously in Figure 2.2.3. A validation fold is then given by leaving out all of the subsidence estimates linked to one of the megathrust events from the data set thus leaving subsidence estimates for $M - 1$ megathrust event with which to fit the fold model. After fitting, this fold model can then be used to predict the left out subsidence estimates. This is done by drawing $n_{sims} = 1000$ realisations of the fixed parameters via the joint precision matrix of the fold model. In the case of the models with a shared spatial component, 1000 draws are also taken from this shared spatial component. Predicting the left out megathrust event is thought of as predicting a future unseen event, as discussed in Chapter 5. Note however that instead of choosing a "best" parameter set, the precision matrix method is used to generate 1000 draws of the fixed model parameters. This results in 1000 predictions for each of the left out subsidence estimates, which will be thought of as an empirical distribution for these estimates. The given score can then be calculated for each of the subsidence estimates given the predicted subsidence distribution. Mathematically this score is denoted as $s(y_{i,m}|P_{-m})$ whereby P_{-m} refers to the empirical distribution of predictions for the subsidence estimates when the model is fitted without $(-m)$ the estimated from megathrust event m. With the score for each of the subsidence estimates from the left out event, it is possible to calculate the average event score

e_m as:

$$e_m = \frac{1}{N_m} \sum_{i=1}^{N_m} s(y_{i,m}|P_{-m}). \tag{6.1}$$

Finally the total model score, e, can be calculated by taking the average over all the left out event scores:

$$e = \frac{1}{M} \sum_{m=1}^{M} e_M. \tag{6.2}$$

6.2 Scoring Rules Considered

Now that the validation scheme is in place, the next step is to choose the scores which will be used to evaluate the predictive ability of the model. To get a good overview of how well the models perform a selection of scores will be chosen. It is also useful to introduce proper scoring rules and strictly proper scoring rules here. A proper scoring rule is one whereby the expected score is minimised when the predictive distribution is equal to the distribution of the observations. A strictly proper scoring rule is one whereby the expected score is minimised ONLY when the predictive distribution is equal to the distribution of the observations. This means that a strictly proper score will be minimised only by the correct model, whereas a proper score can have other minimums. It is important to use proper and strictly proper scoring rules as it enables an honest assessment of how the predictive model is performing. One can read more about proper scoring rules in Gneiting and Raftery [76].

The selections of scores starts with the classical error scores of the Squared Error (SE) (6.3) and the Absolute Error (AE) (6.4). These scores are included to provide a more general overview of the models performance that can easily be interpreted by academics from a wide range of disciplines, thus potentially enabling the transfer of learning's to other studies. They are both also proper scoring rules. The squared error is more sensitive to outliers than the absolute error. With both these scores a lower value is considered better.

$$SE(y_{i,m}|P_{-m}) = (y_{i,m} - \hat{y}_{i,m})^2 \tag{6.3}$$

$$AE(y_{i,m}|P_{-m}) = |y_{i,m} - \hat{y}_{i,m}| \tag{6.4}$$

In addition the 95% prediction interval width will be reported which indicates the spread of predictions for one subsidence estimate. Alongside this the coverage at the 95% level will be reported. This is defined as the percentage of subsidence estimates which lie within the 95% empirical prediction interval. It is intuitively expected that this value is close to 95%. In general a smaller prediction interval width indicates that the model is more confident in it's prediction of subsidence. However this is not always a good thing, because if the validation gives a small prediction interval width, but also a small coverage percentage then this would suggest that the model is very confident in it's subsidence prediction when in fact the real estimate does not lie within the interval. To help resolve this the Interval Score (IS), a proper scoring rule, is used. The interval score set at a

$(1-\alpha)\cdot 100\%$ level, with a lower quantile for the subsidence predictions at l and an upper quantile at u is defined as:

$$IS(y_{i,j}|P_{-j}) = (u-l) + \frac{2}{\alpha}(l-y_{i,j})\mathbb{1}(y_{i,j}<l) + \frac{2}{\alpha}(y_{i,j}-u)\mathbb{1}(y_{i,j}>u). \quad (6.5)$$

Here, α is set to 0.05 which corresponds to a 95% empirical prediction interval (so l is the lower 2.5% quantile and u is the upper 97.5% quantile). Notice that the interval score is just the width of the prediction interval with a penalty term added when the actual subsidence estimate doesn't fall within the interval range. That way the score rewards smaller intervals but penalizes when the predictive interval doesn't cover the real value. Therefore a smaller interval score is better. Next, the Continuous Rank Probability Score (CRPS) is introduced. CRPS is used because it is strictly proper and can be evaluated when the predictive density is not of a known form, in this case when it is represented by draws from the posterior distribution. It is defined as:

$$CRPS(y_{i,m}|P_{-m}) = -\int_{\infty}^{\infty}(F_p(x) - \mathbb{1}(x \geq y_{i,m}))dx \quad (6.6)$$

where $F_p(x)$ is the cumulative distribution function for the distribution of subsidence predictions. With CRPS, a lower score indicates a better predictive model. The CRPS was implemented in this work using the *crps_sample* function from the *ScoringRules* R package [77]. Finally the time taken to optimise the full model plus the time taken to find the joint precision matrix for all the model parameters is recorded. This does not give information about the predictive ability of the model but rather gives an indication of the computational requirements to build the model and thus the model complexity. This gives 7 scores with which to judge the models by. CRPS will be favoured for deciding upon a best model, but considerations of the other scores and their attributes will also be accounted for.

6.3 Validation Results

This section gives the results of the validation process. Firstly it is insightful to see the actual subsidence prediction for each validation fold for each model. This will help explain the validation scores seen. These predictions are shown for the isotropic models in Figure 6.3.1, plotted with the actual estimates. The same for the anisotropic models can be seen in Figure 6.3.2.

There is no noticeable difference between the isotropic and anisotropic variants of the models. What is evident however is that the models with a shared spatial component predict much better on unseen subsidence data than the models without a shared component. This is because the shared component can be used when making predictions, whereas the models without this component rely solely on the fixed model parameters to give information about the subsidence data. Remembering that the shared component makes up the vast majority of marginal variance, these results are not surprising and one would expect these two models to predict unseen data with an accuracy comparable with the full model. To see how the performance of the models changes between the full and fold models for the CRPS score, please see Appendix B.3. It is seen that the models without a

shared component predict quite a flat subsidence distribution with latitude, and even predict some uplift in the southern extent of the CSZ. The next step is to look at information about the CRPS score for each model and each event. This is illustrated via boxplots in Figure 6.3.3. It is important to keep in mind how many subsidence estimates went into the CRPS distribution shown by each box, for example event $T12$ has only 2 subsidence estimates related to it. Similar boxplots of the other scores aggregated by event can be seen in Appendix B.4.

Figure 6.3.3 confirms that the models with a shared spatial component predict better than those without. This is shown by the boxes in the plot having a lower CRPS for models 2 and 4. Event $T12$ looks to be an anomaly in the results, but this event, as mentioned, has only 2 subsidence estimates attached to it, so inferring distributional results here is not really appropriate. Finally the total validation scores are calculated following (6.2) and presented in Table 6.3.1.

Score	**Model 1**	**Model 2**	**Model 3**	**Model 4**
MSE	0.683	0.186	0.665	0.166
MAE	0.571	0.297	0.560	0.295
95% PI Width	2.21	0.677	2.11	0.679
Coverage (%)	90.2	68.2	88.8	70.7
CRPS	0.276	0.204	0.275	0.204
Interval Score	0.0741	0.0686	0.0754	0.0681
Time (mins)	20.2	35.4	26.1	40.7

Table 6.3.1: The overall model validation scores.

The validation process shows that the models with a shared component perform better in all the scores than the models without a shared component. This is apart from the coverage %, whereby the shared component models are a long way under the expected 95% coverage. It is suggested that this comes from the fact that these models rely heavily on the shared component to give the prediction and thus there will not be much variation between the megathrust events which could result in a narrower PI width. What is interesting is that despite the poorer coverage, the interval score is still lower for the shared component models, suggesting a better prediction interval. There is only a very slight difference between the isotropic and anisotropic models, with the anisotropic models performing slightly, but not significantly better overall. This gives reason to believe that anisotropy is an important component in modelling for CSZ coseismic slip distributions but that the anisotropy implemented here could not capture the information well enough to make a big difference in model outcomes. The models with a shared component do however take almost double the amount of time to fit, which is indicative of their complexity. This comes from having to optimise a shared component across all the models, as well as having to account for individual spatial effects as well.

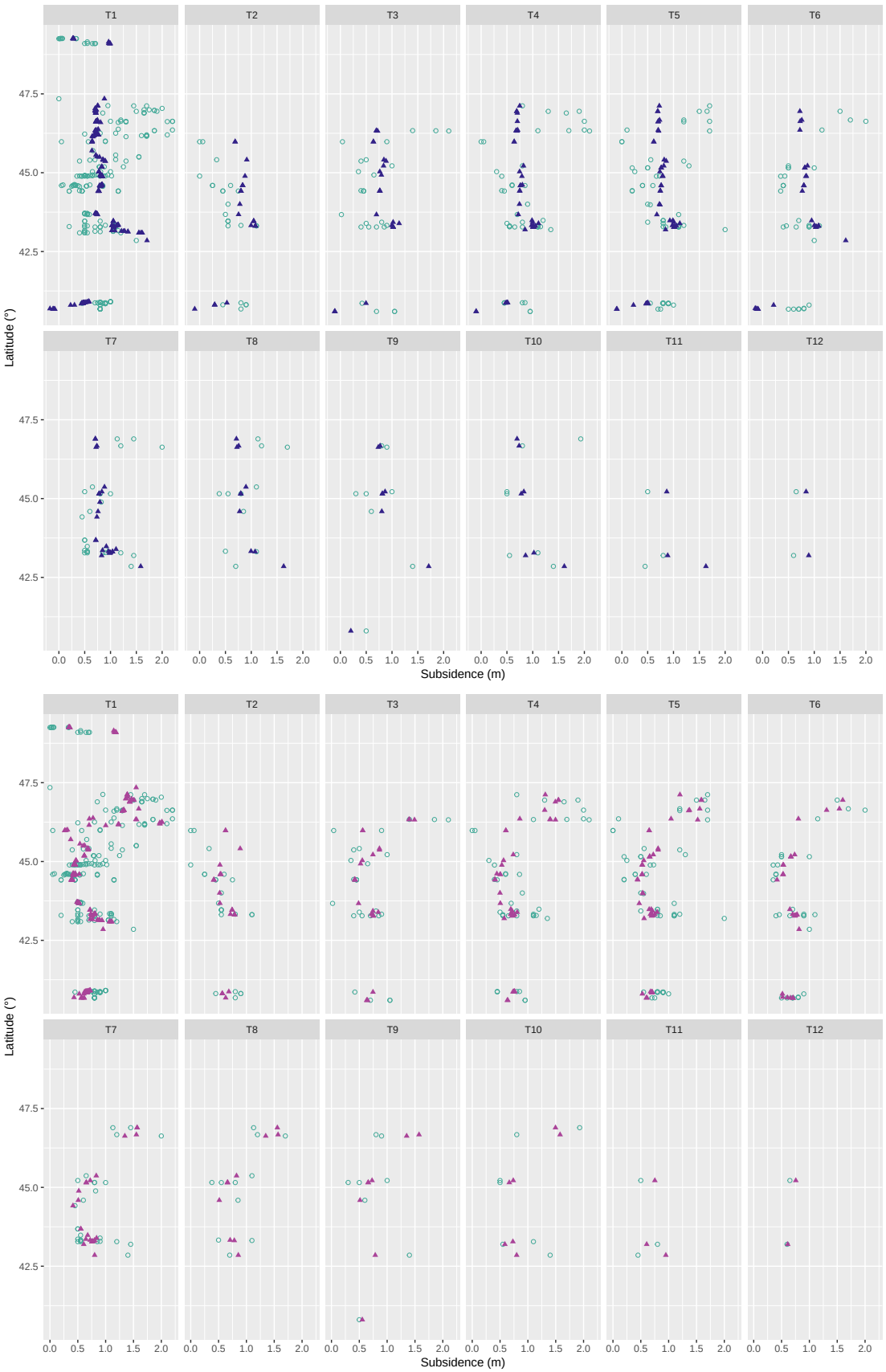

Figure 6.3.1: The above illustration relates to the first model, and below the second model. The illustration shows the mean subsidence prediction for each fold of the validation process plotted against latitude. The coloured triangles represent the predictions, whereas the hollow green points are the actual subsidence estimates.

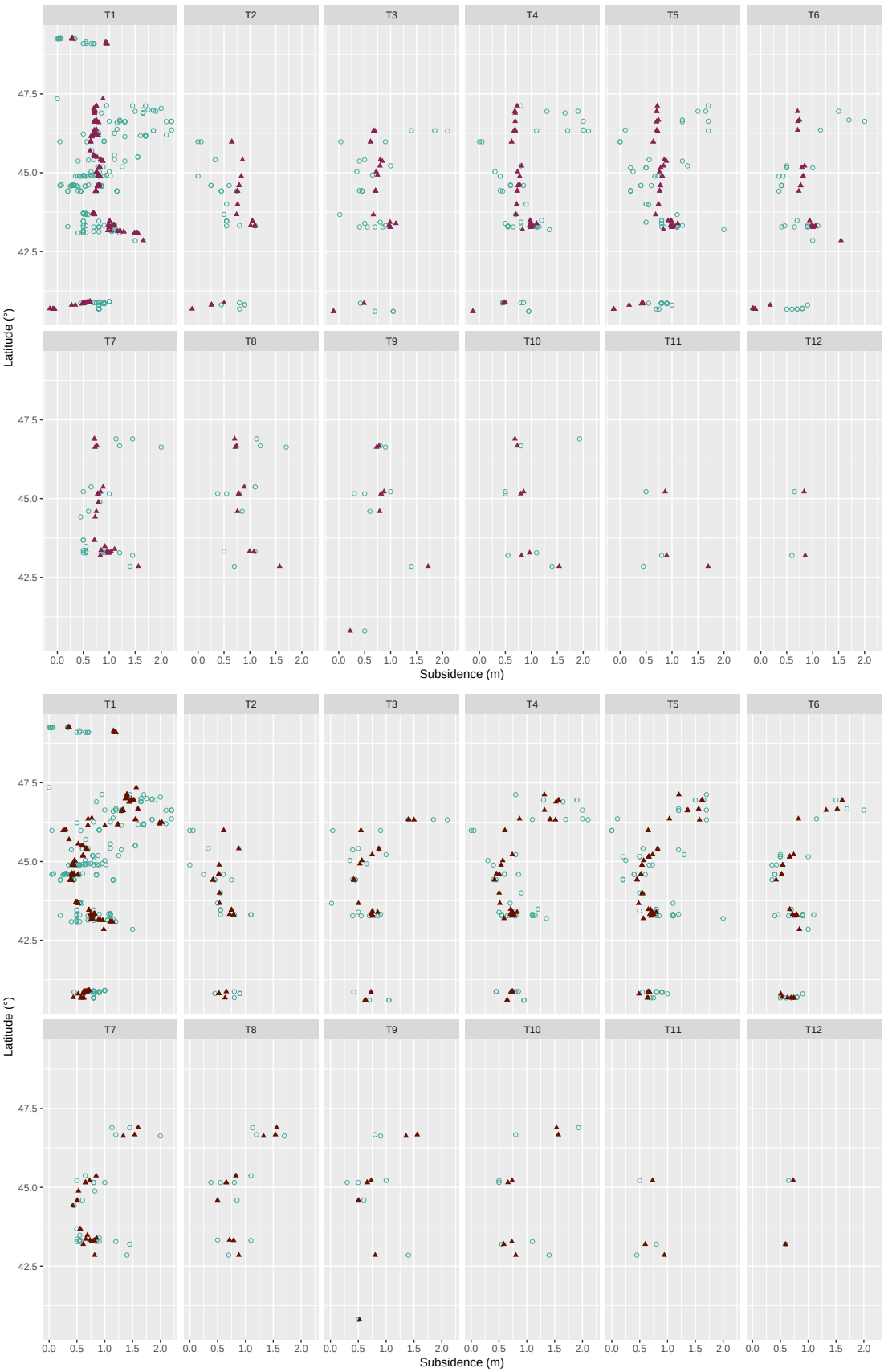

Figure 6.3.2: The above illustration relates to the third model, and below the fourth model. The illustration shows the mean subsidence prediction for each fold of the validation process plotted against latitude. The coloured triangles represent the predictions, whereas the hollow green points are the actual subsidence estimates.

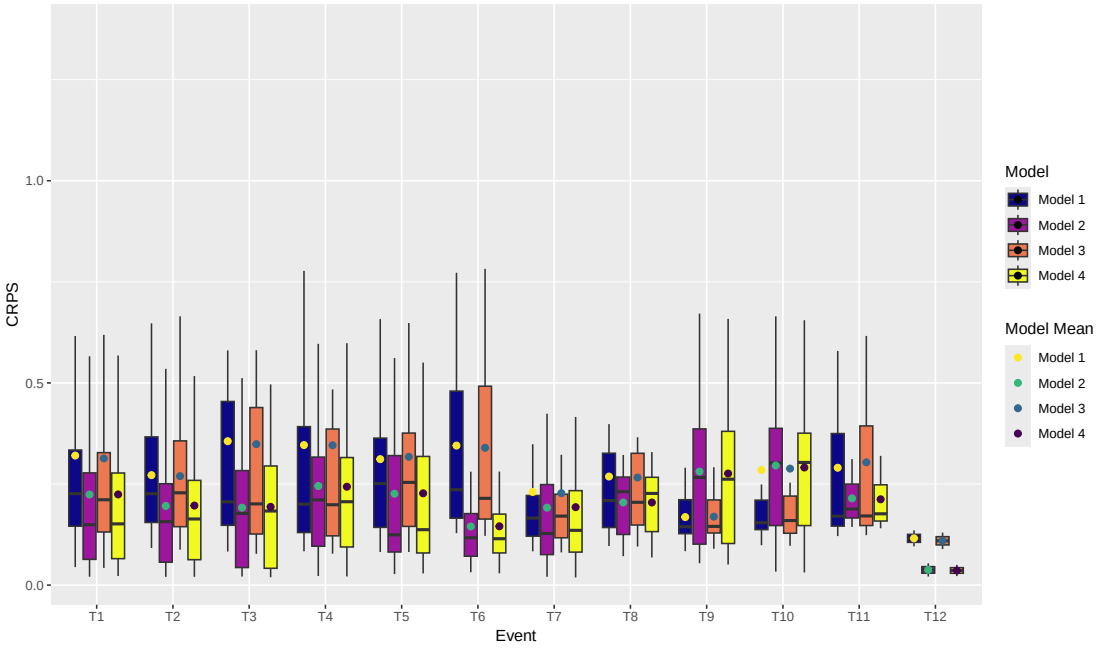

Figure 6.3.3: This illustrates the distribution of the CRPS from the validation process for each event. The distributions are split up by model and the mean is given as a point inline with the boxplot.

CHAPTER

SEVEN

CONCLUSIONS

In this final chapter, the work throughout this thesis is summarised. The outcomes of the modelling efforts are firstly highlighted. Then the shortcomings of these models are described, consequently leading to recommendations for any future research directions.

7.1 Model Outcomes

In Chapter 3, four new spatial to describe the CSZ coseismic slip were introduced. All of them have used a Bayesian hierarchy to link the coseismic subsidence data introduced in Chapter 2, to a resulting coseismic slip distribution. The first and second models are isotropic variants, with model 3 and model 4 introducing geometric anisotropy to help describe the rupture patterns seen in the strike and dip directions. Another important difference in the modelling is the introduction of a shared spatial component to model 2 and model 4. The validation in Chapter 6 leads to several conclusions regarding these models. Firstly the models with a shared component perform significantly better in megathrust subsidence prediction than the models without a shared spatial component. This is explained by the shared spatial component allowing for the transfer of information between megathrust events, and thus allowing for better prediction of unseen subsidence data. Secondly the models with an anisotropic component are shown to slightly, but not significantly outperform the isotropic models. This gives marginal evidence for the inclusion of anisotropy into the modelling but it is noted that the geometric, and fixed angle assumptions of the implemented anisotropy are too rigid to fully account for the underlying variations caused by the differing strike and dip angles. It is concluded that, out of the models presented here, model 4, that which incorporates a shared spatial component and geometric anisotropy is the one favoured for doing inference about historical megathrust event in the CSZ and when predicting potential future megathrust events.

The coseismic slip distributions which have been inferred and predicted from this modelling effort align with previous research in some respects but also differ slightly. The concentration of slip on the shallower edge of the CSZ is consistent with previous research [23, 35], and is mainly due to the effects of the taper functions, which is highlighted as incorporating key scientific information into

the modelling. The concentration of slip in the central latitudinal region of the CSZ, most evident in the inferred and predicted coseismic slip distributions of the shared spatial component models (Figure 4.2.1, Figure 4.2.2 and Figure 5.1.1), is also consistent with the simulated rupture patterns seen in Goda [23]. This result is most likely a direct consequence of inference from the subsidence estimates, which are highest in this region. Contrasting this is the extent to which the concentration of coseismic slip distribution is spread throughout region. In Goda [23], the maximum of mean slip was 20 m and spread over a relatively large central area of the CSZ, whereas we have seen the mean values of simulations reaching upwards of 30 m, but only in a relatively small region of the CSZ. Our results actually align with the preferred multi-modal coseismic slip distribution modelling described in Wang et al. [35]. Overall the Bayesian methodology presented seems to infer CSZ coseismic slip distributions which align with previous research, but currently the methodology given does not well enough account for key geological processes, mainly the strike-dip anisotropy.

7.2 Recommendations for Future Work

From the shortcomings mentioned, there are several logical next steps in any future research. Firstly some "easier" fixes. It would be ideal to incorporate the updated subsidence estimate data set of Kemp et al. [19] which would potentially involve personal correspondence to gain access to the summary statistics from their work. Since they used an improved Bayesian transfer function methodology in making their subsidence estimates, the associated uncertainties are smaller, which will further inform the models presented here and guide them to converge to a suitable coseismic slip distribution. Next would be to increase the resolution of both the subfault triangulation (seen in Figure 2.3.2) and the SPDE mesh (seen in Figure 3.2.1). Optimisation of models using high resolution meshes will take up a lot of RAM and computation time, however any results will closer approximate the reality of the CSZ. They will also help reduce uncertainty surrounding artifacts seen in the spatial plots, as discussed in Appendix B.2.

The next suggestions for future work are with regards to extensions to the models presented in this work. The Slab2 data set [25] is the first place to look. This dataset gives the point depths across the CSZ region, but it also gives an attached uncertainty with this measurement which has not been incorporated in this methodology. The depth is used explicitly in two places: the taper function 3.9 and the Okada model 3.1. There is potential to add some kind of error terms to both of these, but any modelling choices would have to be carefully considered and be grounded in both their physical interpretation and the theoretical implications involved. Another, and potentially better researched, area for model improvement would be to add in non-stationary anisotropy to the models. This would follows the work of Fuglstad et al. [65] and would mean that the underlying Random Fields could vary with the varying strike and dip angles as shown in Figure 3.5.1. There is also potential for different priors to be placed on the model parameters. It is advised to keep the prior on the taper function as this encodes a lot of scientific information about how cosesimic slip distributions tend to taper.

Alternatively the prior on the SPDE parameters could be investigated as both the τ and κ parameters seemed to be quite ill-defined during the optimisation process, leading to heavy tailed posterior distributions for these parameters. Making the conditions on the prior, especially in the shared component models, more constrictive would be a place to start. Alternatively one could investigate a completely new form of prior that is more appropriate to the CSZ. The final suggestion is to add an Auto-Regressive (AR) component into the modelling. This make intuitive sense since the megathrust events occur chronologically, and so could potentially exhibit a temporal component. One potential issue here is that partial margin ruptures can (and have [18]) happened which would disturb the temporal relation between full-fault ruptures.

7.3 Final Words

During this research, a new Bayesian methodology for inferring the coseismic slip distribution of past megathrust events has been developed, validated and criticised. It has resulted in an anisotropic model with a shared spatial component performing the best in CRPS when predicting unseen coseismic subsidence estimates. This indicates that it will also give the most accurate prediction of the coseismic slip distribution for a potential future megathrust event in the Cascadia region, and is the model which is advised to be developed further for usage in tsunami hazard modelling. The new methodology here has the potential to lead to greater accuracy in tsunami modelling and as such have the potential to inform the construction of safer infrastructure and most importantly warn communities in the Cascadia region of the risk that a future great earthquake poses.

REFERENCES

[1] Walter W Hays. *Facing geologic and hydrologic hazards: earth-science considerations*. 1240. US Department of the Interior, Geological Survey, 1981.

[2] International Monetary Fund. *Preliminary Assessment of the Macroeconomic Impact of The Tsunami Disaster on Affected Countries, and of Associated Financing Needs*. Accessed: 2024-05-26. 2005. URL: `https://www.imf.org/external/np/oth/2005/020405.htm`.

[3] Ahmed Ghobarah, Murat Saatcioglu, and Ioan Nistor. "The impact of the 26 December 2004 earthquake and tsunami on structures and infrastructure". In: *Engineering structures* 28.2 (2006), pp. 312–326.

[4] Mitsuaki Katayanagi et al. "Impact of the Great East Japan Earthquake on the employment status and mental health conditions of affected coastal communities". In: *International Journal of Environmental Research and Public Health* 17.21 (2020), p. 8130.

[5] Elisabeth Krausmann and Ana Maria Cruz. "Impact of the 11 March 2011, Great East Japan earthquake and tsunami on the chemical industry". In: *Natural hazards* 67 (2013), pp. 811–828.

[6] Okada Norio et al. "The 2011 eastern Japan great earthquake disaster: Overview and comments". In: *International Journal of Disaster Risk Science* 2 (2011), pp. 34–42.

[7] Yoshio Kajitani, Stephanie E Chang, and Hirokazu Tatano. "Economic impacts of the 2011 Tohoku-Oki earthquake and tsunami". In: *Earthquake Spectra* 29.1_suppl (2013), pp. 457–478.

[8] Takeo Ohnishi. "The disaster at Japan's Fukushima-Daiichi nuclear power plant after the March 11, 2011 earthquake and tsunami, and the resulting spread of radioisotope contamination". In: *Radiation research* 177.1 (2012), pp. 1–14.

[9] Oliver W Morgan et al. "Mass fatality management following the South Asian tsunami disaster: case studies in Thailand, Indonesia, and Sri Lanka". In: *PLoS medicine* 3.6 (2006), e195.

[10] Brian F Atwater and Eileen Hemphill-Haley. *Recurrence intervals for great earthquakes of the past 3,500 years at northeastern Willapa Bay, Washington*. 1576. US Government Printing Office, 1997.

[11] Harvey M Kelsey, Robert C Witter, and Eileen Hemphill-Haley. "Plate-boundary earthquakes and tsunamis of the past 5500 yr, Sixes River estuary, southern Oregon". In: *GSA Bulletin* 114.3 (2002), pp. 298–314.

[12] Harvey M Kelsey et al. "Tsunami history of an Oregon coastal lake reveals a 4600 yr record of great earthquakes on the Cascadia subduction zone". In: *Geological Society of America Bulletin* 117.7-8 (2005), pp. 1009–1032.

[13] Robert C Witter, Harvey M Kelsey, and Eileen Hemphill-Haley. "Great Cascadia earthquakes and tsunamis of the past 6700 years, Coquille River estuary, southern coastal Oregon". In: *Geological Society of America Bulletin* 115.10 (2003), pp. 1289–1306.

[14] Alan R Nelson, Harvey M Kelsey, and Robert C Witter. "Great earthquakes of variable magnitude at the Cascadia subduction zone". In: *Quaternary Research* 65.3 (2006), pp. 354–365.

[15] Chris Goldfinger et al. "Holocene earthquake records from the Cascadia subduction zone and northern San Andreas fault based on precise dating of offshore turbidites". In: *Annual Review of Earth and Planetary Sciences* 31.1 (2003), pp. 555–577.

[16] Chris Goldfinger et al. "Late Holocene rupture of the northern San Andreas fault and possible stress linkage to the Cascadia subduction zone". In: *Bulletin of the Seismological Society of America* 98.2 (2008), pp. 861–889.

[17] Brian F Atwater et al. *The orphan tsunami of 1700: Japanese clues to a parent earthquake in North America*. University of Washington Press, 2016.

[18] Lucinda J Leonard et al. "Rupture area and displacement of past Cascadia great earthquakes from coastal coseismic subsidence". In: *Bulletin* 122.11-12 (2010), pp. 2079–2096.

[19] Andrew C Kemp et al. "Revising estimates of spatially variable subsidence during the AD 1700 Cascadia earthquake using a Bayesian foraminiferal transfer function". In: *Bulletin of the Seismological Society of America* 108.2 (2018), pp. 654–673.

[20] Jason S Padgett et al. "Timing and amount of southern Cascadia earthquake subsidence over the past 1700 years at northern Humboldt Bay, California, USA". In: *Bulletin* 133.9-10 (2021), pp. 2137–2156.

[21] Maureen AL Walton et al. "Toward an integrative geological and geophysical view of Cascadia subduction zone earthquakes". In: *Annual Review of Earth and Planetary Sciences* 49 (2021), pp. 367–398.

[22] Randall J LeVeque et al. "Generating random earthquake events for probabilistic tsunami hazard assessment". In: *Global Tsunami Science: Past and Future, Volume I* (2017), pp. 3671–3692.

[23] Katsuichiro Goda. "Stochastic source modeling and tsunami simulations of Cascadia subduction earthquakes for Canadian Pacific coast". In: *Coastal Engineering Journal* 64.4 (2022), pp. 575–596.

[24] Clawpack Development Team. *Clawpack Version 5.9.2*. 2023. DOI: 10.5281/zenodo.10076317. URL: http://www.clawpack.org.

[25] Gavin P Hayes et al. “Slab2, a comprehensive subduction zone geometry model”. In: *Science* 362.6410 (2018), pp. 58–61.

[26] Gail M Atkinson and David M Boore. “Stochastic point-source modeling of ground motions in the Cascadia region”. In: *Seismological Research Letters* 68.1 (1997), pp. 74–85.

[27] Gail M Atkinson and Miguel Macias. “Predicted ground motions for great interface earthquakes in the Cascadia subduction zone”. In: *Bulletin of the Seismological Society of America* 99.3 (2009), pp. 1552–1578.

[28] Dane M Wiebe and Daniel T Cox. “Application of fragility curves to estimate building damage and economic loss at a community scale: a case study of Seaside, Oregon”. In: *Natural hazards* 71 (2014), pp. 2043–2061.

[29] Dawei Gao et al. “Defining megathrust tsunami source scenarios for northernmost Cascadia”. In: *Natural Hazards* 94 (2018), pp. 445–469.

[30] Katsuichiro Goda et al. “New scaling relationships of earthquake source parameters for stochastic tsunami simulation”. In: *Coastal Engineering Journal* 58.3 (2016), pp. 1650010–1.

[31] Geoffrey CP King and Steven G Wesnousky. “Scaling of fault parameters for continental strike-slip earthquakes”. In: *Bulletin of the Seismological Society of America* 97.6 (2007), pp. 1833–1840.

[32] Kelin Wang and Jiangheng He. “Effects of frictional behavior and geometry of subduction fault on coseismic seafloor deformation”. In: *Bulletin of the Seismological Society of America* 98.2 (2008), pp. 571–579.

[33] Diego Melgar et al. “Kinematic rupture scenarios and synthetic displacement data: An example application to the Cascadia subduction zone”. In: *Journal of Geophysical Research: Solid Earth* 121.9 (2016), pp. 6658–6674.

[34] Kelin Wang et al. “A revised dislocation model of interseismic deformation of the Cascadia subduction zone”. In: *Journal of Geophysical Research: Solid Earth* 108.B1 (2003).

[35] Pei-Ling Wang et al. “Heterogeneous rupture in the great Cascadia earthquake of 1700 inferred from coastal subsidence estimates”. In: *Journal of Geophysical Research: Solid Earth* 118.5 (2013), pp. 2460–2473.

[36] Yoshimitsu Okada. “Surface deformation due to shear and tensile faults in a half-space”. In: *Bulletin of the seismological society of America* 75.4 (1985), pp. 1135–1154.

[37] Eric L Geist and Tom Parsons. “Probabilistic analysis of tsunami hazards”. In: *Natural Hazards* 37 (2006), pp. 277–314.

[38] Hyoungsu Park, Daniel T Cox, and Andre R Barbosa. “Probabilistic Tsunami Hazard Assessment (PTHA) for resilience assessment of a coastal community”. In: *Natural Hazards* 94 (2018), pp. 1117–1139.

[39] United Nations. *Sustainable Development Goals*. Accessed: 2024-05-31. 2024. URL: `https://www.un.org/sustainabledevelopment/`.

[40] Garnier et al. *viridis(Lite) - Colorblind-Friendly Color Maps for R*. viridis package version 0.6.5. 2024. DOI: `10.5281/zenodo.4679423`. URL: `https://sjmgarnier.github.io/viridis/`.

[41] Thomas Lin Pedersen and Fabio Crameri. *scico: Colour Palettes Based on the Scientific Colour-Maps*. R package version 1.5.0. 2023. URL: https://cran.r-project.org/web/packages/scico/index.html.

[42] Jakub Nowosad. *rcartocolor: 'CARTOColors' Palettes*. R package version 2.0.0. 2023. URL: https://cran.r-project.org/package=rcartocolor.

[43] R Core Team. *R: A Language and Environment for Statistical Computing*. R Foundation for Statistical Computing. Vienna, Austria, 2024. URL: https://www.R-project.org/.

[44] RStudio Team. *RStudio: Integrated Development Environment for R*. RStudio, Inc. Boston, MA, 2024. URL: http://www.rstudio.com/.

[45] GADM. *Global Administrative Areas*. Accessed: [02/10/23]. Accessed 2023. URL: https://gadm.org/.

[46] Homeland Infrastructure Foundation-Level Data (HIFLD). *Canada and US Border Dataset*. Accessed: [02/10/23]. Accessed 2023. URL: https://hifld-geoplatform.opendata.arcgis.com/datasets/canada-and-us-border/explore.

[47] Andy Teucher and Kenton Russell. *rmapshaper: Client for 'mapshaper' for 'Geospatial' Operations*. R package version 0.5.0.9000, http://andyteucher.ca/rmapshaper/. 2023. URL: https://github.com/ateucher/rmapshaper.

[48] Hadley Wickham. *ggplot2: Elegant Graphics for Data Analysis*. Springer-Verlag New York, 2016. ISBN: 978-3-319-24277-4. URL: https://ggplot2.tidyverse.org.

[49] Chris Goldfinger et al. *Turbidite event history—Methods and implications for Holocene paleoseismicity of the Cascadia subduction zone*. Tech. rep. US Geological Survey, 2012.

[50] Christopher Bronk Ramsey. *OxCal (Version 4.0)*. Software. https://c14.arch.ox.ac.uk/oxcal/OxCal.html. 2001.

[51] AD Hawkes et al. "Late Holocene coseismic deformation at the Cascadia subduction zone, Oregon, USA". In: *AGU Fall Meeting Abstracts*. Vol. 2008. 2008, T53B–1937.

[52] Kamil Slowikowski. *ggrepel: Repulsive Text and Label Geoms for 'ggplot2'*. R package version 0.9.1. 2022. URL: https://ggrepel.slowkow.com/.

[53] U.S. Geological Survey. *ScienceBase Catalog*. Accessed: [02/10/23]. Accessed 2023. URL: https://www.sciencebase.gov/catalog/item/5aa312cde4b0b1c392ea3ef5.

[54] Paul Flück, RD Hyndman, and Kelin Wang. "Three-dimensional dislocation model for great earthquakes of the Cascadia subduction zone". In: *Journal of Geophysical Research: Solid Earth* 102.B9 (1997), pp. 20539–20550.

[55] Diego Melgar, Valerie J Sahakian, and Amanda M Thomas. "Deep coseismic slip in the Cascadia megathrust can be consistent with coastal subsidence". In: *Geophysical Research Letters* 49.3 (2022), e2021GL097404.

[56] Joël Gombin. *Concaveman: A very fast 2D concave hull algorithm*. R package version 1.1.0, https://joelgombin.github.io/concaveman/. 2024. URL: https://joelgombin.github.io/concaveman/.

[57] Robert J. Hijmans. *terra: Spatial Data Analysis*. R package version 1.7-76, https://rspatial.github.io/terra/. 2024. URL: https://rspatial.org/.

[58] Håvard Rue, Sara Martino, and Nicolas Chopin. "Approximate Bayesian inference for latent Gaussian models by using integrated nested Laplace approximations". In: *Journal of the Royal Statistical Society Series B: Statistical Methodology* 71.2 (2009), pp. 319–392.

[59] Håvard Rue, Sara Martino, and Nicolas Chopin. *R-INLA Project: Bayesian Analysis Using INLA*. Accessed: 2024-01-20. 2024. URL: https://www.r-inla.org/.

[60] Albrecht Gebhardt. *akima: Interpolation of Irregularly and Regularly Spaced Data*. R package version 0.6-3.4. 2024. URL: https://cran.r-project.org/web/packages/akima/index.html.

[61] Finn Lindgren, Håvard Rue, and Johan Lindström. "An explicit link between Gaussian fields and Gaussian Markov random fields: the stochastic partial differential equation approach". In: *Journal of the Royal Statistical Society Series B: Statistical Methodology* 73.4 (2011), pp. 423–498.

[62] Kasper Kristensen et al. "TMB: automatic differentiation and Laplace approximation". In: *arXiv preprint arXiv:1509.00660* (2015).

[63] Bertil Matérn. "Spatial Variation". In: *Meddelanden fran Statens Skogsforskningsinstitut* 49.5 (1960).

[64] Kerry Sieh. "The repetition of large-earthquake ruptures." In: *Proceedings of the National Academy of Sciences* 93.9 (1996), pp. 3764–3771.

[65] Geir-Arne Fuglstad et al. "Exploring a new class of non-stationary spatial Gaussian random fields with varying local anisotropy". In: *Statistica Sinica* (2015), pp. 115–133.

[66] Geir-Arne Fuglstad and Stefano Castruccio. "Compression of climate simulations with a nonstationary global SpatioTemporal SPDE model". In: *The Annals of Applied Statistics* 14.2 (2020), pp. 542–559.

[67] James T Thorson et al. "Geostatistical delta-generalized linear mixed models improve precision for estimated abundance indices for West Coast groundfishes". In: *ICES Journal of Marine Science* 72.5 (2015), pp. 1297–1310.

[68] Geir-Arne Fuglstad et al. "Constructing priors that penalize the complexity of Gaussian random fields". In: *Journal of the American Statistical Association* 114.525 (2019), pp. 445–452.

[69] Umut Altay. *GeoAdjust*. Accessed: 2024-05-31. 2024. URL: https://github.com/umut-altay/GeoAdjust/tree/main.

[70] Julie Røste. "The Importance of Mesh Resolution When Using the SPDE Approach". MA thesis. NTNU, 2020.

[71] Samuel H Clarke Jr and Gary A Carver. "Late Holocene tectonics and paleoseismicity, southern Cascadia subduction zone". In: *Science* 255.5041 (1992), pp. 188–192.

[72] U.S. Geological Survey. *Earthquake Magnitude, Energy Release, and Shaking Intensity*. Accessed: 2024-05-24. 2024. URL: https://www.usgs.gov/programs/earthquake-hazards/earthquake-magnitude-energy-release-and-shaking-intensity.

[73] Kenji Satake, Kelin Wang, and Brian F Atwater. "Fault slip and seismic moment of the 1700 Cascadia earthquake inferred from Japanese tsunami descriptions". In: *Journal of Geophysical Research: Solid Earth* 108.B11 (2003).

[74] Havard Rue and Leonhard Held. *Gaussian Markov random fields: theory and applications*. Chapman and Hall/CRC, 2005.

[75] Hyoungsu Park et al. "Probabilistic seismic and tsunami hazard analysis conditioned on a megathrust rupture of the Cascadia subduction zone". In: *Frontiers in built environment* 3 (2017), p. 32.

[76] Tilmann Gneiting and Adrian E Raftery. "Strictly proper scoring rules, prediction, and estimation". In: *Journal of the American statistical Association* 102.477 (2007), pp. 359–378.

[77] Alexander Jordan, Fabian Krüger, and Sebastian Lerch. "Evaluating Probabilistic Forecasts with scoringRules". In: *Journal of Statistical Software* 90.12 (2019), pp. 1–37. DOI: 10.18637/jss.v090.i12.

APPENDICES

APPENDIX

A

GITHUB REPOSITORY

All code used in this document are included in the Github repository linked below. Further explanations are given in the readme-file.

Github repository link

- `https://github.com/alastair-thomas/Cascadia`

APPENDIX

B

EXTENSIVE MODELLING RESULTS

B.1 Underlying GRF Illustrations

In this section the spatial random effects are shown for each model. The mean and standard deviation over the CSZ are given which are calculated from the $n_{sims} = 1000$ draws from the joint precision matrix for all the model parameters. In all the models the individual spatial fields (X) are shown for each mega thrust event, and then in the models which include a shared spatial field (W) these are also given. Firstly comes the isotropic model without a shared spatial component. The mean and standard deviation for the X spatial field for the first model can be seen in Figure B.1.1.

Next, the isotropic model with a shared component has two spatial random fields: X and W. The mean and standard deviation for the independent fields for all the mega thrust events can be seen in Figure B.1.2. The mean and standard deviation for the shared spatial field, W, can be seen in Figure B.1.3.

The mean and standard deviation for the X spatial field for the anisotropic model without a shared component can be seen in Figure B.1.4.

Much like its isotropic counterpart the anisotropic model with a shared spatial component also has two spatial random fields: the independent fields, X, and the shared spatial field W. The mean and standard deviation for the independent fields for all the mega thrust events can be seen in Figure B.1.5. Finally the mean and standard deviation for the shared spatial field in the fourth model can be seen in Figure B.1.6.

All of the models display the expected pattern for a GRF: the uncertainty is lowest around the data locations. This is perhaps most evident from the X fields in the non-shared component models. Since the shared spatial component is responsible for the vast majority of the marginal variance in model two and four, the mean of the random effect draws is only significantly different from 0 in the shared fields, X is essentially 0 over the entire region, and only visible in the plots because they do not share the same colour scale as the W fields. Additionally the W fields display lowest variance at data locations, whereas this pattern is not seen from the individual random effects fields in the shared component models.

B.2 Standard Deviation of Whole Region Subsidence Predictions

In this section the standard deviation of subsidence predictions across the entire CSZ region is shown for all the applied models. This is shown for isotropic models in Figure B.2.1, for anisotropic models in Figure B.2.2 and for future megathrust events in Figure B.2.3. This standard deviation is calculated from 1000 draws of the CSZ coseismic slip distribution. The Okada model was then used to predict the surface subsidence at a grid of points, shown in Figure 4.3.3, for all the slip draws. The SD was found from the 1000 subsidence predictions, and plotted via interpolation. The reason this is in the appendix and not the main text is because the plot looks "patchy" and it is unclear whether these are actual features of the predicted subsidence or come from the implementation. The features could come from the interpolation between points however the actual value at each point has been checked and these would indicate that this is an actual feature of the model and not the implementation. The choice of the Magma colour scale here was also not ideal as the plot becomes mainly black and unreadable. To try reduce this plotting affect the opacity was also scaled by the standard deviation which slightly helps.

B.3 Full vs Validation Model Scores

In this section the difference in the distribution of CRPS for subsidence predictions across each mega thrust event is explored. This comparison is made between when the full model is used to predict an event (a model fitted to the data for that event) and when the validation model is used to predict the subsidence in the left out event (a model which hasn't been fitted to the data from the event). The CRPS distribution for each event is shown as a boxplot, which is coloured by whether the CRPS is from the full model, or validation model. This information is shown for the isotropic models in Figure B.3.1 and for the anisotropic models in Figure B.3.2.

As is expected the full model performs better in all models, as shown by having a lower CRPS in the majority of cases. The distribution of CRPS for each event is also narrower for the full model indicating that they predict better a higher percentage of the time. These results are not groundbreaking work: if the model has been given access to data it has seen then it is much more likely to predict better. This just confirms that the modelling does in fact work. It is interesting to see that the models with a shared spatial component managed to be almost as good without access to the data being predicted as in the full model case. This again demonstrates a that these models have been able to use the data from other megathrust events effectively in predicting unseen megathrust events.

B.4 Score Distribution by Mega Thrust Event

This final appendix shows the distribution of model scores for each megathrust event. The CRPS was shown already in the main text as this score is highlighted as the one which is used for determining the "best" model. The absolute errors are

seen in Figure B.4.1, the squared errors are seen in Figure B.4.2 and the interval scores are seen in Figure B.4.3.

The absolute error confirms that the models with a spatial component predict the unseen subsidence better than those without a shared component. The squared error also confirms this, as well as highlighting some outliers in prediction for events $T10$ and $T11$. This will come from the simulation of the underlying spatial field via draws from the fixed parameters. Finally is the interval score which highlights some problems with the shared spatial component models. For most events, the interval score is low and tightly distributed which indicates a small PI, and good coverage of predictions. However for some events such as $T2$, $T8$ and $T9$ the interval score has a very wide distribution. Since it is know that the PI is always relatively narrow for these models, this shows that the actual observed subsidences lie outside the PI which is not what is wanted.

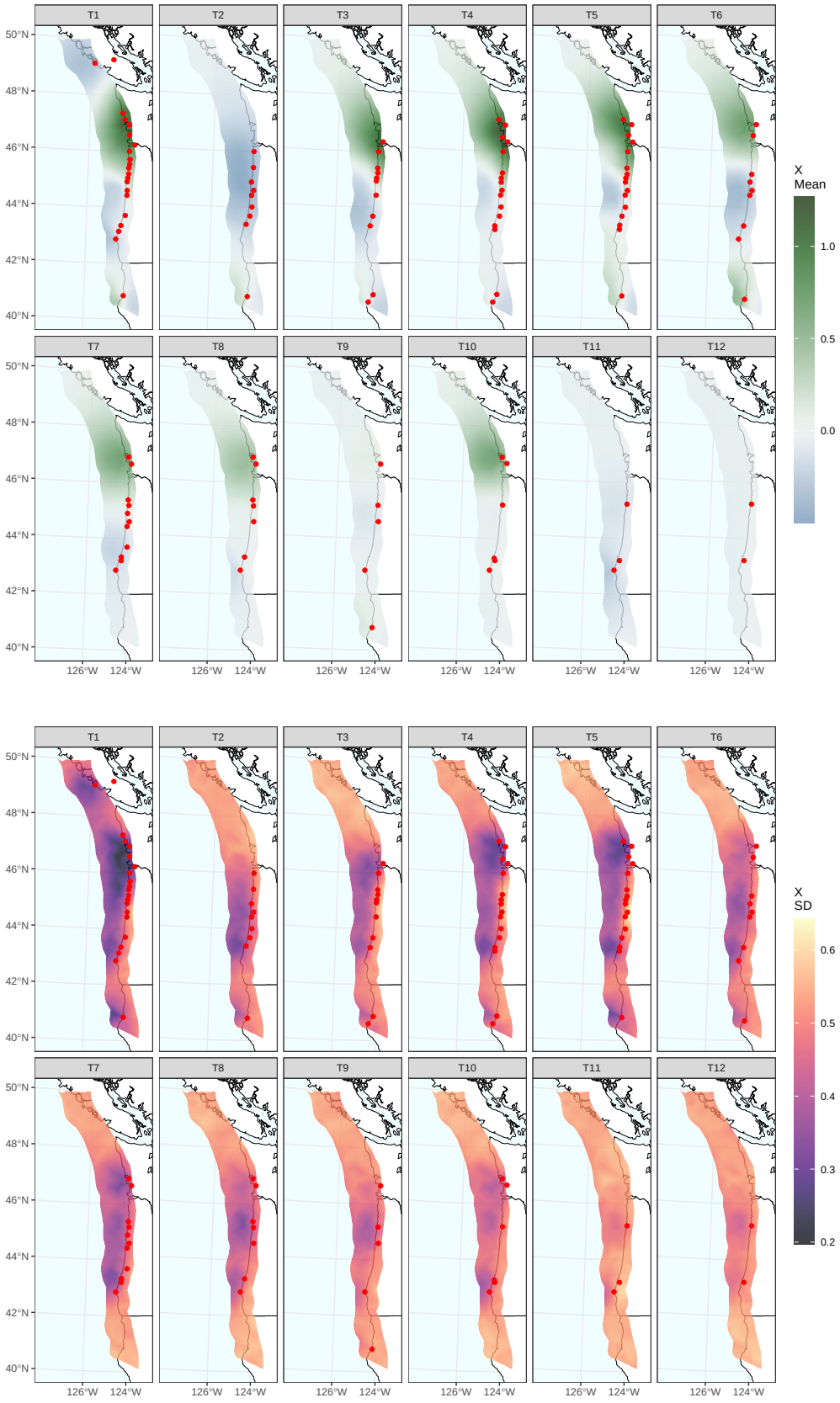

Figure B.1.1: The mean and standard deviation of X for the isotropic model without a shared component. The mean and standard deviation at the nodes in the SPDE mesh are interpolated onto the CSZ using linear interpolation. The red points are locations of observed subsidence estimates.

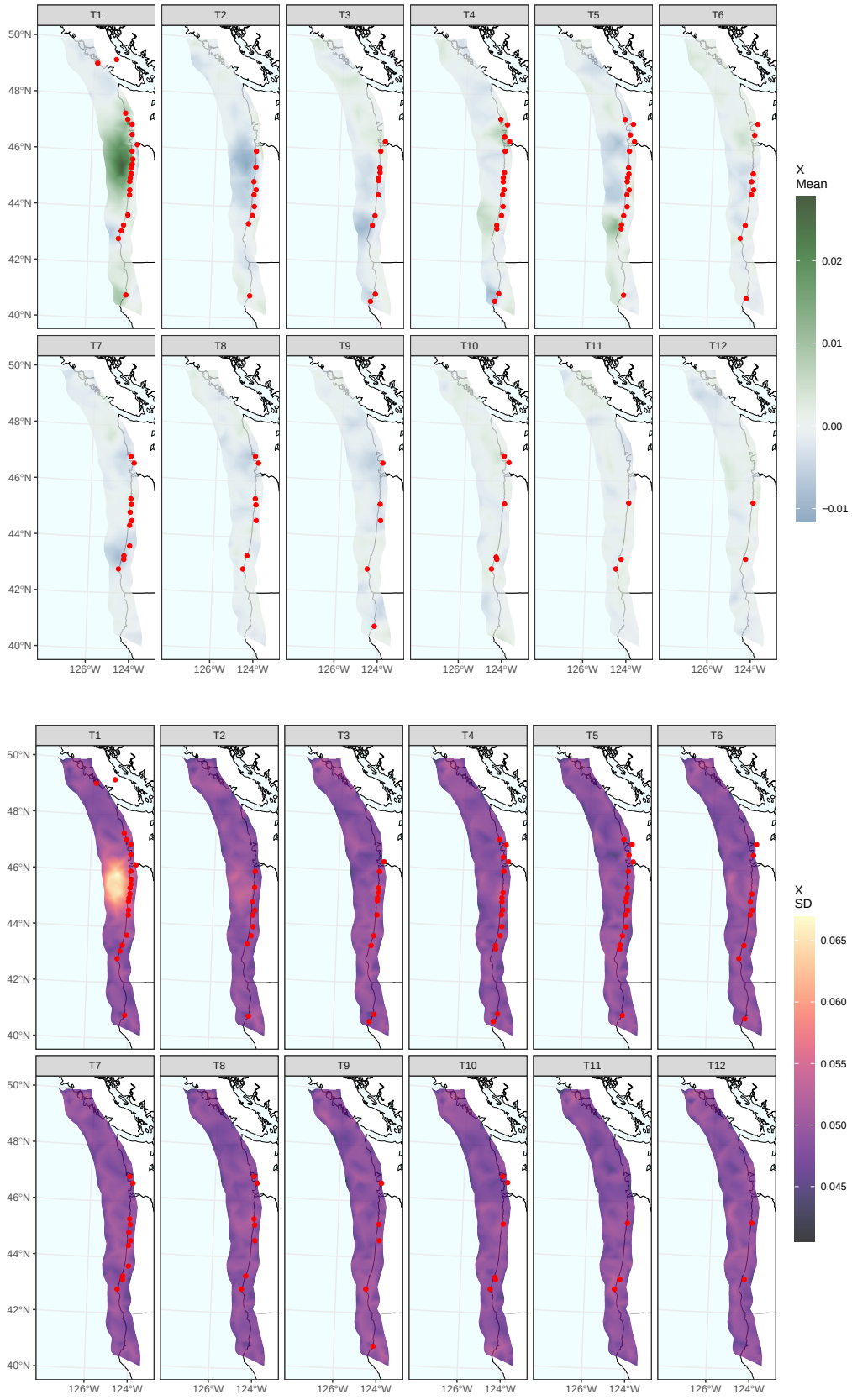

Figure B.1.2: The mean and standard deviation of X for the isotropic model with a shared component. The mean and standard deviation at the nodes in the SPDE mesh are interpolated onto the CSZ using linear interpolation. The red points are locations of observed subsidence estimates.

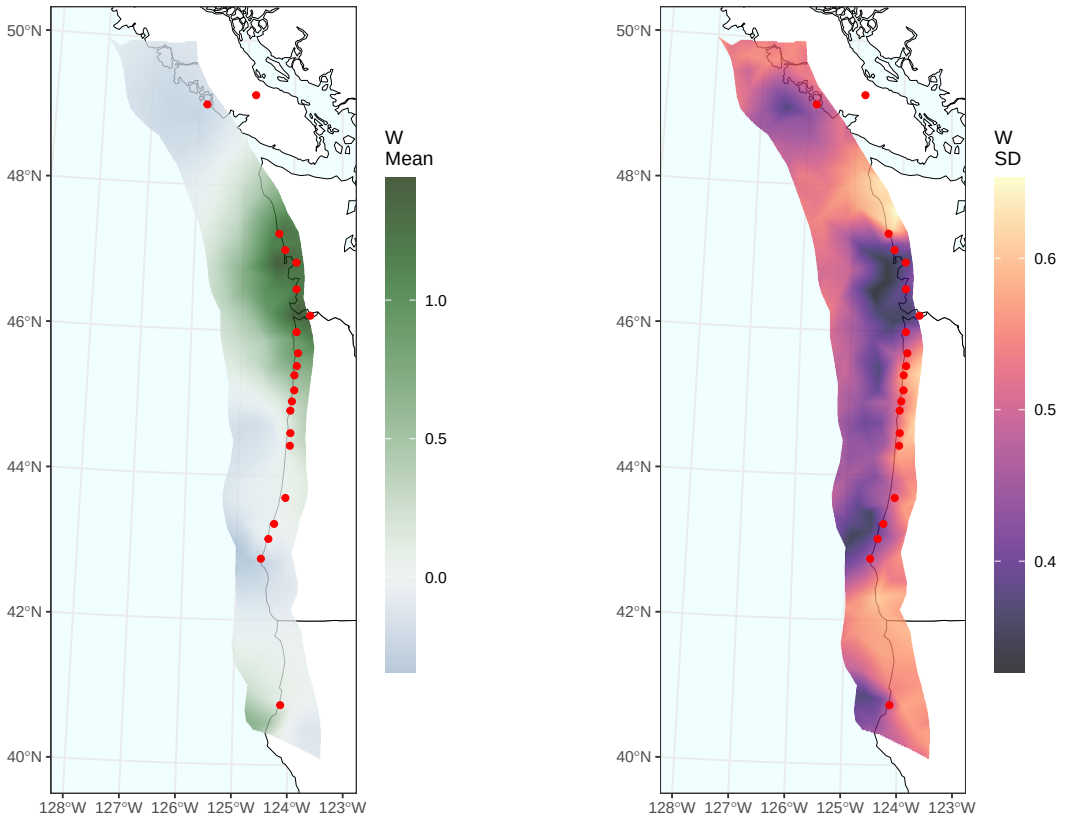

Figure B.1.3: The mean and standard deviation of W for the isotropic model with a shared component. The mean and standard deviation at the nodes in the SPDE mesh are interpolated onto the CSZ using linear interpolation. The red points are locations of observed subsidence estimates.

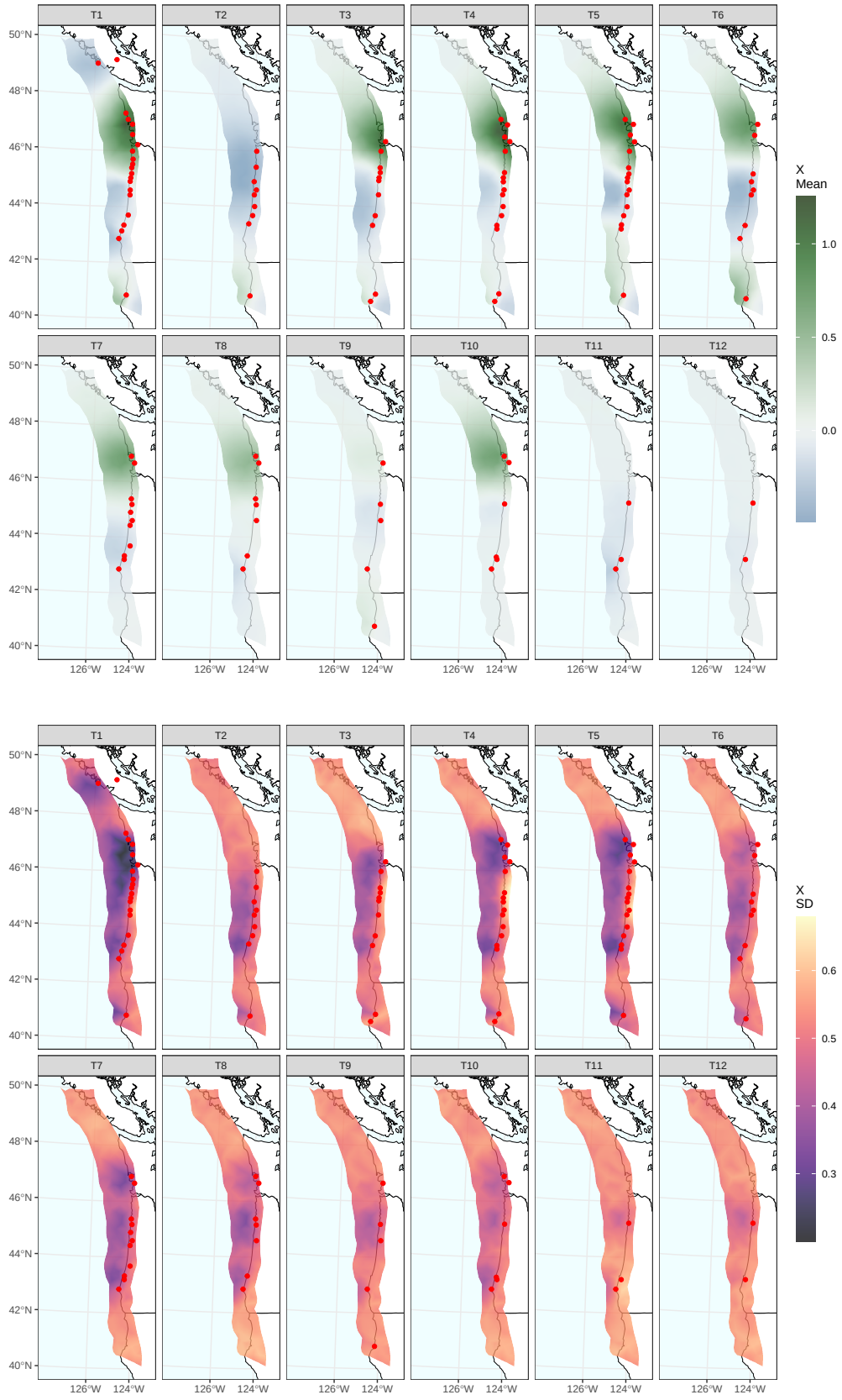

Figure B.1.4: The mean and standard deviation of X for the anisotropic model without a shared component. The mean and standard deviation at the nodes in the SPDE mesh are interpolated onto the CSZ using linear interpolation. The red points are locations of observed subsidence estimates.

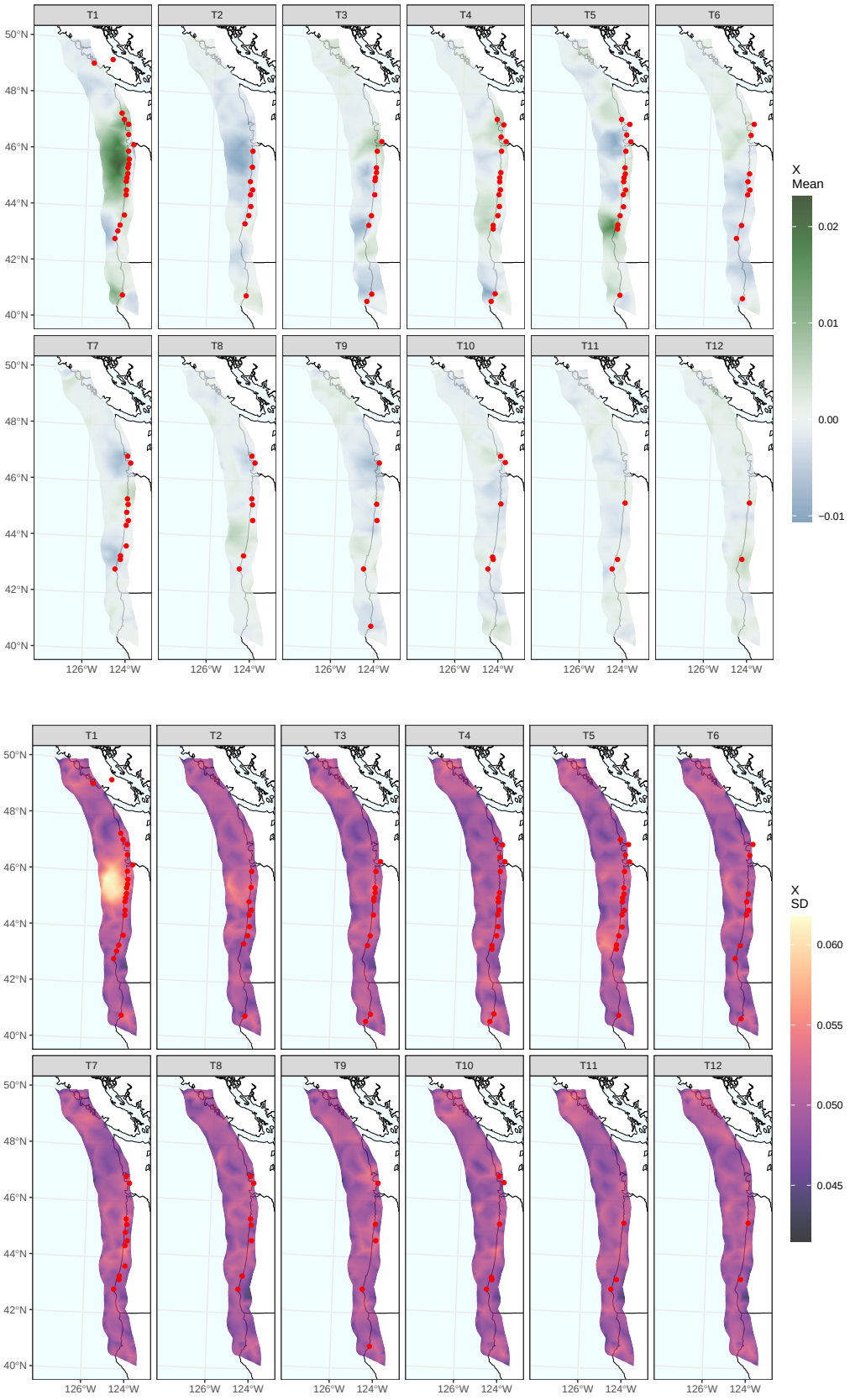

Figure B.1.5: The mean and standard deviation of X for the anisotropic model with a shared component. The mean and standard deviation at the nodes in the SPDE mesh are interpolated onto the CSZ using linear interpolation. The red points are locations of observed subsidence estimates.

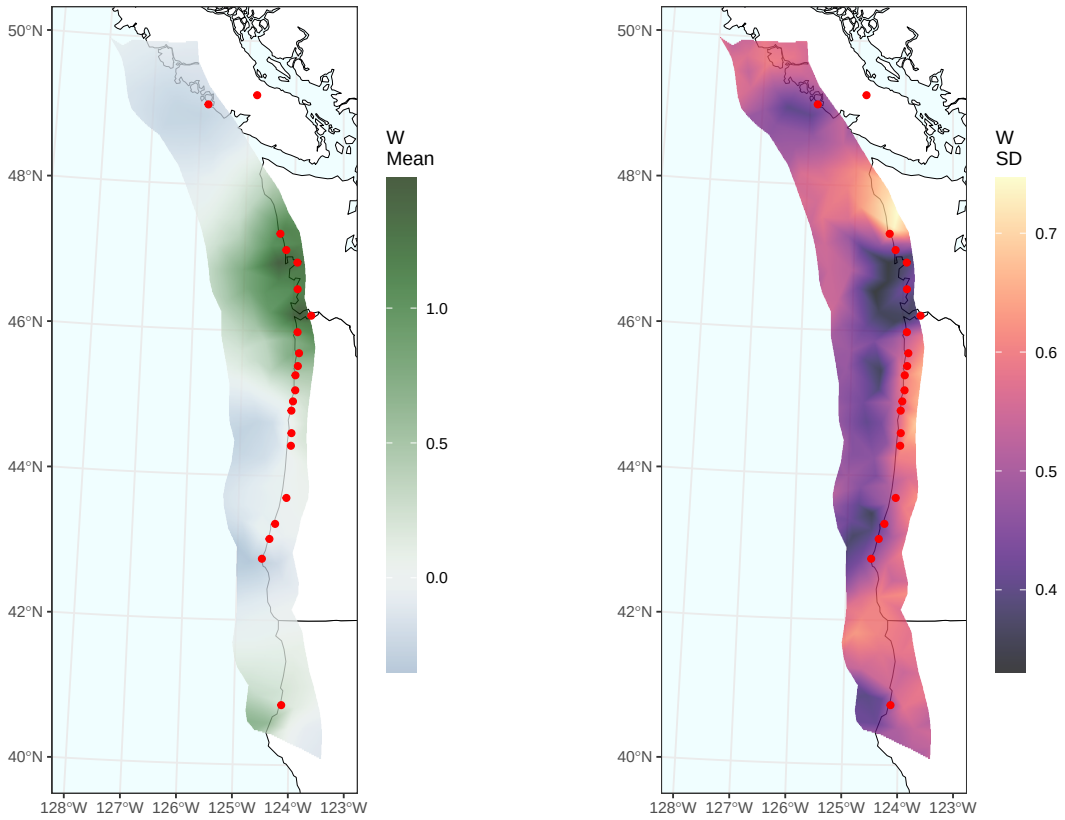

Figure B.1.6: The mean and standard deviation of W for the anisotropic model with a shared component. The mean and standard deviation at the nodes in the SPDE mesh are interpolated onto the CSZ using linear interpolation. The red points are locations of observed subsidence estimates.

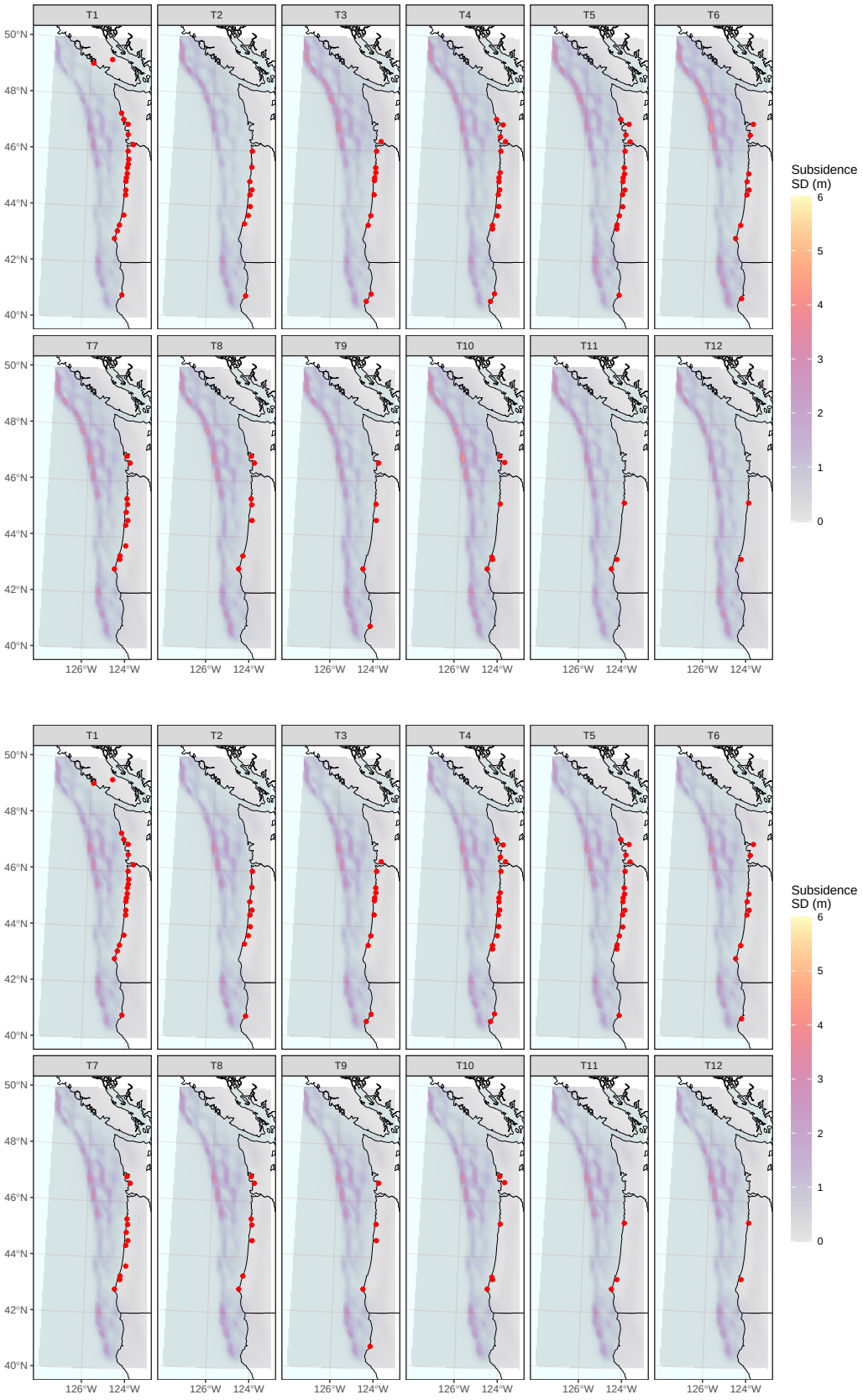

Figure B.2.1: The standard deviation of subsidence across the whole fault calculated for the first model is shown above, and below is the same information but for the second model. The red points give the locations of subsidence estimates. The illustration was created by linearly interpolating the standard deviations on the grid shown in Figure 4.3.3.

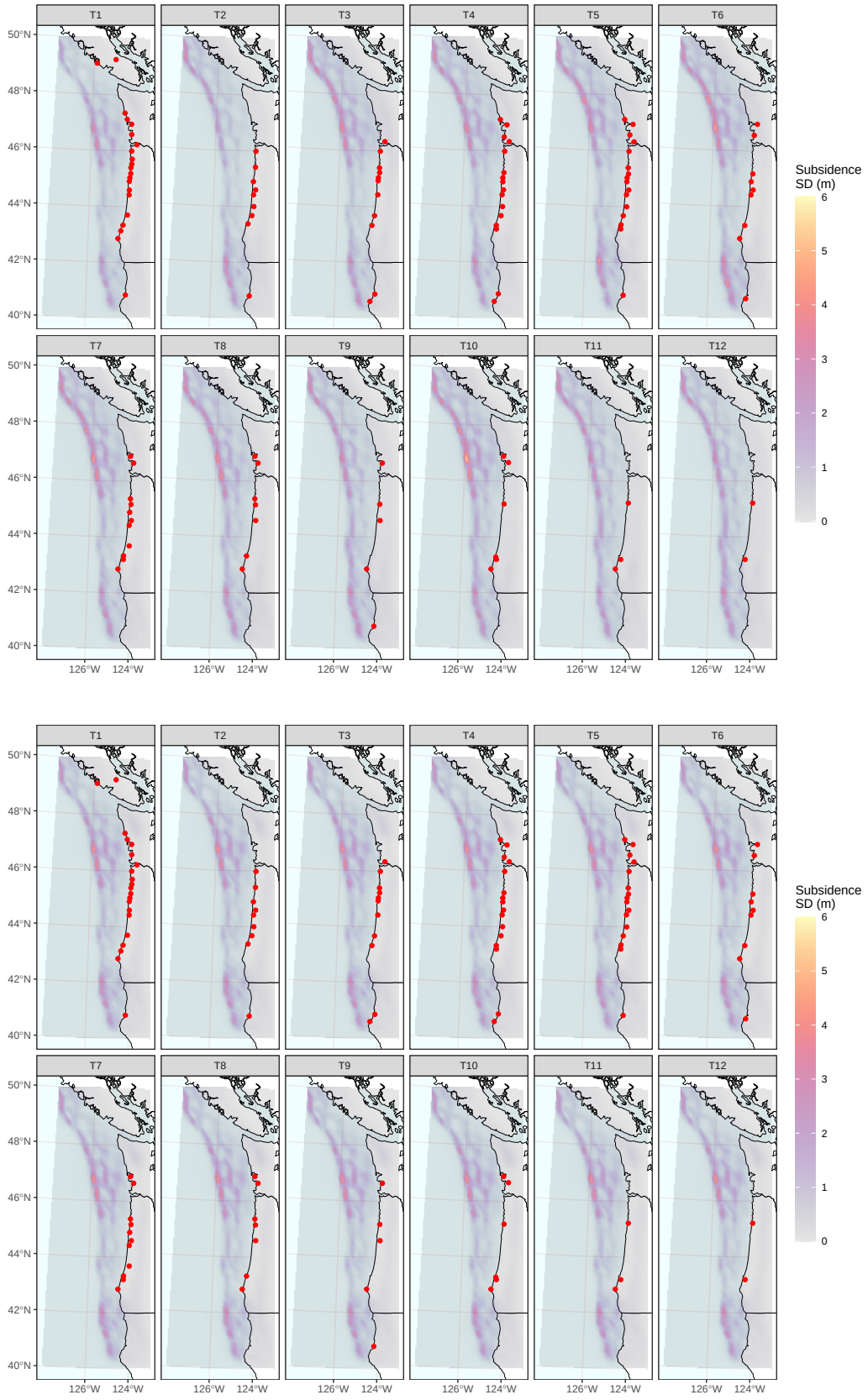

Figure B.2.2: The standard deviation of subsidence across the whole fault calculated for the third model is shown above, and below is the same information but for the fourth model. The red points give the locations of subsidence estimates. The illustration was created by linearly interpreting the standard deviations on the grid shown in Figure 4.3.3.

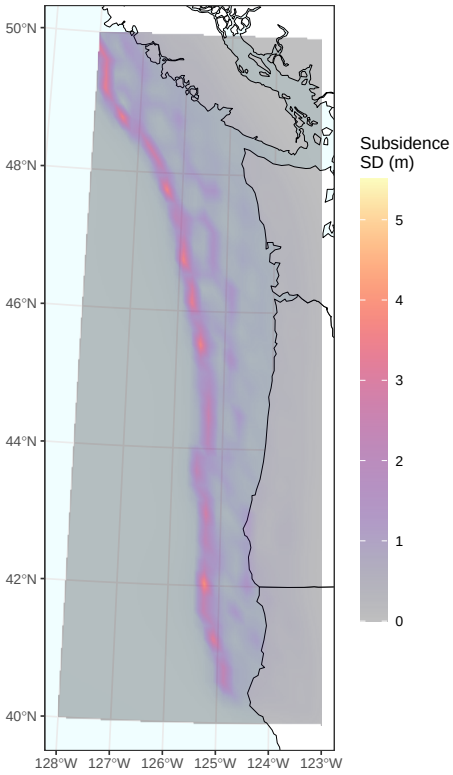

(a) Model 1

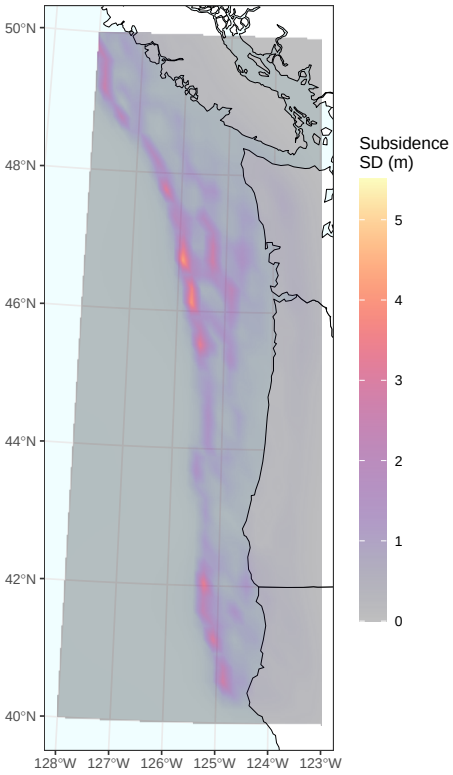

(b) Model 2

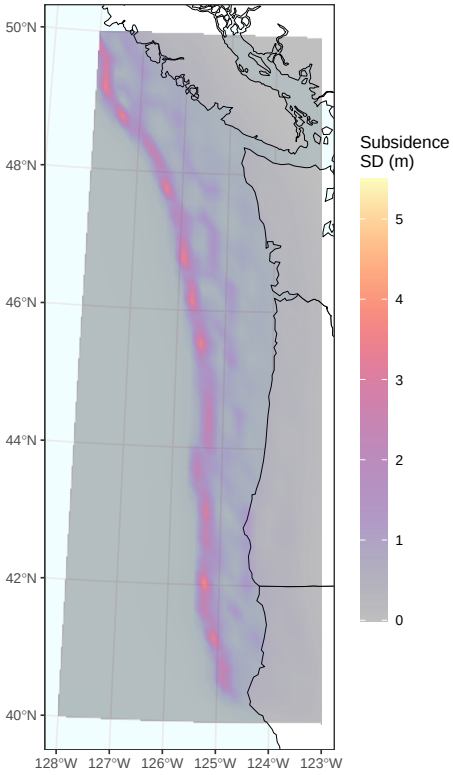

(c) Model 3

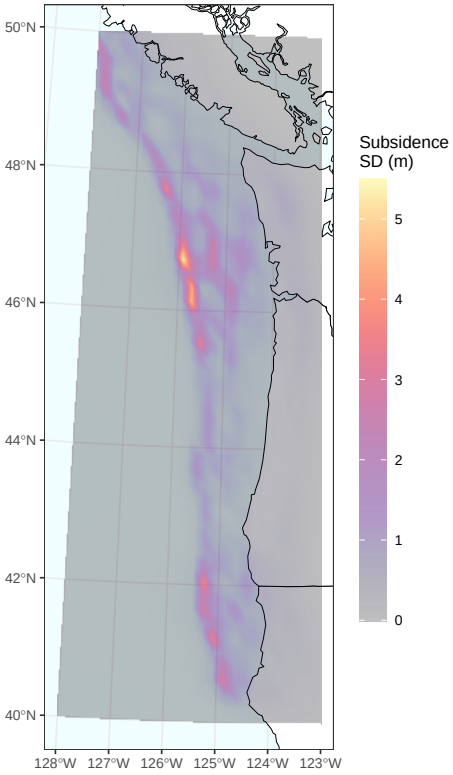

(d) Model 4

Figure B.2.3: These plots show the standard deviations of 1000 predictions of future subsidences across the entire CSZ for all the model.

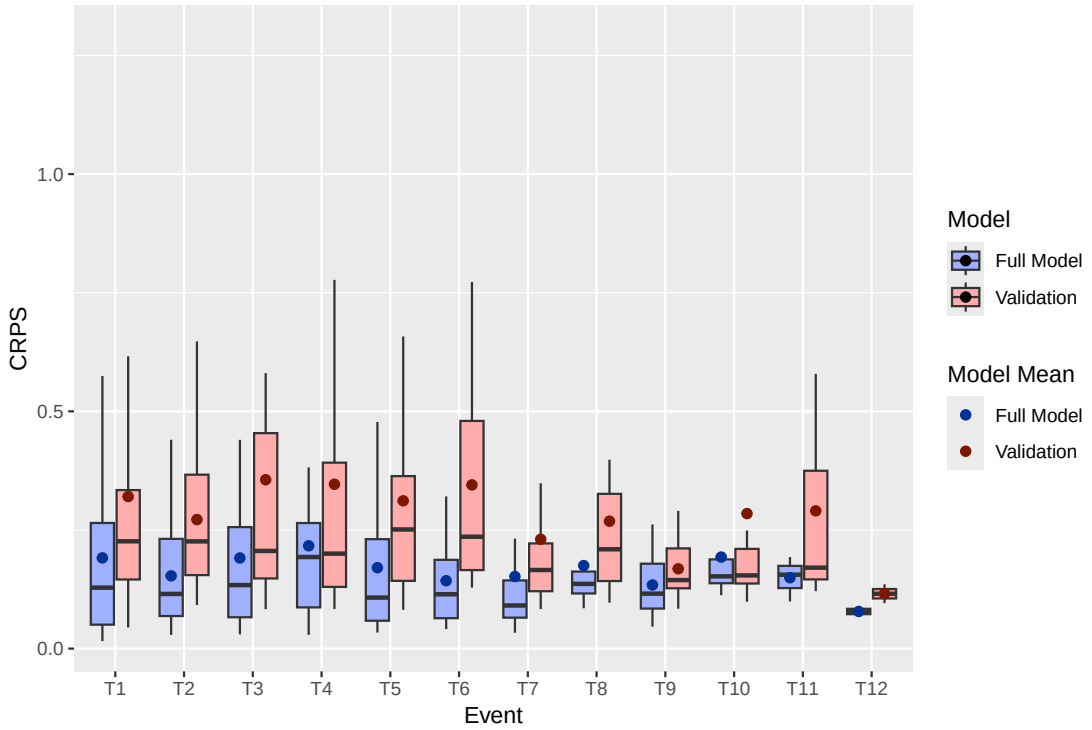

(a) Model 1

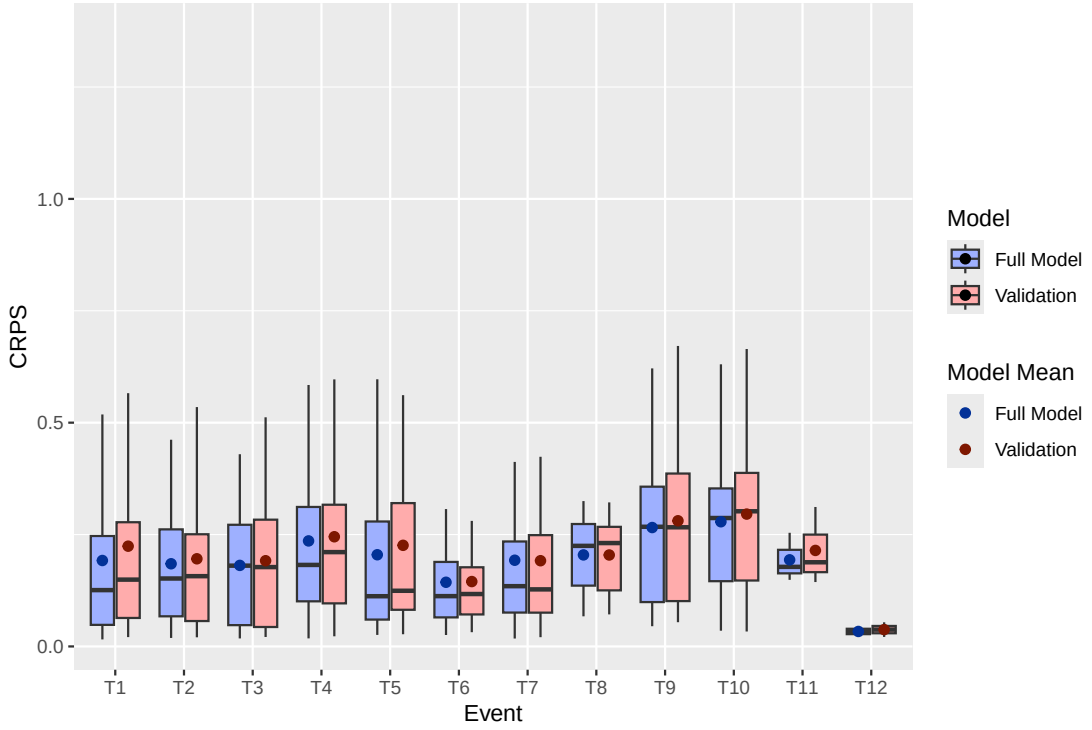

(b) Model 2

Figure B.3.1: The CRPS score for the full model subsidence predictions and the validation models predictions are shown for the isotropic models.

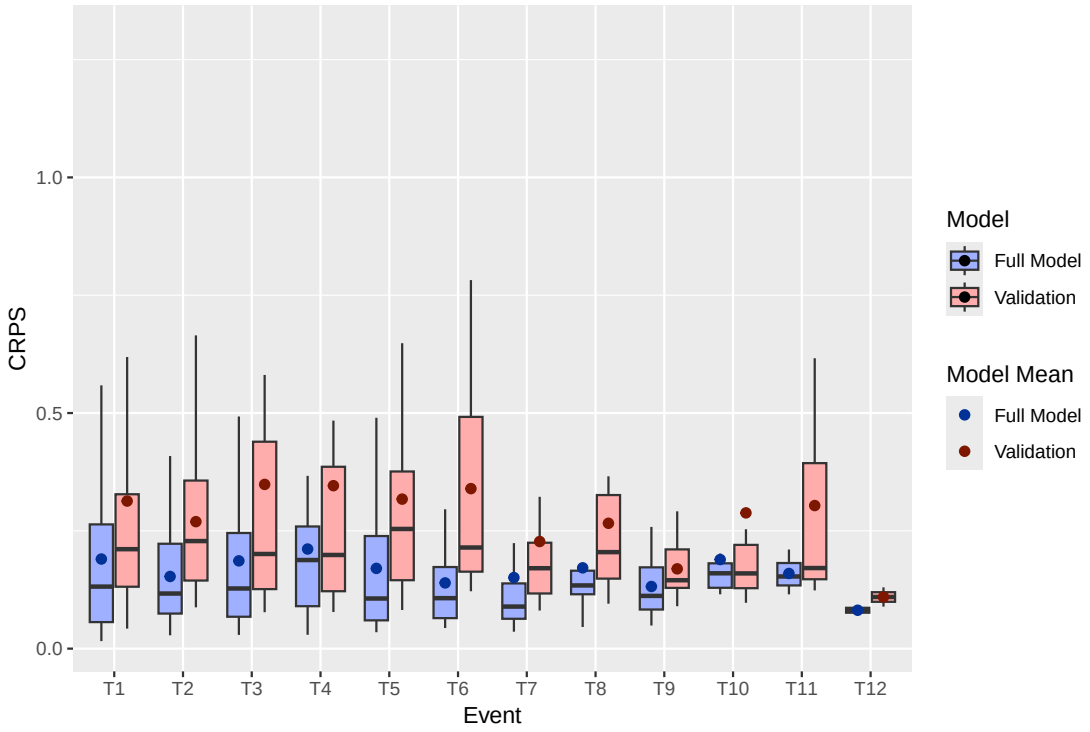

(a) Model 3

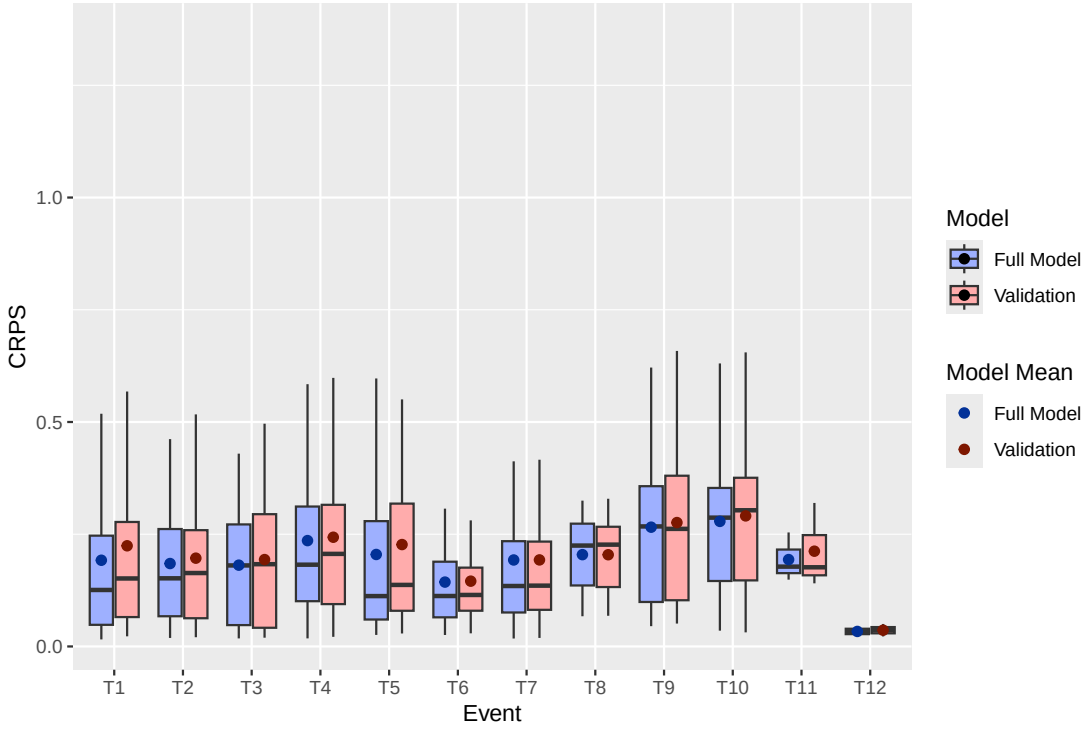

(b) Model 4

Figure B.3.2: The CRPS score for the full model subsidence predictions and the validation models predictions are shown for the anisotropic models.

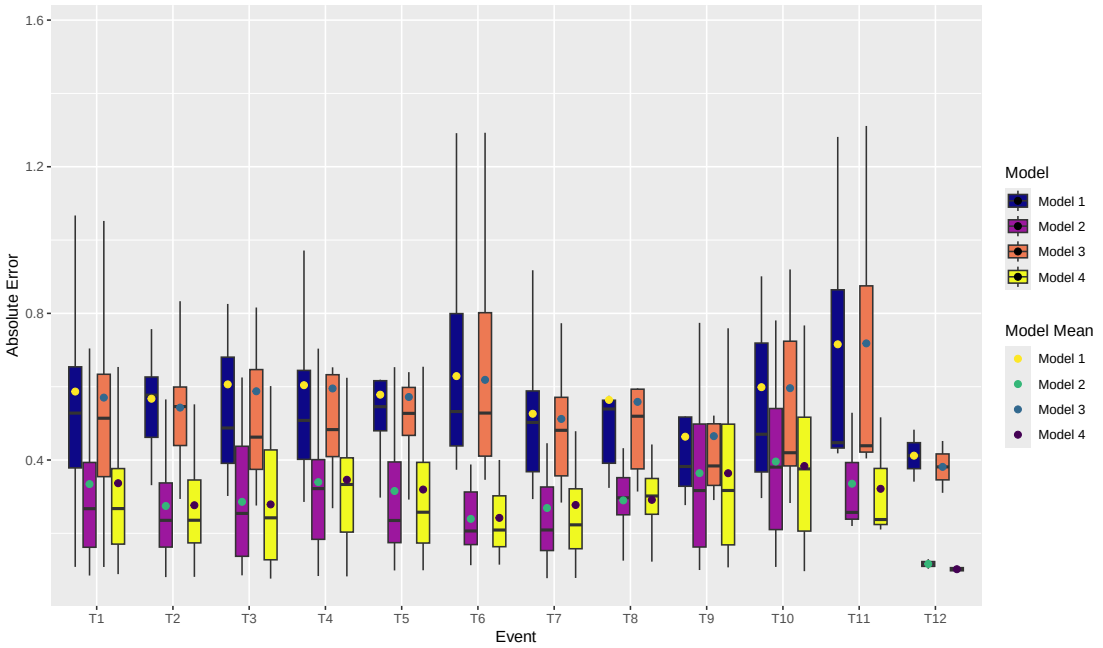

Figure B.4.1: This figure shows the distribution of absolute errors for each megathrust event and model. The scores are calculated during the validation process.

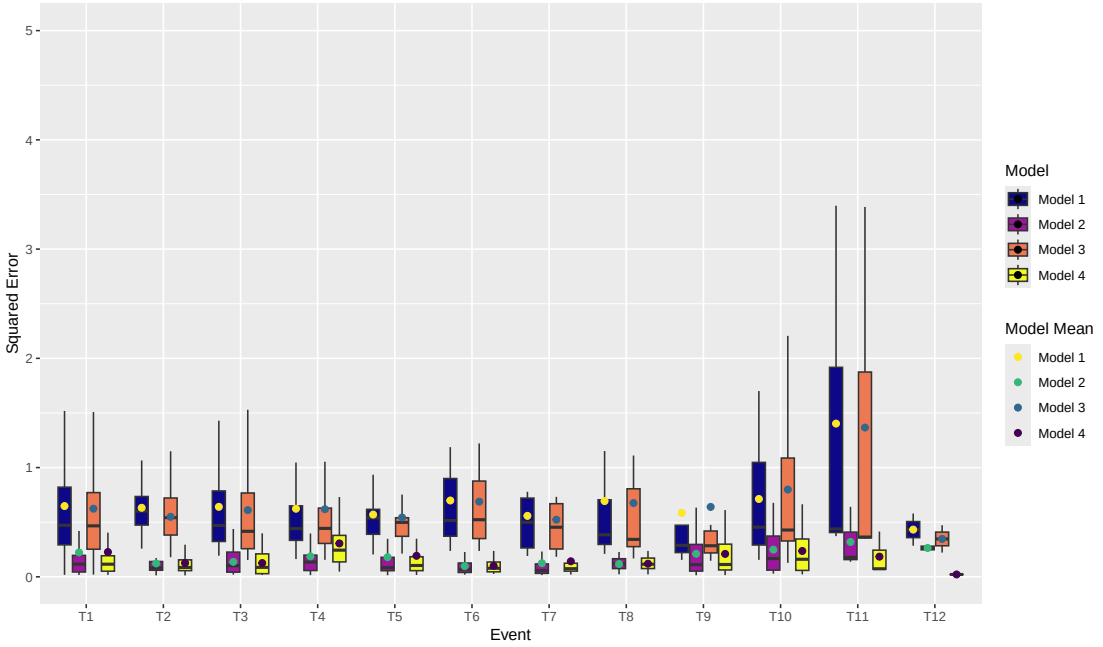

Figure B.4.2: This figure shows the distribution of squared errors for each megathrust event and model. The scores are calculated during the validation process.

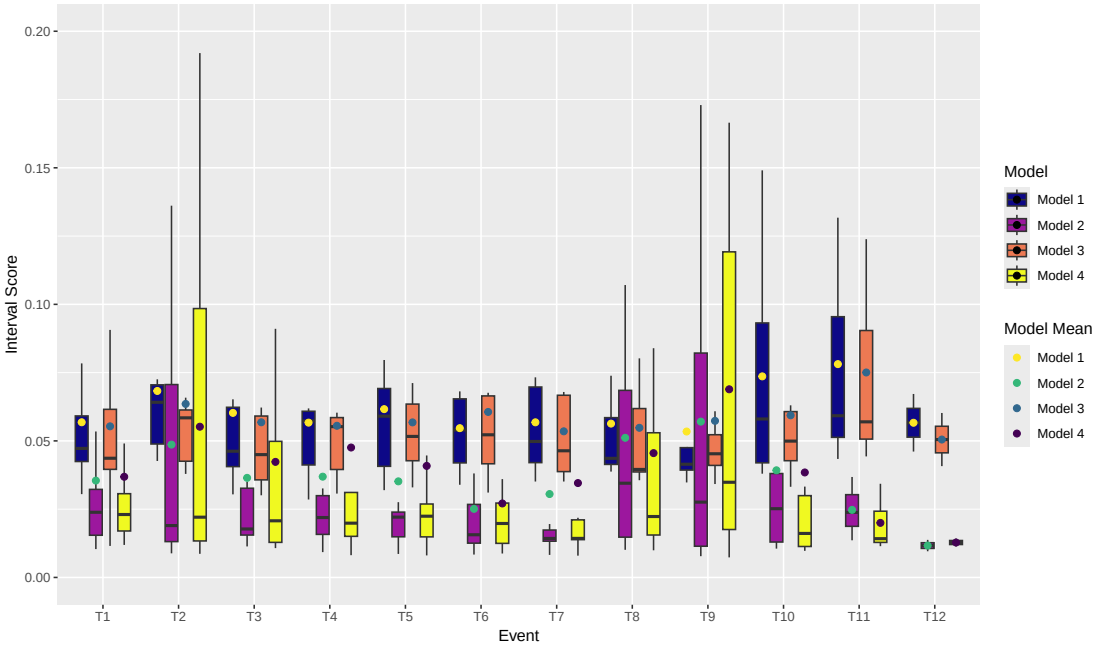

Figure B.4.3: This figure shows the distribution of the interval scores for each megathrust event and model. The scores are calculated during the validation process.

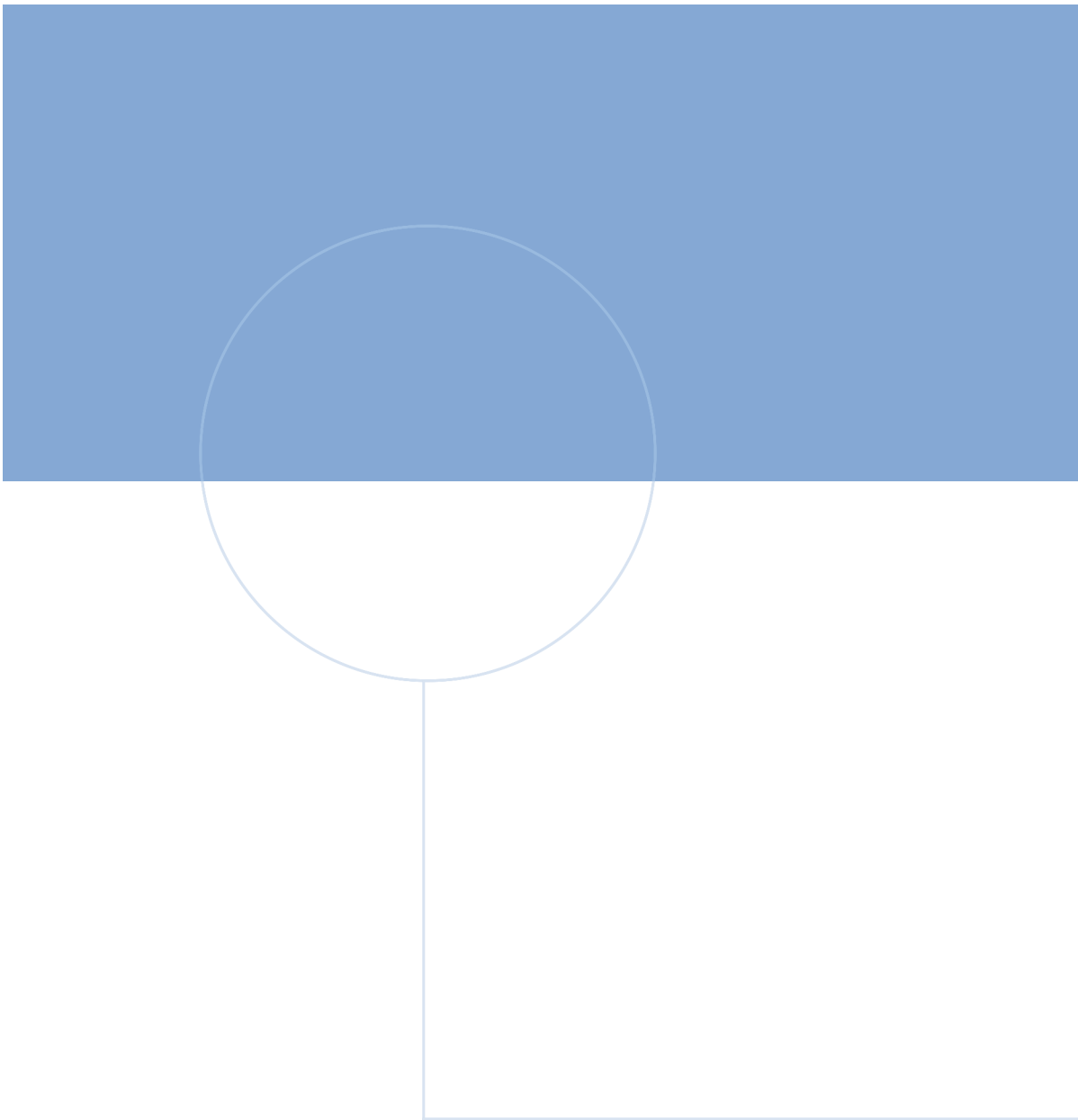

NTNU

Norwegian University of
Science and Technology